Unobtrusive Monitoring of Fluid Accumulation in the Body Using Ballistocardiography

Master Thesis

Irene Suriani

Delft University of Technology

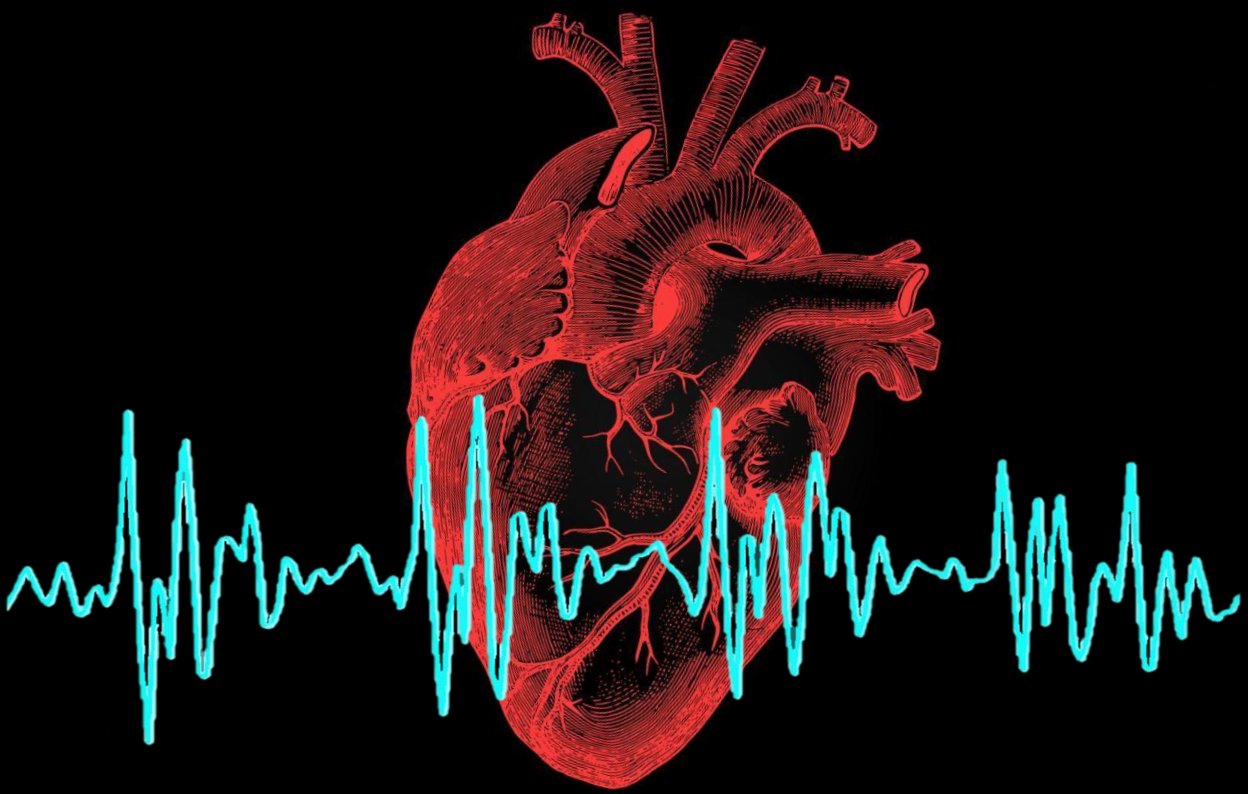

TU Delft

UNOBTRUSIVE MONITORING OF FLUID ACCUMULATION IN THE BODY USING BALLISTOCARDIOGRAPHY

A Feasibility Study

By

Irene Suriani

to obtain the degree of Master of Science in Biomedical Engineering
at the Delft University of Technology,
to be defended publicly on Thursday 29th August, 2019 at 11:00 AM.

Student number: 4729331

Project duration: 1st January 2019 – 19th August 2019

Supervisors: Paddy French – TU Delft
Kiran Dellimore – Philips Research

Acknowledgements

First and foremost, I would like to thank my daily supervisor Kiran Dellimore, and my co-supervisors Murtaza Bulut and Ron van Lieshout, for giving me the opportunity to carry out this project, for guiding me through it with genuine enthusiasm, and for making me feel part of their team from the very beginning of my stay at Philips Research.

Furthermore, I would like to thank my academic supervisor prof. Paddy French, for introducing me to this project and following up on my progress despite the distance.

I would also like to thank Rohan Joshi for his valuable support during my first months of work at Philips Research, and later on for the occasional involvement in the project and inspiring conversations.

I am extremely grateful to all my fellow interns and friends Carla, Francesca, Margarida, Himanshu, Saharsh, Tim, Claudia, Sinduja, Alessio, Sevgi, José, Alex, and all the wonderful people I have had the chance to meet in the past twelve months, for the daily dose of fun at work, and for all the beautiful memories that will forever warm my heart.

This page would not be complete without mentioning my TU Delft family: Shubham, Mina, Esther, Alberto, Armin, Amal, Pedro, Jens, Ferry, Hande, Tawab, Quinten and Corey. Thank you for making the past two years unforgettable, and for always inspiring me with your brilliant minds and gentle souls.

Finally, to my sister, parents and grandmothers, for the unconditional love and support, and for being the motivation behind any accomplishment in my life.

Abstract

Fluid accumulation in the human body is, in many cases, a symptom of some underlying pathological condition. Most common examples include edema, ascites, pleural effusion, and internal bleeding. Currently available non-invasive methods to assess fluid accumulation in the body are mainly imaging-based (i.e. ultrasound, computed tomography). This means that monitoring is limited to spot-checks and is only performed when the presence of a particular condition is already suspected from prior clinical evaluation of the patient. There is high clinical interest in the development of a system allowing such monitoring to be performed automatically, continuously over a prolonged period of time, and independently of prior clinical evaluation. For instance, in the case of internal bleeding, hemorrhage indicators such as variation in heart rate and blood pressure are only observable after significant blood loss (up to more than 1 liter) has already taken place, therefore an early warning system can save lives, decrease hospital stay length and significantly reduce complication-related costs.

In this thesis, a pioneer solution is proposed for development of such a monitoring system. The hypothesized solution is based on the observation of specific energy-describing features of the Ballistocardiogram (BCG) signal, a measure of the periodic displacements generated on the body as a result of ballistic forces produced by the heart during each cardiac cycle. Because of additional damping generated by the presence of internally accumulated fluid, the energy of this signal is expected to decrease compared to its baseline value. The BCG can be recorded unobtrusively with different sensing modalities on the surface of the body.

In order to validate the research hypothesis and assess the feasibility of this novel technique, a custom experimental set-up exploiting several different BCG sensing options has been used to carry out a study on 15 human volunteers. Localized fluid accumulation along the GI tract was induced in a controlled, safe and simple fashion, by means of water intake by the participants, and the BCG signal was recorded before and after intake. Signal feature exploration and performance analysis has been used to develop an optimized feature able to accurately capture the decrease in signal energy due to fluid accumulation, as well as to identify the most suitable sensor type and monitoring body location for the present application.

The developed energy-describing feature shows a significant decrease in energy value from baseline to after-intake condition with a p-value<0.001. Moreover, the selected feature was able to correctly identify presence of fluid accumulation with high sensitivity (90% in bed-based, and 100% in standing-position monitoring). Given the promising results of the present study, further research towards improvement and development of the proposed technique is highly encouraged.

Table of contents

List of Figures 3
List of Tables 5
List of Abbreviations 6
1. Introduction 7
2. Monitoring Fluid Accumulation in the Body 9
2.1. Pathology of Fluid Accumulation in the Body 9
2.2. Current Monitoring Methods 10
2.3. An Envisioned Pioneer Solution Based on Ballistocardiography 12
3. An Introduction to Ballistocardiography 13
3.1. Historical overview 13
3.2. The Physics of Ballistocardiography 14
3.3. Physiology of the BCG Signal 14
3.4. Available Sensing Modalities 16
4. Hypothesis and Research Objectives 19
5. The Experiment 21
5.1. The Experimental Setup 22
5.2. The Study Protocol 23
5.3. The Dataset 25
6. Signal Processing and Feature Analysis 27
6.1. Visual Inspection of the Signals 27
6.2. Spectral Analysis 30
6.3. Pre-processing: Artifact Removal and Noise Filtering 34
6.4. Heart Rate Extraction 35
6.5. Feature Exploration 37
6.6. Preliminary Feature Selection 40
6.7. Feature Optimization 47
7. Results 52
8. Discussion 57
8.1. Variability of The Effect Magnitude 57
8.2. Inter-personal and Intra-personal Variability of the Baseline 60
8.3. Feature Overfitting 63
9. Key Contributions and Future Developments 64
Bibliography 67

List of Figures

Figure 1: Comparison of a FAST scan (to the left) and a CT scan (to the right) of the same patient [14]. 11
Figure 2: BCG waveform obtained from the Starr Ballistocardiograph [15] 14
Figure 3: Events in a cardiac cycle (Reproduced after: The McGraw-Hill Companies, Inc.) 15
Figure 4: Amplitude ratio of a system under harmonic force at different frequency ratios and different damping ratios, image from Wikipedia. 20
Figure 5: Orientation of the accelerometers' axes with respect to the body's anatomical planes. 22
Figure 6: Schematization of the experimental setup. Accelerometer locations shown refer to Test Round 1 23
Figure 7: Accelerometer locations in the two test rounds. The dotted circles indicate that the accelerometer is placed on the backside of the body 25
Figure 8: Synchronized segments of raw unfiltered signals from different acquisition channels during Test Round 1 in the lying position 27
Figure 9: Synchronized segments of raw unfiltered signals from different acquisition channels during Test Round 2 in the lying position 28
Figure 10: Synchronized segments of raw unfiltered accelerometer signals (EMFIT is not relevant to standing measurement) from different acquisition channels during Test Round 1 in the standing position 28
Figure 11: Accelerometer signals acquired from two different study participants plotted in different colors 29
Figure 12: Example of an accelerometer signal segment containing movement artifacts, marked by orange triangles 29
Figure 13: One complete standing measurement, with initial and last few seconds of measurement corrupted by movement artifacts (highlighted in orange). 30
Figure 14: Spectra of signals acquired during Test Round 1 in lying position 31
Figure 15: Spectra of signals acquired during Test Round 1 in lying position, with y-axis is plotted in base 10 logarithmic scale. 32
Figure 16: Spectra of signals acquired during Test Round 1 in the standing position, with y-axis of the plots rescaled so to focus on the higher frequency components. 32
Figure 17: Spectra of signals acquired during Test Round 1 in standing position, with y-axis plotted in base 10 logarithmic scale. 33
Figure 18: BCG power spectra reported in [28]. 33
Figure 19: Peak-to-peak amplitude per second of one 3-minute measurement: the second at which the artifact is detected is marked by an orange triangle 34
Figure 20: Two examples where peak-to-peak amplitude-based artifact removal is used. On the left is a signal from the EMFIT sensor, on the right from an accelerometer. The plots in blue represent the original signals, while the signals after artifact removal is applied are superimposed in orange. 35
Figure 21: Magnitude to frequency response of the 6-th order Butterworth band pass filter designed for heart rate extraction. The two black vertical lines mark the normal resting heart rate band (1 to 1.6 Hz). 36
Figure 22: Example of heart rate extraction procedure 37
Figure 23: Empirical mode decomposition of a BCG signal 39
Figure 24: Segment of signal denoised using EMD (in orange) with the corresponding original signal (in blue) 40
Figure 25: For each feature, number of participants, averaged amongst the 12 signals, showing a significant decrease in feature value from BL to AI according to Student t-test calculated on Test Round 1, lying data. The black vertical lines indicate standard deviation from the average. 43
Figure 26: For each feature, number of participants, averaged amongst the 12 signals, showing a significant decrease in feature value from BL to AI according to Wilcoxon Rank Sum test calculated on Test Round 1, lying data. The black vertical lines indicate standard deviation from the average. 43
Figure 27: For each feature, mean t_{stat} value per participant, averaged amongst the 12 signals, calculated on Test Round 1, lying data. The black vertical lines indicate standard deviation from the average. The dashed lines indicates the t_{stat} value for which a result is deemed statistically significant at the chosen α value (in both directions) for the sample size considered. 44
Figure 28: For each feature, number of participants, averaged amongst the 12 signals, showing a significant decrease in feature value from BL to AI according to Student t-test calculated on Test Round 1, standing data. The black vertical lines indicate standard deviation from the average. 44
Figure 29: For each feature, mean t_{stat} value per participant, averaged amongst the 12 signals, calculated on Test Round 1, standing data. The black vertical lines indicate standard deviation from the average. The dashed line indicates the t_{stat} value for which a result is deemed statistically significant at the chosen α value for the sample size considered. 45
Figure 30: For each feature, number of participants, averaged amongst the 12 signals, showing a significant decrease in feature value from BL to AI according to Student t-test calculated on Test Round 2, lying data. The black vertical lines indicate standard deviation from the average. 45

Figure 31: For each feature, mean t_{stat} value per participant, averaged amongst the 12 signals, calculated on Test Round 2, lying data. The black vertical lines indicate standard deviation from the average. The dashed line indicates the t_{stat} value for which a result is deemed statistically significant at the chosen α value for the sample size considered. 46
Figure 32: Scatter plot of instantaneous feature values, calculated from two BL and two AI measurements, against the corresponding instantaneous heart rate values 47
Figure 33: Sensitivity of σ-based features calculated on incremental set of frequency bands for each signal considered, for data set of Test Round 1, lying position. 48
Figure 34: Sensitivity of σ-based features calculated on incremental set of frequency bands for each signal considered, for data set of Test Round 2, lying position. 48
Figure 35: Schematization and nomenclature of the accelerometer signal channels analyzed 49
Figure 36: Sensitivity of σ-based features calculated on incremental set of frequency bands for each signal considered, for data set of Test Round 1, standing position. 50
Figure 37: Feature performance using different window length and overlap percentage combinations, in terms of sensitivity and mean t_{stat} per participant (taking into account only the significant values). 51
Figure 38: Schematization of optimized signal processing steps involved in energy feature extraction (for reference on signal nomenclature, see Figure 35). 52
Figure 39: Boxplot representation of the energy feature values obtained from standing measurements of Test Round 1. BL and AI stand for baseline and after-intake condition, respectively 54
Figure 40: Boxplot representation of the energy feature values obtained from lying measurements of Test Round 1. BL and AI stand for baseline and after-intake condition, respectively 55
Figure 41: Boxplot representation of the energy feature values obtained from lying measurements of Test Round 2. BL and AI stand for baseline and after-intake condition, respectively 55
Figure 42: Sample distribution histograms of BL and AI values obtained for each of the 15 participants during the lying Test Round 2 57
Figure 43: Linear regression of individual t_{stat} value from lying measurements of Test Round 1 to participant BMI, weight, gender, age and average heart rate 58
Figure 44: Linear regression of individual t_{stat} value from lying measurements of Test Round 2 to participant BMI, weight, gender, age and average heart rate. 59
Figure 45: Difference in t_{stat} value of each participants between the two lying test rounds. Blue dots represent results of Test Round 1 and magenta dots of Test Round 2. 60
Figure 46: Boxplots obtained by grouping the BL and AI feature values of the two test rounds for the lying data. 61
Figure 47: Mean BL values from the two lying test rounds for each participant. 62
Figure 48: Boxplots of BL vs. AI feature values of all participants from both Test Rounds 62

List of Tables

Table 1: Hypovolemic shock symptoms classification for a 70-kg male adult [1] 10
Table 6: Statistical distribution of participants' age, BMI, and monitoring duration 25
Table 7: Overall performance (averaged between Test Rounds 1 and 2) of the optimal σ-based feature bands for lying condition, calculated on Signal 10 49
Table 8: Overall performance of the optimal σ-based feature bands for standing condition, calculated on Signal 1 50
Table 9: Performance of optimized energy feature (applied to Signal 10) in lying tests 53
Table 10: Performance of optimized energy feature (applied to Signal 1) in standing test 53
Table 11: Performance of optimized energy feature, this time applied to Signal 10, in standing test 53
Table 12: Results of paired-sample Student's t-test for the three experimental datasets 56
Table 13: Regression coefficients and *p*-values for each independent variable for lying data of both Test Rounds 59
Table 14: Performance of generalized feature in terms of statistic values from a paired-sample Student's t-test and of sensitivity 63

List of Abbreviations

- AI – After-intake
- ANS – Autonomous Nervous System
- BCG – Ballistocardiogram
- BL – Baseline
- BMI – Body Mass Index
- CT – Computed Tomography
- DAQ – Data Acquisition
- ECG – Electrocardiogram
- EMD – Empirical Mode Decomposition
- EMFi – Electromechanical Film
- FAST – Focused Abdominal Sonography for Trauma
- GI – Gastrointestinal
- HR – Heart Rate
- HRV – Heart Rate Variability
- IMF – Intrinsic Mode Function
- MAD – Median Absolute Deviation
- MEMS – Micro-machined Electro-Mechanical Systems
- PVDF – Polyvinylidene Fluoride
- REM - Rapid Eye Movement

1. Introduction

Abnormal fluid accumulation in localized compartments of the human body is a symptom common to several pathological conditions. Some commonly encountered examples are edema, ascites, pleural effusion, and internal bleeding. In these cases, timely detection and monitoring of the fluid build-up is essential to plan correct medical intervention. In particular, a system capable to unobtrusively monitor the development of abnormal fluid accumulation in the body is highly needed. At present, non-invasive methods to assess fluid presence in the body are mainly imaging-based (i.e. ultrasound, computed tomography). This means that monitoring is limited to spot-checks and is only performed when the presence of a particular condition is already suspected from clinical evaluation of the patient. There is high clinical interest in the development of a system that could allow such monitoring to be performed automatically, continuously over a prolonged period of time, and independently of prior clinical evaluation. For instance, in the case of internal bleeding, hemorrhage indicators such as variation in heart rate and blood pressure are only observable after significant blood loss (up to more than 1 liter) has already taken place [1]. Therefore, an early warning system could save lives, decrease hospital stay length and significantly reduce complication-related costs.

In the present study, use of the Ballistocardiogram (BCG) signal is, for the first time, investigated as a monitoring technique for onset of fluid accumulation in the body. Ballistocardiography is an unobtrusive measuring technique that records the periodic displacements generated on the body as a result of ballistic forces produced by the heart with the ejection of blood into the large vessels during each cardiac cycle. These movements can be recorded on the surface of the body using several non-invasive and unobtrusive sensing modalities [2]. The hypothesis investigated in the present work is that the energy of the BCG-induced body oscillations will decrease, compared to its baseline value, due to the presence of an additional damping element, corresponding to the added internal liquid mass, in the vibrating system. This effect is expected to be reflected in the energy of the acquired signal.

In order to validate this hypothesis and evaluate feasibility of the proposed technique, a human-based experiment was designed and conducted involving 15 volunteers. Localized fluid accumulation along the GI tract was induced in a controlled, safe and simple fashion, by means of intake of 500 mL of water by the participants. Several sensing options were used to record the BCG signal of the volunteers at several body locations before and after water intake, with the purpose of investigating the optimal sensing modality. These included accelerometers, electromechanical film and load-cells. The experiment included two test rounds per volunteer conducted at approximately one-week distance, and including bed-based monitoring as well as monitoring in the standing position. Based on the collected dataset, specific data preparation was performed (mainly involving automated detection and removal of movement artifacts) and an initial set of energy-describing signal features was designed, exploring different signal pre-processing steps and investigating different spectral components of the signal, by means of classical filtering techniques as well as based on Empirical Mode Decomposition (EMD). Features were computed on short-time sliding windows in order to ensure higher resolution of the signal energy estimate. Features were then evaluated according to defined performance parameters; namely, the sensitivity – defined as the number of study volunteers for which the feature was able to 'detect' fluid accumulation by showing a statistically significant decrease compared to its value at baseline condition – and the t_{stat} value, a measure to quantify the

separation between two sets of values in terms of their mean difference and respective variances. Based on these performance metrics, the most promising feature appeared to be standard deviation of the signal filtered at a pass band including only the higher frequency components of the BCG signal (above respiration and heart rate). This band of frequencies is thought to be maximally affected by damping due to interaction with the natural frequencies of the body itself, as explained more in depth in Chapter 6 of this report. Contextually, the optimal signal channel to use for feature extraction, amongst the ones available, was indicated for both bed-based and standing monitoring modalities. Further feature optimization involved fine-tuning of the filter cutoff frequencies as well as definition of the optimal window length and percentage overlap for feature calculation. Finally, the research hypothesis was proven by means of a paired-sample t-test, which showed that a significant decrease in energy feature value exists from baseline to after-intake condition at a confidence level higher than 99.9% (p-value<0.001) in both test rounds performed, and in both monitoring modalities (bed-based and standing). Moreover, the feature was able to correctly identify presence of fluid accumulation with high sensitivity (90% in bed-based and 100% in standing monitoring).

The present report is structured as follows. Chapter 2 briefly delineates the clinical need for an unobtrusive monitoring system for internal fluid accumulation. The following chapter gives an introduction on Ballistocardiography, including physics and physiology of the signal and available sensing modalities. Chapter 4 states and explains in detail the research hypothesis at the basis of the present work, and lists the research objectives. Chapter 5 deals describes the experimental setup and methodology for data collection, while Chapter 6 the signal processing and feature analysis methods employed. Chapter 7 reports the achieved results, which are then discussed in Chapter 8. Finally, Chapter 9 summarizes conclusions and key contributions of the present work, and proposes future research avenues that will allow further understanding of the physiological aspects involved in this project, and advancing of the investigated technique towards a reliable monitoring tool.

2. Monitoring Fluid Accumulation in the Body

2.1 Pathology of Fluid Accumulation in the Body

Accumulation of fluid in the body cavities is a symptom common to a variety of pathological conditions. Early detection of this symptom is critical, in some cases because the fluid accumulation itself is a threat to the patient's life, in others because it might lead to the diagnosis of serious conditions requiring timely medical intervention. Some examples are hereby briefly described:

- *Ascites* is a condition consisting in the accumulation of free fluid in the peritoneal cavity. It can result from a variety of pathologies, including heart failure, cirrhosis and cancer. Possible complications include life-threatening spontaneous bacterial peritonitis. It is usually diagnosed by physical examination, followed by ultrasound or computed tomography (CT) scan. It is classified according to three grades of severity, and is only visibly detectable at its second and third grade of severity [3], [4].
- *Edema* consists in the abnormal build-up of interstitial fluid, which can occur at several different locations in the body, including limbs, face, as well as internal organs including brain and lungs. It can occur at several grades of severity, and have diverse etiology, largely specific to the location and type of edema experienced. Causes include systemic diseases, cardiac or liver failure, pregnancy-related conditions, and minor local conditions [5].
- *Hydrocephalus* is the accumulation of cerebrospinal fluid in the brain. It can indicate a variety of conditions such as neural tube defects, meningitis, brain tumors, traumatic brain injury, and intraventricular hemorrhage. It is diagnosed based on symptoms identification, followed by imaging, and can be deadly if untreated [6].
- *Pleural Effusion* consists in the development of excess bodily fluid (that can be of different nature) in the pleural cavity, and can result in compression of the lungs impairing breathing. Possible etiologies include congestive heart failure, cirrhosis, pneumonia, pulmonary infarction, and a long list of others. It is diagnosed based on medical history, physical examination and imaging [7].
- *Internal Hemorrhage* is the loss of circulating blood volume into internal body cavities. In can result from a vast set of conditions, the most common being blunt trauma, post-operative complications, gastrointestinal pathologies, obstetrical complications or rupture of aneurysms. If not timely managed, it can lead to hemorrhagic shock and, eventually, deadly exsanguination. Internal bleeding is, in fact, a leading cause of preventable mortality, as it can easily go undetected: several liters of blood can be lost into the body cavities without external evidence. Body pouches such as the pleural space, the abdominal cavity, the mediastinum and retroperitoneum, as well as the pelvic cavities are common locations of hemorrhage, and can accommodate quantities of blood sufficient to cause deadly exsanguination [8]. Among post-operative complications, bleeding is the main attributable reason for post-operative mortality [10]. In case of post-surgical bleeding, bleeding is often slow and might not itself be an acute life threat; however, re-operation is required as early as possible: in some cases of post-operative bleeding, mortality increases from 9% to as high as 25% if the second surgery is performed after 6 hours from the onset of bleeding. As post-operative

bleeding can develop several days after surgery (for instance, the average onset time for bleeding is 6.1 days after liver transplantation surgery and 12 days after pancreatic surgery), continuous long-term monitoring is essential in order to allow early detection of bleeding, and a timely intervention means significantly reducing the risk of complication and death [11].

The economic burden of internal bleeding is high. A study on bleeding complications after endovascular procedures showed that the length of median hospital stay is 3 times as high, and median healthcare cost per patient increases of more than 18,000 dollars in the case of bleeding complications [12]. A French study analyzing surgeries that are most commonly affected by bleeding complications found the length of hospital stay to increase by 26.5% and costs by 19.9% in case of bleeding complications [13]. From a broader perspective, considering that functional recovery from hemorrhagic shock is often poor, and the percentage of survived patients that return to work after 2 years is only of 50-58%, the overall socioeconomic impact is likely even higher [9].

Unfortunately, the current practice for identifying internal hemorrhage relies on monitoring of vital signs, mainly heart rate and mean arterial pressure. However, changes in these are only noticeable at an advanced stage of hemorrhage, as the body is normally able to hemodynamically compensate for up to 1 liter or more of blood lost, without external evidence. Table 1 classifies, according to international standards, hemorrhagic blood symptoms based on the estimated amount of blood loss. As is clear from the table, increase in heart rate starts being noticeable only in Class II hemorrhage, with 750 to 1500 mL of blood lost, and blood pressure starts dropping at an even later stage [1].

Table 1: Hypovolemic shock symptoms classification for a 70-kg male adult [1]

	Class I	**Class II**	**Class III**	**Class IV**
Blood loss [mL]	<750	750-1500	1500-2000	>2000
Blood loss (% blood volume)	<15	15-30	30-40	>40
Heart rate (bpm)	<100	100-120	120-140	>140
Systolic blood pressure [mmHg]	Normal	Normal	Decreased (<100)	Decreased (<70)
Respiratory rate (breaths per minute)	14-20	20-30	30-40	>35
Urine output [mL/h]	>30	20-30	5-15	Negligible
Mental state	Normal	Mildly anxious	Anxious, confused	Confused, lethargic

2.2 Current Monitoring Methods

Clinical assessment of the patient is always the first step in the individuation of internal fluid accumulation. Externally visible or measurable symptoms vary according to the specific pathology, and so does the severity of the condition at the time symptoms become apparent. As explained in the previous section, internal hemorrhage is one of the most striking examples where external manifestation of symptoms often occurs at a late stage of the condition.

Once the presence of fluid has been suggested by primary survey of the patient, imaging-based techniques are the main tool employed in further examination, localization of the fluid pool and diagnosis. Ultrasound and CT are the most widely used.

Focused Abdominal Sonography for Trauma (FAST) scan is one of the most established tools to investigate presence of free fluid in the abdominal cavities [9]. The extended FAST (eFAST) scan additionally allows for examination of the thoracic region. FAST is an ultrasound-based imaging technique, and is widely used as a decision-making tool for intervention. Its sensitivity and specificity for detection of free fluid vary depending on the target area, ranging from 69% to 98%, and from 94% to 100%, respectively [10]. Sensitivity of FAST scan is known to be lower in pediatric patients. The minimum volume detection limit for a FAST scan varies depending on target area, with reported values range from 250 to 700 mL for abdominal scans [11],[12] and [13]. Presence of air, bowel gas or excessive fat are known to hinder correct FAST results. FAST scan is not an automatic monitoring tool, and it requires operation by highly trained personnel. Its accuracy has been shown to be greatly dependent on operator experience [10].

CT is an accurate diagnostic test that provides information on the extent, location and source of fluid accumulation. It involves administration of a radiocontrast agent for the enhancement of X-ray visualization, and it produces cross-sectional images of the abdomen. It is effective in identifying fluid located in areas difficult to monitor by FAST, such as the retroperitoneal region. Its sensitivity ranges between 92% and 98%. However, it is a time-consuming procedure (demanding up to an hour for complete image acquisition), which involves the use of costly equipment and requires transport and collaboration of the patient [1].

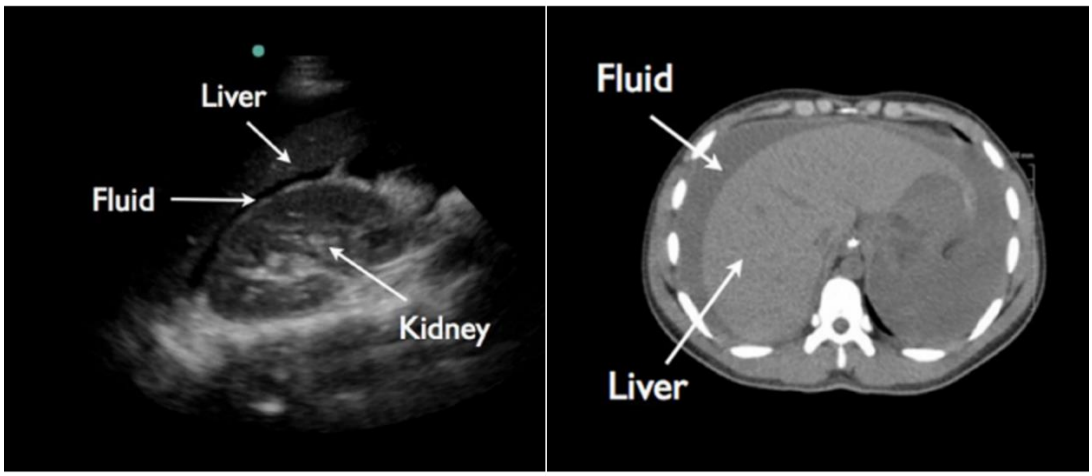

Figure 1: Comparison of a FAST scan (to the left) and a CT scan (to the right) of the same patient [14]**.**

Other, more condition-specific imaging methods are available. However, an automatic continuous-monitoring solution providing early alert for fluid accumulation is currently still unavailable.

2.3 An Envisioned Pioneer Solution Based on Ballistocardiography

From the information reported in the previous sections, the need for a continuous, automated monitoring system for fluid accumulation in the body stands out. Such a system has the potential to target several critical clinical applications. Common limitations of currently available monitoring systems are: the need to be operated by specialized personnel, the restriction to sporadic spot-checks, and the need for prior clinical evaluation of the patient to suggest presence of a pathological condition, which often occurs only at advanced stages of condition severity. The missing link is an automatic, unobtrusive monitoring tool to be smoothly incorporated into the current clinical workflow, serving as an early warning tool triggering further examination or intervention. In the present study, it is hypothesized that such a system could be realized by employing the technique of Ballistocardiography (BCG), a measuring method dating back to the 20th century, and nowadays subject of renovated interest by the scientific community. The BCG signal can be acquired via several sensing modalities, which mostly allow for discrete embedding in daily-use objects such as beds, chairs and wearables, making it an ideal option for the purpose of unobtrusiveness. The following chapter introduces the BCG measuring technique, explaining the physiology of the BCG signal, and giving an overview of the available sensing modalities.

3. An Introduction to Ballistocardiography

3.1 Historical Overview

The term Ballistocardiography finds its etymology in the Ancient Greek words βάλλω "to throw", καρδία "heart", and γραφία "description". It consists, in fact, in recording the repetitive ballistic accelerations imparted to the body by the mass displacement of blood ejected ("thrown") into and along the aorta at each cardiac cycle. The heart, therefore, acts as an intrinsic actuator, generating the driving force that gives rise to the signal.

Isaac Starr (1895-1989) is largely considered "the father of Ballistocardiography", as he developed the first practical ballistocardiograph and published the first related scientific works. The first devices consisted in suspended beds where the subject would lie, enabling recording of the forces exerted on the body's longitudinal axis. Starr's device was a spring-coupled undamped bed with natural frequency of 9 Hz ("high frequency ballistocardiograph"). Other early devices included Nickerson's critically damped, "low frequency" bed, and Nickerson's and Hamilton's first ballistocardiograph able to acquire the signal directly from the body, by measuring displacement of the head vertex while the subject would lie on a fixed bed [15]. In the 1950s Dock and Taubman developed two acquisition methods for body-contact BCG. One was based on a photo-electric technique: the subject lying on a table, a rigid strip of metal would be attached to the shins, and illuminated by a light source. Underneath, a photocell would be placed so that the illuminated strip cast a shadow onto it, which would move according to the body motion on the longitudinal axis. The electrical currents generated on the photocell, varying with body motion, would be recorded by a galvanometer. The second one was electromagnetic-based. A coil of copper wire, attached to the subject's shins in the same configuration as in the previous case, would be immersed in a magnetic field such that the movements imparted to the coil by body displacements would generate currents in the wire, measured by a galvanometer [16].

In spite of the initial enthusiasm for the technique, in the following years Ballistocardiography did not prove a solid enough technique to convert into a clinical examination tool. Fundamental limitations, at the time, mainly involved a difficulty in the physiological interpretation of the signal, as well as technological constraints that would not allow reaching the required signal quality. There was, moreover, a lack of normalization in procedures, devices and nomenclature, that made comparison and cross validation of studies difficult.

Nowadays, the development of new sensing devices and improved signal processing techniques allows for significantly improved quality of BCG measurement, and the technique is in fact object of renewed interest and investigation. The possibility of developing non-invasive and unobtrusive health monitoring tools, which can be embedded in common-use objects (beds, chairs.. etc.), offers promising applications in an era where healthcare is more and more shifting towards e-health and automatic home-care systems [15].

3.2 The Physics of Ballistocardiography

From a physics point of view, the basic underlying principle of Ballistocardiography is Newton's third law of motion: any movement of mass within a body will be reflected by oppositely directed motion of the body itself, conserving the same center of gravity. In order to give a simple demonstration, we can consider the human body as a simplified one-dimensional system. The system comprises of a mass m, corresponding to the combined masses of blood and heart, a mass M, representing the whole body mass, with respective coordinates x and X, and center of mass of the whole system x_C, which we can chose to be at the origin of the system. This can be expressed as:

$$m\ddot{x} + M\ddot{X} = (m + M)\ddot{x_C} = 0 \quad (1)$$

Thus, the force exerted by blood and heart generates an equal and opposite force in the rest of the body. If we now consider the subject standing vertically on a force platform, we have that the equilibrium of forces in the vertical direction gives:

$$F = -(m + M)\ddot{X} + (m + M)g \quad (2)$$

Where F is the vertical reaction force of the force plate, equal to the force generated by the BCG signal (first term on the right-hand side of the equation) plus the gravity force. The BCG records $\ddot{X}$ adjusted for gravity. Rearranging Equation 2, this corresponds to:

$$\frac{\ddot{X}}{g} = 1 - \frac{F}{W} \quad (3)$$

Where W is the weight force given by gravity acceleration times the combined masses m and M. The signals that are usually of interest are x and m, particularly for cardiovascular applications. When m is estimated, x can be obtained from the relation in Equation 1 [17].

3.3 Physiology of the BCG Signal

The characteristic BCG waveform reflects events occurring within a cardiac cycle. Although the waveform shape obtained varies with different sensing modality used, there are characteristic wave complexes that are commonly distinguishable and correspond to physiological cardiac events. Physiological interpretation has been obtained by comparison with other cardiac measures such as electrocardiography (ECG) and phonocardiography. An example of BCG waveform can be seen in Figure 2.

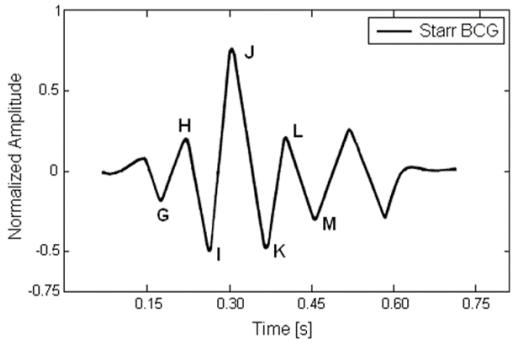

Figure 2: BCG waveform obtained from the Starr Ballistocardiograph [15]

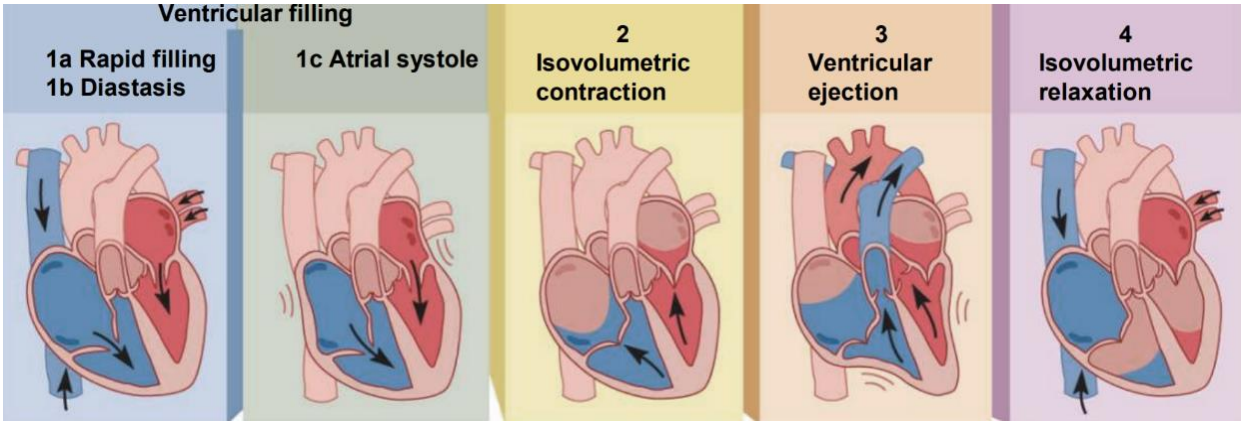

Figure 3: Events in a cardiac cycle (Reproduced after: The McGraw-Hill Companies, Inc.)

The following elements can be seen in a BCG wave complex (see Figure 3 for reference to the events of the cardiac cycle):

- *F wave*: pre-systolic wave, rarely seen unless the heart rate is slow, corresponds to the onset of atrial contraction (preceding 1c phase in Figure 3)
- *G wave*: downward wave corresponding to atrial systole (1c)
- *H wave*: it corresponds to the phase of isovolumetric ventricular contraction (2), right after electrical activation of the ventricles. It is an upward wave, and is associated with the abrupt deceleration in the flow of blood returning to the heart as pressure rises in the ventricles before the onset of ejection.
- *I wave*: sharp negative deflection corresponding to systole (3). It is due to the acceleration of blood into the pulmonary and ascending arch of the aorta.
- *J wave*: upward deflection, caused by reversing of direction in blood flow as it travels through the aortic arch. Its amplitude usually varies with respiration.
- *K wave*: it is a downward wave due to the deceleration of blood when encountering peripheral resistance, as well as the reduction of ejection velocity in late systole.
- *L-M waves*: corresponding of various diastolic events such as opening of the atrioventricular valves, and circulatory phenomena in the aorta.
- *N wave:* upward wave, corresponds to rapid ventricular filling (1a) [15].

It can be noticed how the direction of the recorded waves is opposite to the forces relative to the underlying events, which is explained by the fact that BCG is a ballistic force, thus a recoil force in the surrounding tissue occurring in reaction to the force of the blood mass.

The BCG signal is rich in information about cardiovascular activity, being a direct product of it. Therefore, both historically and currently, the main application of Ballistocardiography has been and still is the assessment and monitoring of cardiovascular function. The first and most basic information that can be retrieved from BCG is the heart rate (HR). It can be found in several ways. Peak detection is one of the used methods, and it can be achieved by using algorithms analogous to the ones used in ECG R-peak detection, with necessary adaptations. Often HR is also obtained by spectral analysis.

One application of BCG-based HR estimation is monitoring of Heart Rate Variability (HRV). HRV is the variation in time interval between successive heartbeats, a phenomenon influenced by the autonomic nervous system (ANS), in particular giving information on the activation of sympathetic and parasympathetic body rhythms [18]. A variety of cardiovascular, neurological and psychological conditions has been shown to relate with HRV patterns.
There have been attempts to assign clinical significance to characteristics of the BCG wave complex. Amplitude, timing and form of the BCG waves all play a role in assessment of cardiovascular health. Moreover, the BCG signal is closely related to heart contractility, and therefore gives an accurate indication of the heart's physiological age [15].
Although an abnormal BCG wave complex does, in general, indicate or predict cardiovascular disease, wave abnormalities are rarely specific to one particular disease. Moreover, because the BCG signal is characterized by a large inter-subject variability, and, on the other hand, a low intra-subject variability over serial measurements, recent applications have been focusing on over-time monitoring of changes in the same patient's cardiovascular health [19]. In this perspective, BCG monitoring can represent an early warning tool to elicit further analysis.
BCG is also widely applied to sleep monitoring. Sleep stages (wake state, deep sleep, REM sleep), are strongly related to ANS activity. As previously seen, the latter can be monitored through BCG by estimation of HRV. BCG-based sleep classification accuracy reaches 97.4% in healthy subjects, and 96.5% in obstructive sleep apnea patients [18].
Other applications include the combined measuring of BCG and other signals such as ECG and photoplethysmogram to obtain parameters such as blood pressure, pulse transit time, pre-ejection period, and left-ventricular ejection time.

3.4 Available Sensing Modalities

A broad choice of BCG sensing modalities is nowadays available. The historically used suspension table ballistocardiographs, described in Section 3.1, have over time been replaced with smaller, more sophisticated systems, allowing both for accurate and unobtrusive BCG sensing. Most traditional devices require mechanical coupling with the body. Of these, the most commonly used are weighing scales, load cells, MEMS accelerometers, piezoelectric and electromechanical film sensors. Recently, moreover, contactless BCG monitoring systems have been introduced, mainly using Doppler radar technology.

Weighing scale-based BCG measurement is a popular option, offering several advantages, such as the ability of recording a purely longitudinal BCG signal – which is typically of interest when the purpose is monitoring of cardiac activity – as well as low cost and wide availability. In [20], a simple commercial bathroom scale was proven effective in high-quality BCG monitoring, showing sufficient linearity of force-to-voltage conversion in the frequencies of interest for BCG (below 10 Hz for most purposes) for bodyweight biases ranging between 45 and 143 kg. However, disadvantages of this sensing modality include the high susceptibility to motion artifacts and floor vibrations, as well as a practical limit to test duration, due to the requirement that subjects maintain a still standing position throughout measurement.

Most weighing scales and load cells employed for BCG monitoring utilize strain-gauge sensors. These are sensing elements whose electrical resistance varies in a defined way according to the deformation imposed to the sensor by an applied stress. The stress-induced variation in resistance is converted to a change in voltage by connecting the strain gauge as component of a circuit, typically a Wheatstone bridge [18].

Micro-machined Electro-Mechanical Systems (MEMS) accelerometers are a convenient option, and can be incorporated in wearable BCG sensing devices, as they are small and lightweight. Such devices are typically secured to the body by adhesives, plastic mounting or embedded in textiles. MEMS technology consists in batch microfabrication of high-quality silicon sensors, integrated on-chip with their microelectronic readout circuit, which allows for reduced overall size (MEMS accelerometers have dimension in the order of few millimeters and weight of less than 1 gram), cost, and reliability. These accelerometers typically consist of a seismic mass, suspended between two plates by beams that act as mechanical springs, and are designed in such a way to restrain the mass' mobility to the axis of interest. The seismic mass and the upper and lower plates form two capacitances in correspondence to the air-gaps between mass and plates. When acceleration is applied to the seismic mass, this tends to move in the opposite direction, according to Newton's second law of motion, generating a change in capacitance proportional to the resulting change in thickness of the upper and lower air-gaps. This sensing modality offers the advantage of allowing continuous monitoring, possibly throughout daily activities and in any environmental setting. Moreover, most accelerometers-based devices allow tri-axial BCG acquisition rather than uni-axial [19]. Direct recording of acceleration, furthermore, provides an accurate basis for quantitative assessment of cardiovascular dynamics. In the case of accelerometers, an important aspect that demands attention is determining the sensor location, and measurement axes orientation (these are typically chosen so to span the three anatomical planes of the body, namely sagittal, coronal and transversal), as these aspects greatly affect the morphology and amplitude of the resulting BCG signal obtained. A standardization of procedure in this regard, still appears to be lacking [18]. One challenging aspect of this sensing modality might be ensuring the correct coupling of the sensors to the body throughout the entire measurement duration, as they might shift or detach with body movements.

Film-type sensors, namely Polyvinylidene Fluoride (PVDF) and Electromechanical Film (EMFi), are the preferred option when it comes to bed-based and chair-based BCG systems, because of their thin and flexible structure that allows easy integration in mattresses and cushions. Both mentioned materials are able to measure dynamic changes in externally applied force by generating a change in charge distribution when mechanically deformed, and are thus especially indicated for measuring signals of pulsatile nature such as BCG. However, the two materials have slightly distinct behavior due to their different internal structures. PVDF is a semicrystalline polymer with a solid and homogeneous structure, consisting of monomer units dispersed within amorphous regions. Piezoelectric properties are inferred to the material during manufacturing, when the material's molecular dipoles are given a fixed orientation via exposure to a high electric field, so that the material retains a net polarization. The two faces of the film are metallized so to provide electrodes. Upon compression or shear of the material by an external force, the dipoles' orientation changes, inducing an electrical signal on the electrodes. Because of its anisotropic properties, the material's response differs depending on the direction of the applied force. In general, PVDF is able to detect forces along all its three dimensions, with different sensitivity. The sensitivity of PVDF also depends

on the cross-sectional area encountered in the direction of the applied force, which means that typically the sensitivity is lower in the direction normal to the film's surface. EMFi, on the other hand, consists of a propylene sheet comprising of two external homogeneous layers and a central midsection full of flat air voids separated by thin propylene layers. As in the case of PVDF, the film is externally coated with metallic electrode layers. The interfaces between air voids and propylene are charged, forming macroscopic electrical dipoles that can be compressed in thickness by forces applied normal to the film's surface. Therefore, its sensitivity to forces applied in the normal direction is high, while sensitivity in the lateral directions is negligible. The sensitivity of an EMFi sensor may vary in different parts of the film due to irregularity of the air voids and local electrical discharges. Examples of measured force sensitivities of the two materials are: (12.6 ± 0.8) mV/N in the normal direction, and (223.9 ± 20.3) mV/N and (55.2 ± 11.9) mV/N in the two tangential directions for a 28 μm thick, 3 cm x 3 cm wide PVDF sensor; and (58.7 ± 16.5) mV/N in the normal direction for a 70 μm thick, 3 cm x 3 cm wide EMFi sensor [21]. Typical piezoelectric coefficients of the two materials are 25-250 pC/N for EMFi and 33 pC/N for PVDF in the normal direction [22]. When only the normal forces are of interest, EMFi is typically preferred over PVDF because of its higher flexibility, non-toxicity (while PVDF contains fluoride which is potentially toxic), and low cost.

Non-contact BCG systems are recently being explored, as the difficulty in maintaining an optimal mechanical coupling between sensor and body, and the influence of posture and motion on signal quality are among the main challenges of traditional BCG measuring. Microwave Doppler radar technology has been found particularly appropriate for the detection of low amplitude movements such as the ones of interest for BCG. Doppler radar technology detects movement of an object by measuring the frequency shift between the signal transmitted by the source and the one received after being reflected by the target moving body. The use of frequency modulated continuous Doppler radar is preferred, as opposed to fixed frequency continuous Doppler radar, as it allows for distinction of the subject's position from the small motions relative to BCG signal [23].

4. Hypothesis and Research Objectives

A human body subject to BCG oscillation may essentially be seen as a mechanical system under harmonic excitation, the source of this periodic oscillation being the beating heart. A vibratory system is, in general, characterized by three main kinds of elements: springs, responsible for the storing of potential energy, masses or inertial elements, responsible for the storing of kinetic energy, and dampers, responsible for energy dissipation. Each segment of the human body possesses some level of inertial, elastic and damping properties, the combination of which characterizes the way BCG oscillations are transmitted through the body and received at the sensing location in a baseline condition [24].
When a liquid mass is present in the body, an additional damping element, in this case a viscous damper, is added to the system. The fluid element opposes resistance to the oscillating body, causing increased energy dissipation. The amount of energy dissipated depends on several factors, including viscosity of the fluid, frequency of vibration, and velocity of the vibrating body[24].

The phenomenon of damping can be explained by comparing the two following situations.
An undamped system subject to a static harmonic force is described by the equation of motion:

$$m\ddot{x} + kx = F_0 cos\omega t \tag{4}$$

where $F_0 cos\omega t$ is the harmonic force, k is the spring constant, m the mass and x the displacement. The complete solution of this equation is:

$$x(t) = \left(x_0 - \frac{F_0}{k-m\omega^2}\right) cos\omega_n t + \left(\frac{\dot{x}_0}{\omega_n}\right) sin\omega_n t + \left(\frac{F_0}{k-m\omega^2}\right) cos\omega t \tag{5}$$

which essentially describes the sum of two sinusoids, one at the natural frequency ω_n of the system and one at the frequency of the applied harmonic force ω. The amplitudes of these sinusoids are entirely determined by the amplitude and frequency of the applied force and by initial conditions and constants of the system.
When a damping term is introduced, the equation of motion becomes:

$$m\ddot{x} + c\dot{x} + kx = F_0 cos\omega t \tag{6}$$

and the complete solution is now:

$$x(t) = X_0 e^{-\zeta\omega_n t} cos\left(\sqrt{1-\zeta^2}\omega_n - \varphi_0\right) + Xcos(\omega t - \varphi) \tag{7}$$

where the amplitude of the response oscillation X is equal to

$$X = \frac{F_0}{[(k-m\omega^2)^2 + c^2\omega^2]^{1/2}} \tag{8}$$

The formula can be rewritten as

$$X = \frac{F_0/k}{[(1-r^2)^2 + (2\zeta r)^2]^{1/2}} \tag{9}$$

with $r=\omega/\omega_n$ and $\zeta=c/c_c$ (where c_c is the coefficient of critical damping, for which the system returns to equilibrium without oscillation). From this formula it is evident that the amplitude of response vibration of a mechanical system subject to a static harmonic force is reduced by damping at any value of forcing frequency [24]. This can be visualized in the figure below.

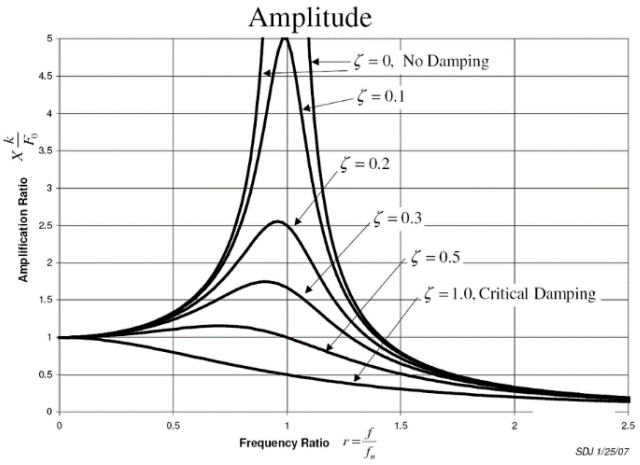

Figure 4: Amplitude ratio of a system under harmonic force at different frequency ratios and different damping ratios, image from Wikipedia.

This study's hypothesis is therefore that the presence of a liquid mass within the human body can be sensed unobtrusively through monitoring of the BCG signal, and specifically by comparing the energy of the signal at a baseline condition, to the energy of the signal in presence of an additional liquid mass inside the body. The signal energy recorded is expected to decrease in the latter case due to energy dissipation caused by the presence of an additional damping element.

Investigation of the above stated hypothesis entails several research objectives for the present study, namely:

- designing and conducting a human volunteer-based experimental study for acquisition of the required data, given that this is a pioneering study for this technique, and thus no suitable dataset is available from previous studies
- developing a feature able to accurately capture the decrease in signal energy caused by the presence of fluid accumulation in the body
- assessing the feasibility of the studied method for monitoring onset of fluid accumulations in the body, by investigating whether the hypothesized effect is observable in a systematic, significant and repeatable manner
- determining the optimal sensing modality for the present application, amongst the available options for BCG sensing, with preference given to those options which are most suitable for introduction within a clinical scenario
- selecting an optimal sensing location on the body, out of a focused set of anatomical locations, given that the simulated fluid accumulation in the present study is localized in the abdominal area (which is nevertheless a common location where pathological cases of fluid accumulation are frequently encountered)

A detailed description of the experimental methods used and of the signal analysis performed to fulfill the above research objectives is given in the fore coming chapters, dealing with experimental methods and signal processing and analysis methodology of the present study.

5. The Experiment

In order to investigate the use of BCG signal as a monitoring tool for internal fluid accumulation in the body, a human volunteer-based experiment has been designed and conducted. The experiment makes use of water intake by the participants as a method of inducing fluid accumulation, localized within the gastro-intestinal (GI) tract. The participant's BCG signal is thus recorded prior and after water-intake. The choice of such method is based on the following requirements:

- The method should induce a local accumulation of fluid within a confined cavity or hollow lumen in the human body, in a way that is conceptually comparable to the occurrence of pathological or abnormal fluid accumulation, such as the ones described in the Chapter 2.
- The method should be applicable to healthy human volunteers in a safe and ethical manner, with no adverse effect on their health.
- The method should be relatively controllable and reproducible.

The choice of conducting the experiment on human volunteers is due to the fact that the BCG signal itself is intrinsically dependent on human anatomy and physiology: the human heart is, in fact, the BCG signal actuator, and the response vibration of the body resulting in the acquired BCG depends on human anatomy and body composition. Any phantom-based or animal-based protocol would, therefore, not be appropriate for the present research, as it would not capture the real behavior of the signal under analysis, and would thus impede any conclusion on the practical feasibility of the studied technique.

The second requirement leads to the exclusion of any invasive method. This supports the choice of liquid intake as a simple and safe way of inducing a transient fluid accumulation in the GI tract of volunteers: drinking is a normal physiological activity, which does not entail risk for the volunteer.

The choice of intake liquid was also a matter of discussion. Because the range of envisioned applications of the studied technique is broad, it was decided not to focus the experiment on the perfect imitation of a particular pathological case, which would entail the selection of an edible liquid having density and viscosity as close as possible to those of the imitated bodily fluid. The experiment is, in fact, intended as a general feasibility trial for the explored technique. Therefore, it was decided to use water as intake liquid. The choice of water has several advantages. Firstly, it excludes any allergenicity considerations, posing the least possible limitations on volunteer recruitment. Moreover, water transition and absorption involves a minimum of gastric motility - which would possibly add noise to the received BCG signal in proximity of the location of fluid accumulation - as compared to other liquids containing nutritive substances requiring digestion [25].

To ensure reproducibility, a fixed amount of liquid is used for intake on an empty stomach. The amount of choice is 500 mL. This allows testing the present technique for a volumetric detection limit of 50% to 70% less compared to the detection limit of currently used hemorrhagic shock indicators (heart rate and blood pressure) [1]. The use of a fixed amount of water, furthermore, allows to investigate the variability

of the induced effect in volunteers having different body weights and body mass indices (BMI) (different ratios of water mass accumulated to total mass).

5.1 The Experimental Setup

The experimental setup was designed to combine use of different sensors for acquisition of the BCG signal unobtrusively. These include:

- Three galvanically isolated tri-axial accelerometers, attached to the body by use of a skin friendly, biocompatible adhesive (3M™ 1522 double-coated medical tape). The accelerometers used have sensitivity of approximately 25 ms^{-2}/V, slightly differing among the three axes. They were placed on the body such that the Y axis be perpendicular to the transverse anatomical plane and pointing towards the head, the X axis perpendicular to the sagittal anatomical plane and pointing to the subject's left, and the Z axis perpendicular to the coronal anatomical plane, and pointing outwards. The axes' orientation is illustrated in Figure 5.

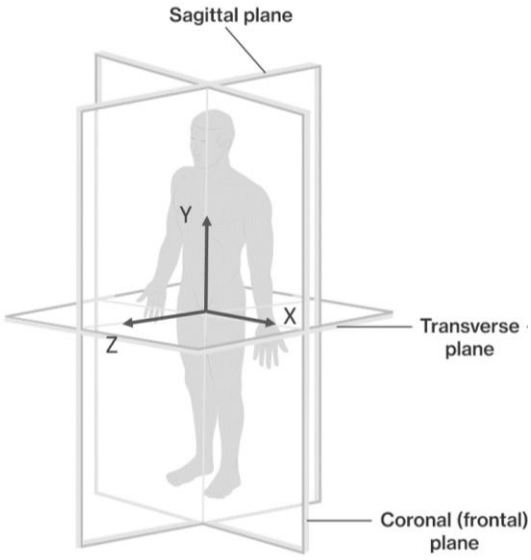

Figure 5: Orientation of the accelerometers' axes with respect to the body's anatomical planes.

- A custom-made weighing scale consisting of four strain-gauge type pressure sensors located at four corners of a squared plate, from which the total instantaneous weight of the volunteer is obtained by summation of the four measured values. Weight data were acquired from the scale via a USB connection running a LabView program, where measurements were stored at a sampling frequency of 10 Hz, with a resolution of 10^{-2} grams.
- An EMFi sensor mat (commercial name: EMFIT) placed on the bed, and located in correspondence to the participant's torso (depending on volunteer's anatomy, approximately extending from the shoulders to the lower back). The EMFi sensor used has a sensitivity of 25 pC/N and capacitive readout. A 2-cm thick foam layer was positioned in-between the bed and the sensor, to improve coupling between to the participant's back contour.

While the weighing scale data was independently acquired, the three accelerometers and the EMFIT sensor were connected to the same data acquisition system (PAK MKII), allowing synchronized signal acquisition. The data acquisition system operates at a sampling rate of 256 Hz, and includes an in-built digital anti-aliasing filter. The entire system is battery-powered due to safety considerations. This also minimized the possibility of polluting the acquired signals with 50 Hz noise from the mains hum. The complete setup is illustrated in Figure 6.

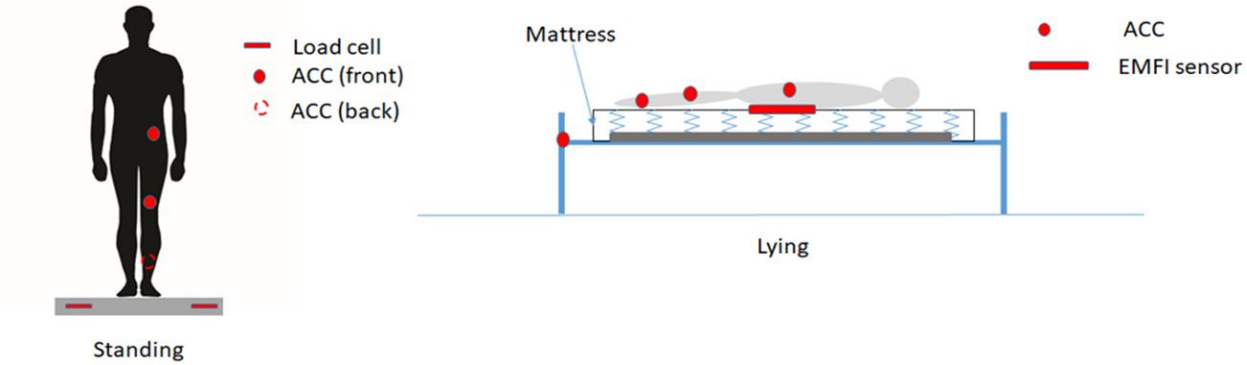

Figure 6: Schematization of the experimental setup. Accelerometer locations shown refer to Test Round 1

The sensors used have been selected in order to explore different sensing options for BCG. In fact, because it is the first time the BCG signal is employed for this specific purpose, it was not possible to *a priori* select one optimal sensing option. Clearly, for applications envisioned in a clinical setting, only the accelerometers or the EMFi mat would be feasible sensing options as they can be, respectively, embedded in hospital beds or attached to the patients' skin in an unobtrusive fashion. However, the weighing scale measuring modality was included to be used as a reference, since this was the modality used in preliminary informal experiments at Philips Research, which had initially demonstrated the explored effect.

5.2 The Study Protocol

The experiment consisted of two separate test rounds, with slightly different protocols, conducted on each participant on different days, separated by approximately and maximum seven days. This was decided in order to investigate intra-personal repeatability, while ensuring that physiological conditions of the participants would not change significantly between the two test rounds. This furthermore allows to investigate a higher number of sensor locations without compromising comfort of the participants. Nevertheless, to be able to investigate baseline variability within a single subject, and repeatability of results, some of the sensors are kept at the same location in both test rounds. The participants are asked to abstain from eating and drinking in the two hours preceding the test, and to empty their urinary bladder immediately before beginning of the test. In both test rounds, the initial part of the protocol is identical, and consists in taking repeated baseline measurements in two different monitoring positions: lying on the sensor-equipped bed, and standing on the weighing scale. Each recording has a duration of 3 minutes, and standing and lying measurements are interleafed for a total of four measurements. After this initial part of

the test is complete, the participant is asked to drink 500 mL of still water within a maximum 10 minutes time span. The second part of the experiment differs between the two test rounds:

- During Test Round 1, interleafed standing and lying 3-minutes measurements are recorded in the after-intake condition, with the same modality as for the baseline measurements.
- During Test Round 2, no standing measurement is performed. Instead, a 30-minutes continuous measurement is recorded with the participant lying on the bed. This choice was motivated by the fact that lying is a more representative modality for any envisioned clinical monitoring application. Therefore, it was decided to give it priority over the standing modality (which was mainly part of the study only as a trusted reference, because of prior use in preliminary experiments, though not as a preferred option because of obvious practical limitations to its feasibility as a continuous monitoring method). Moreover, this represents a situation where the participant's respiratory and cardiac rhythm is expected to be very stable, so to further decrease any possible noise contamination of the acquired signal.

During the measurements, participants are asked to remain as still as possible and to keep a fixed posture (arms along the sides, head straight), as movements and changes in posture significantly affect signal quality. Participants are also asked to remain silent during the recordings, as speaking also produces signal artifacts.

Different accelerometer locations were selected across the body from the chest down, and on the front and back. Again, *a priori* knowledge of an optimal sensing location for the purposes of this study was not available, being this a pioneer study for this technique. Thus, one of the research objectives was indeed selecting a measuring location suitable for capturing the BCG signal energy decrease caused by presence of intra-abdominal fluid accumulation. Locations adopted in the two test rounds are summarized in Figure 7. During Test Round 1, Accelerometer 1 was placed on the left side of the lower abdomen (approximately 3 cm below the navel height); Accelerometer 2 was placed on right outer thigh (ca. 2 cm above the knee cap); Accelerometer 3 on the back of the right calf (ca. 2 cm above the ankle). During Test Round 2, Accelerometer 1 was kept at the same location as for the previous round; Accelerometer 2 was placed on the left side of the upper chest (ca. 1 cm below the collar bone); Accelerometer 3 on the right side of the lower back (around the same height as Accelerometer 1). Due to limited number of available input channels to the PAK MKII data acquisition system, one of the accelerometers' axes had to be discarded in each test round. In order to make a decision in this regard, amplitude and signal-to-noise ratio (SNR) values – intended as percentage signal power of the BCG-relevant frequency band over the total signal power spanning the entire sensor bandwidth – of each accelerometer axis at the different measurement locations were obtained from preliminary tests data and compared. The least performing channels, according to these parameters, were identified to be the x acceleration component recorded on the knee for Test Round 1, and the x acceleration component recorded on the back for Test Round 2. These were, therefore, excluded from acquisition.

Figure 7: Accelerometer locations in the two test rounds. The dotted circles indicate that the accelerometer is placed on the backside of the body.

The Experiment Protocol was approved by the Philips Internal Committee for Biomedical Experiments (Reference: ICBE-2-27345, PJ-008199-NL Investigation of fluid accumulation induced density changes in the body), after verification that the Protocol and Data Collection comply with ethical, safety and privacy EU and National regulations, as well as internal Philips guidelines. The study was classified as a Type B study according to the internal Philips classification: this entails that the study be intended as a preliminary test for validation of an idea, preceding for instance clinical or preclinical trials, and involve a maximum of 15 volunteers recruited amongst Philips Employees. Before proceeding with the experiment, participants were informed in detail about the experimental procedure, purpose and data privacy notice, and were asked to sign an informed content.

5.3 The Dataset

Data were collected from a total of 15 volunteers amongst Philips employees, of which 9 males and 6 females. Age and BMI value of each participant was collected. The participants data is displayed in Table 2.

Table 2: Statistical distribution of participants' age, BMI, and monitoring duration

	Median	25th percentile	75th percentile
Age (years)	37	32.25	43.75
BMI	25.8	21.35	26.6
Duration of monitoring (minutes)	85.3	82.81	87.2

The time of the last meal consumed (minimum two hours prior to the test) was also noted before each test. Data were then acquired following the above-described protocol. Overall, for each participant, approximately 81 minutes of data were recorded (including both Test Rounds) according to protocol. Each of the measurements was acquired from several channels, namely: x, y and z channels of accelerometers 1

and 2, y and z channels of accelerometer 3, weighing scale for the standing measurements and EMFIT for the bed-based ones.

As explained in the protocol, this data is acquired under specific volunteer preliminary conditions, namely: volunteer is healthy (as per exclusion criteria of the study), and volunteer's stomach and urinary bladder are empty at the beginning of the test. Thus, the data obtained from each volunteer can be divided in two sets respecting the following assumptions:

- Data set 1 – No fluid accumulation is present in the GI tract. This will be from now on referred to as BL (baseline condition);
- Data set 2 – GI tract contains up to 500 mL of plain water. This will be from now on referred to as AI (after-intake condition).

6. Signal Processing and Feature Analysis

6.1 Visual Inspection of the Signals

The set of BCG data considered and analyzed in this project contains a wide range of signals having distinct characteristics, due to them being acquired from different anatomical locations, along different spatial axes, and from different sensor types. A first necessary step therefore involves visual inspection of the signals in order to understand the substantial differences and potential issues to be addressed in the pre-processing phase.

The weighing scale signals were used as a "trusted reference" due to established use in preliminary experiments, but are not a preferred option for signal selection because of the obvious non-suitability for use as a clinical monitoring tool, as it requires standing for a prolonged period of time.

The reported analysis will therefore focus on the signals acquired from accelerometers and EMFIT sensor. Figure 8 portrays an example of raw, unfiltered signals from the nine different acquisition channels used during Test Round 1, recorded in the lying position. In the figure, signals X1, Y1, and Z1 correspond to the three axes of accelerometer 1, signals X2, Y2 and Z2 to the axes of accelerometer 2; and Y3 and Z3 of the accelerometer 3, located as depicted in Figure 7 for Test Round 1. The axes' orientation is schematized in Figure 5.

The channels are acquired via the same DAQ system and completely synchronized; it can therefore be observed how different channels respond to the same BCG source. The signals recorded at the abdomen (accelerometer 1 and EMFIT) display a stronger respiratory component, clearly identifiable as the wide periodic oscillation with periodicity of approximately 5 seconds, to which the heart waveform is superimposed. It can also be noticed how the X and Y components of accelerometer 1 are majorly affected by respiration whereas in the Z direction the heart signature appears stronger. As expected, signal amplitude reduces with increasing sensor distance from the heart.

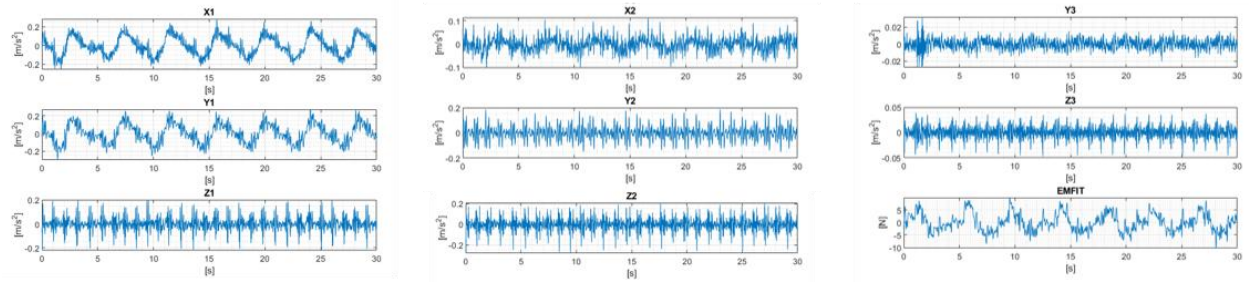

Figure 8: Synchronized segments of raw unfiltered signals from different acquisition channels during Test Round 1 in the lying position

Raw signals from the same volunteer acquired during Test Round 2 (approximately a week later) are displayed in Figure 9. The location of X1, Y1 and Z1 is the same as for Test Round 1, and signals' morphology and amplitude appear relatively consistent with Round 1. Signals X2, Y2 and Z2 are now located on the volunteer's chest slightly above the heart, and Y3 and Z3 on the lower back, as seen in Figure 11 for Test Round 2.

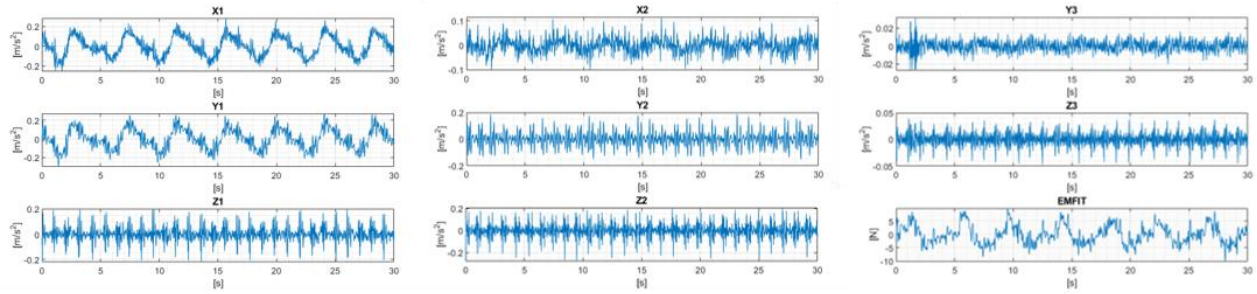

Figure 9: Synchronized segments of raw unfiltered signals from different acquisition channels during Test Round 2 in the lying position

Overall, the signals appear of good quality and low noise level. Unlike most established BCG applications, the focus of the present study doesn't lie in reconstructing the heart waveform or extracting cardiovascular parameters from the BCG signal, therefore commonly used signal processing practices do not necessarily apply to this case, and a careful, possibly more conservative choice must be made in discerning what range of frequencies to accept and what to filter out.

On the other hand, signals acquired in the standing position appear noisier. As can be seen in Figure 10, the respiratory and heart components are still perceivable in the most of the signal, but overall the signals appear more noise corrupted. This is expected: volunteers are asked to stand still for a relatively prolonged period of time, and the body is subject to much higher movement freedom compared to a lying situation. Moreover, the body must actively employ muscles to keep a fixed posture, which likely causes additional noise in the signal. It can be noted that the signals most affected by noise are Y3 and Z3, which is in line with the fact that they are placed close to the knee joint, which has a higher motion freedom compared to the other locations.

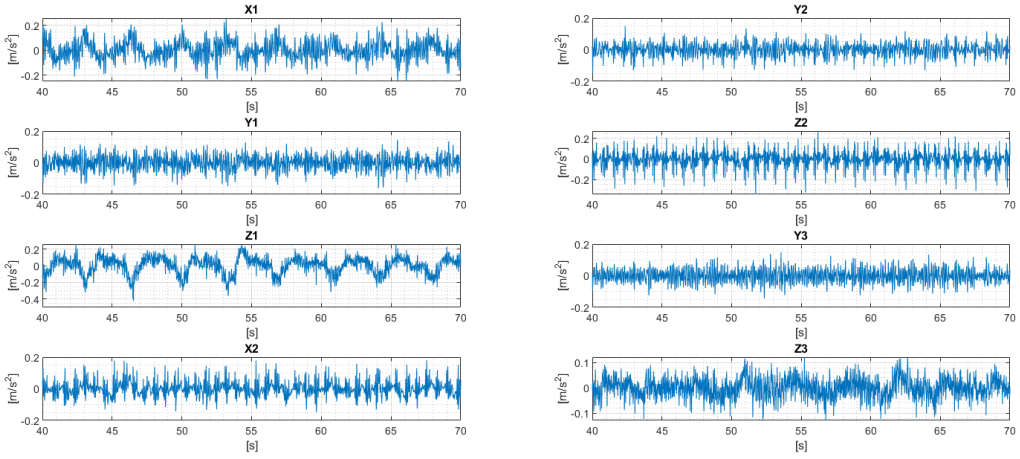

Figure 10: Synchronized segments of raw unfiltered accelerometer signals (EMFIT is not relevant to standing measurement) from different acquisition channels during Test Round 1 in the standing position

Another noticeable aspect is the substantial interpersonal variation of signal morphology and amplitude. In Figure 11, signals from two different study participants are plotted together for comparison. Both

respiratory and heart-related components are differently redistributed amongst the three axes for the two participants: while the participant plotted in blue shows a weaker respiratory component, only apparent along the Z axis, and stronger heart components in the X and Z directions, the participant plotted in orange has strong respiratory signature in the X and Y directions, and more prominent heart-related peaks along Y and Z. These differences are likely due to different respiratory patterns and anatomical differences (in this specific case the shape of the lower abdomen, which inevitably affects the axes orientation of the accelerometer).

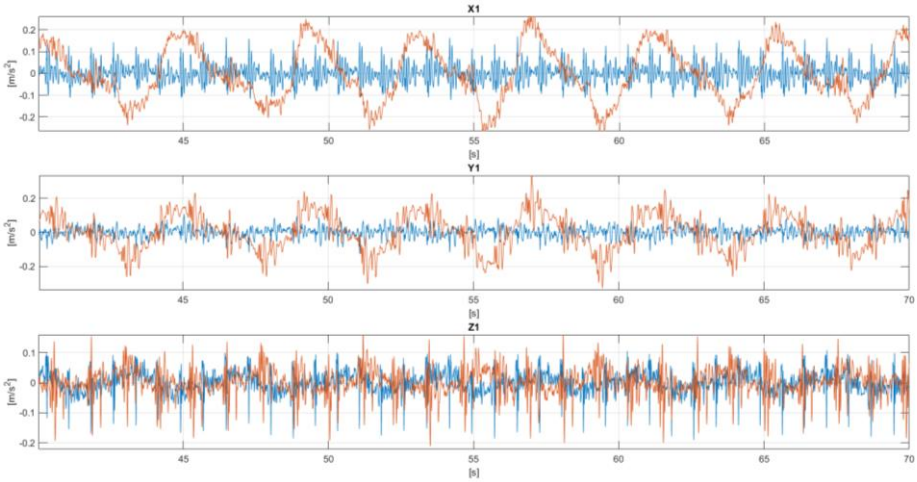

Figure 11: Accelerometer signals acquired from two different study participants plotted in different colors

These observations suggest that it might be advantageous to add three additional signals to the analysis, obtained by summation of the three axes for each accelerometer (only y and z in the case of accelerometer 3). This will allow to capture the complete BCG signal strength regardless of its repartition between the axes. One last observation regards the types of artifacts present in the signals. Since volunteers were asked to remain still and silent, the artifacts found in the signals are mostly due to small, sudden movements (e.g. twitching of the arms or legs). An example is provided in Figure 12.

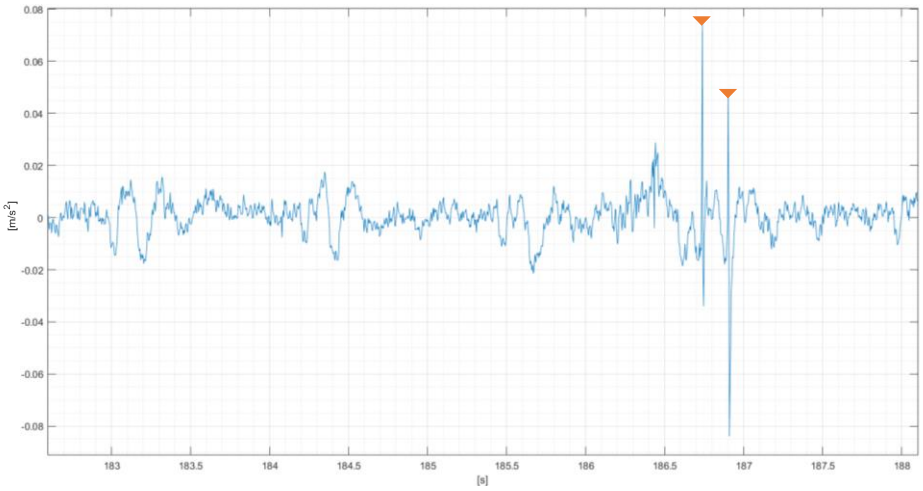

Figure 12: Example of an accelerometer signal segment containing movement artifacts, marked by orange triangles

In the standing signals, the initial and final few seconds of each measurement are corrupted by movements due to posture adjustments, as seen in Figure 13.

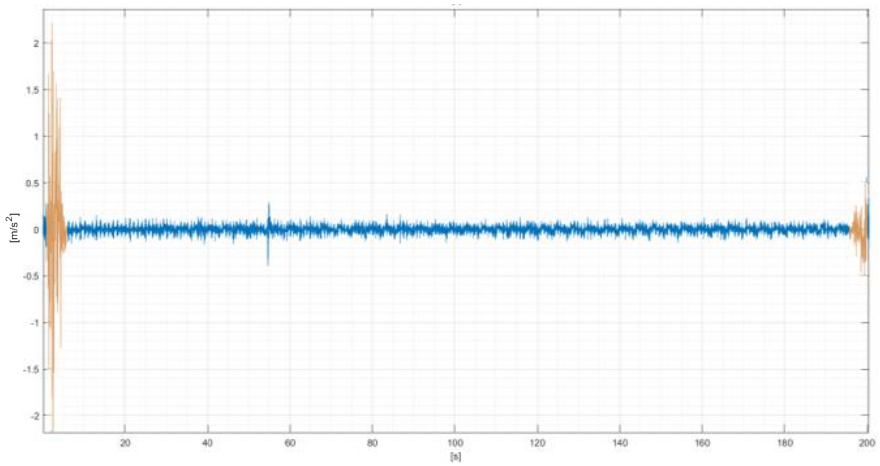

Figure 13: One complete standing measurement, with initial and last few seconds of measurement corrupted by movement artifacts (highlighted in orange).

6.2 Spectral Analysis

A powerful way of gaining deeper insight into the characteristics of the signals under analysis is observing their behavior in the frequency domain. For this purpose, it is required to estimate their power spectrum. Power spectrum estimation is an established tool in biomedical signal processing, and classical methods are based on taking the Fourier transform of the signal's estimated autocorrelation sequence. Essentially, this means correlating the signal with sinusoids at various frequencies, in order to produce a set of coefficients that characterize the signal power in the frequency domain.

When making use of these tools, a number of assumptions are made about the nature of the signals analyzed. In particular, the signals are assumed to be real-valued stochastic processes with Gaussian probability density function. This implies that the density function of the random variable x be of the form:

$$f(\alpha) = \frac{1}{\sigma_x \sqrt{2\pi}}\, e^{-\frac{(\alpha - m_x)^2}{2\sigma_x^2}} \tag{10}$$

This means that the probability density function of the variable is entirely defined by its mean m_x and autocorrelation σ_x. These assumptions are widely accepted for signals of the type analyzed. Moreover, it is common practice to make use of Fourier-based power spectral analysis even with signals that are non-Gaussian, although complete characterization is not ensured [26].

Another assumption made is that the signals be Wide-Sense Stationary; this implies that the processes have constant mean, autocorrelation function $r_x(k,l)$ only dependent on the lag k-l, and finite variance. The signals under analysis are of duration of approximately 3 minutes each, and recorded in very steady conditions for the volunteer. Stationarity is therefore a safe assumption.

Because the autocorrelation function is not known a priori, it has to be estimated by assuming signal ergodicity, a property that assumes the ensemble average of a random process can be consistently estimated by its time average. The signal power spectrum is thus obtained as follows:

$$\hat{P}(f) = \frac{\Delta t}{N}\left|\sum_{n=0}^{N-1} x_n e^{-i2\pi f n}\right|^2, \quad -1/2\Delta t < f \leq 1/2\Delta t \tag{11}$$

where Δt is the sampling interval. In order to improve the power spectral density estimate, windowing and averaging is used according to Welch's method. This means that instead of estimating the power spectrum of the whole sequence, the spectrum of many overlapping segments of the signal is obtained separately and then averaged. The main advantage of this technique lies in the fact that averaging many segments provides a smaller variance in the estimate, while allowing segments to overlap increases the estimate's resolution [26], [27]. In this case, 20 seconds-long Bartlett windows with 80% overlap are used.

Inspection in the frequency domain, first of all, allows us to observe that the signals collected contain no power mains hum interference at 50 Hz (thanks to the use of a battery-powered acquisition system), and that all significant power density is contained within frequencies below approximately 25 Hz. This permits downsampling of the signals at 50 Hz (twice the maximum frequency of interest, according to Nyquist Sampling Theorem) to reduce data size.

Furthermore, interesting observations can be made by comparing the spectra of all signals. As seen in Figure 14, the spectra of X1, Y1 and Z1, as well as EMFIT, are dominated by two main low-frequency peaks: one taller, below 0.5 Hz, corresponding to respiration; and a second, shorter and at approximately 1 Hz, corresponding to the heart rate (sometimes followed by its second harmonic).

However, these frequency components are almost absent in the spectra of the two accelerometers on the legs. Instead, higher frequency components of the BCG waveform are transmitted at these locations.

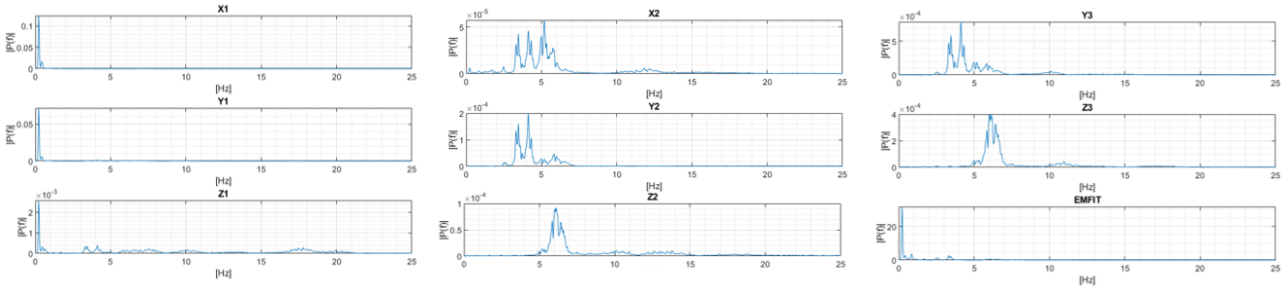

Figure 14: Spectra of signals acquired during Test Round 1 in lying position

By plotting the spectra in on a logarithmic scale, we see that the same higher-frequency components are present in X1, Y1, Z1 and EMFIT (see Figure 15). These appear to be selectively enhanced along different axes at the leg locations (e.g. close to and smaller than 5 Hz for Y, close to and higher than 5 Hz for Z in both accelerometer 2 and 3).

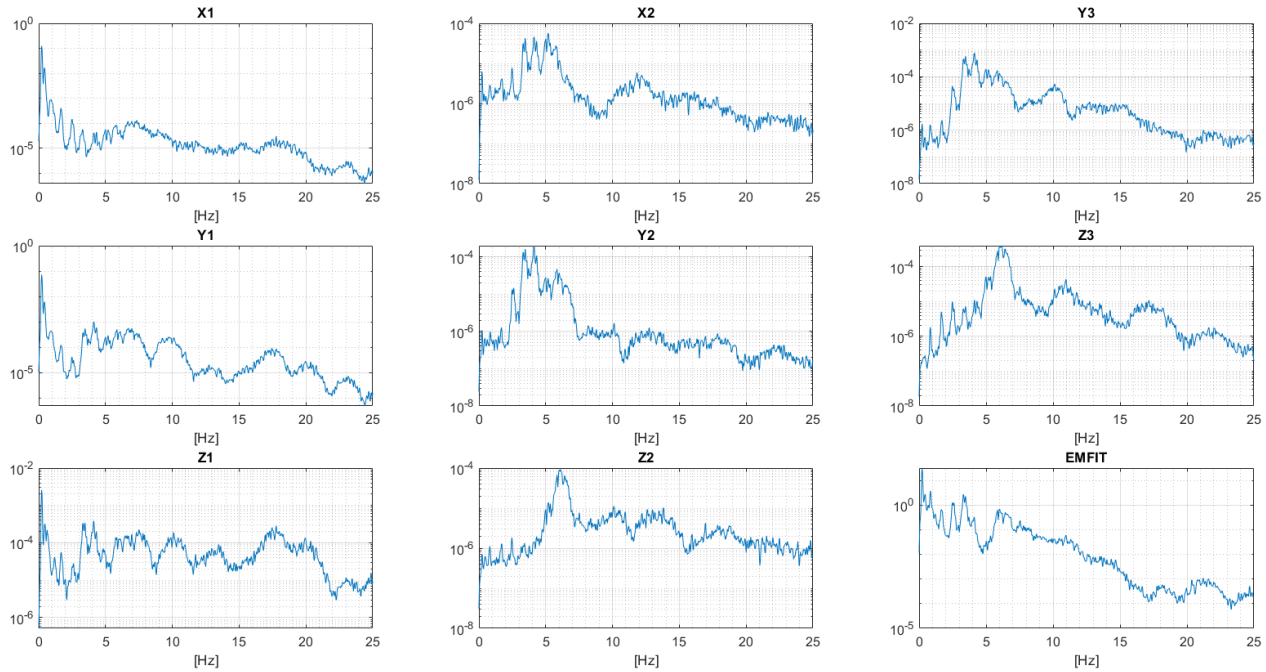

Figure 15: Spectra of signals acquired during Test Round 1 in lying position, with y-axis is plotted in base 10 logarithmic scale.

Similar behavior is observed for the signal locations in Test Round 2. In the standing position, these spectral peaking bands appear slightly shifted towards higher frequencies, as seen in Figure 16.

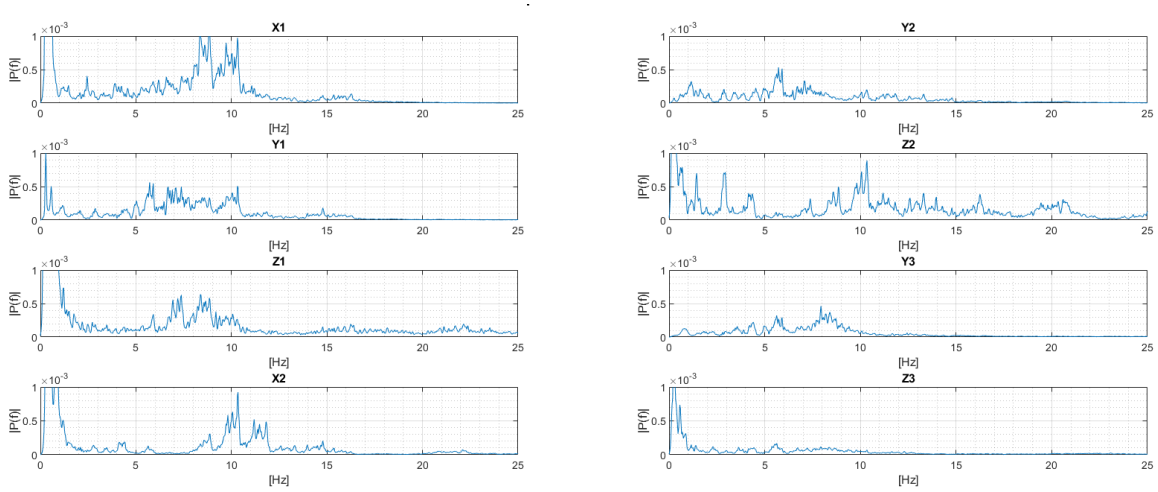

Figure 16: Spectra of signals acquired during Test Round 1 in the standing position, with y-axis of the plots rescaled so to focus on the higher frequency components.

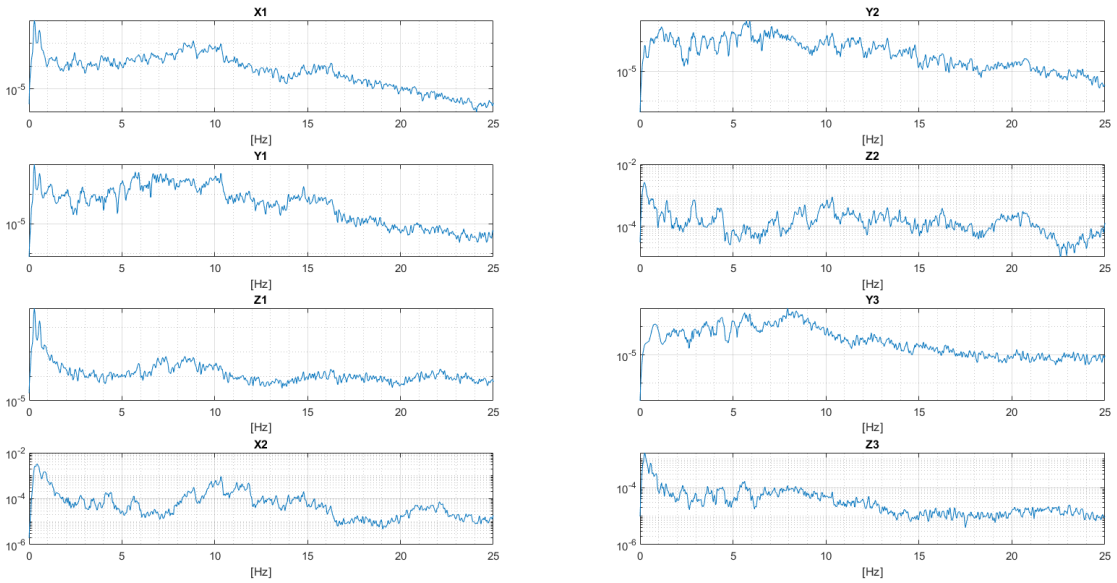

Figure 17: Spectra of signals acquired during Test Round 1 in standing position, with y-axis plotted in base 10 logarithmic scale.

These higher frequency peaks have been reported in other BCG studies, such as the one shown in Figure 18, taken from [28].

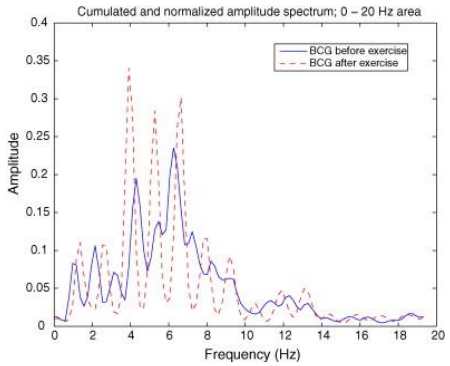

Figure 18: BCG power spectra reported in [28]**.**

The reason why particular frequency bands of the BCG signal are enhanced at some locations rather than others, and along some axes rather than others, might have to do with the interaction of certain frequencies of the BCG signal with the natural frequencies of the body itself.

The natural frequency of a system is defined as the frequency at which the system would oscillate if left free of external forces after initial disturbance. When a system is harmonically excited at frequencies close to its own natural frequency, a condition known as resonance occurs: the amplitude of the response oscillation is maximal, and, if left free of damping, would increase indefinitely in the limit of the forcing frequency approaching the natural frequency [24].

A similar concept has been proposed in [29], suggesting that the heart's pulsatile efficiency be maximized due to a condition called "frequency matching", at which the heart rate and its harmonic modes match the fundamental natural frequencies of the arterial system.

A vibratory system has as many distinct natural frequencies as it has degrees of freedom, it is therefore reasonable to assume that these natural frequencies might be slightly different along different axes, which seems to reflect the observations made on the signals collected in the present study.
A study where human volunteers were made to stand and sit on a vibrating slab, in order to obtain an experimental value for their fundamental resonant frequency, found this to be in the range of 3 to 7 Hz at magnitudes of vibration higher than 0.1 m/s^2, and possibly higher at lower magnitudes of vibration [30]. The study also found this frequency to be slightly higher in the standing condition compared to sitting. These findings seem to be in accordance with the present data.
As one can observe from Figure 4 reported in Chapter 4, the reduction in amplitude ratio due to damping is especially significant near or at the natural frequency of a system [24]. This suggests that these higher frequency bands observed in the spectra be of particular interest for the purpose of this study.

6.3 Pre-processing: Artifact Removal and Noise Filtering

Based on the observations made through visual inspection and spectral analysis, the following pre-processing steps have been taken.
Firstly, all signals have been downsampled to 50 Hz, and the first and last ten seconds of recordings have been discarded from each measurement, because mostly corrupted by artifacts due to posture adjustment. During data acquisition, this had been taken into account, so that the majority of signals are still approximately 3-minutes long even after removal of the first and last segments.
Furthermore, movement artifacts of the type shown in Figure 12 have been removed with the following procedure: 1-second windows are shifted along the signal, and the peak-to-peak amplitude of each window is computed. The mean peak-to-peak amplitude over the 3-minutes measurement is computed, and then the value for each 1-second window is compared to the mean. If the peak-to-peak amplitude of an individual window is larger than twice the mean value for the entire measurement, an artifact is detected and the 1-second segment is discarded. In Figure 19, the peak-to-peak amplitude per second of one measurement is shown, with one instance of artifact marked by the orange triangle.

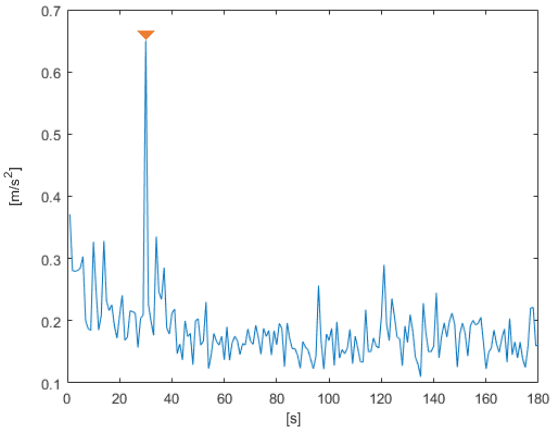

Figure 19: Peak-to-peak amplitude per second of one 3-minute measurement: the second at which the artifact is detected is marked by an orange triangle

When a window is discarded, the trailing part of the signal is shifted and concatenated with the preceding signal segment. In Figure 20, two examples are given of the technique applied: signals in blue are the original signals, while the orange ones are after artifact removal has been applied. This approach has the disadvantage of losing perfect synchronization of the signals, because the artifacts often differ among axes and locations, thus the segments removed do not always coincide for all signals. However, this is not important for the energy-based features used in the analysis, which will be described in Section 6.5. What is most important is maintaining the authenticity of signals' energy, which is ultimately the focus of this study. Therefore, any approach aimed at filling in the removed segments to maintain synchrony, such as interpolation, would not be appropriate, as it would generate false values of energy in those windows. Moreover, artifacts presence was very limited, so that the amount of data was not particularly affected by this procedure (typically, not more than 2 seconds – if any – would be removed out of a 3-minute segment).

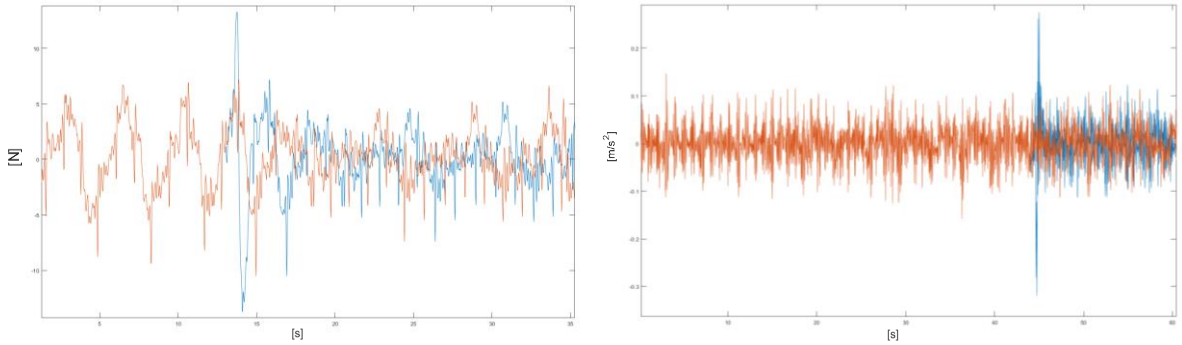

Figure 20: Two examples where peak-to-peak amplitude-based artifact removal is used. On the left is a signal from the EMFIT sensor, on the right from an accelerometer. The plots in blue represent the original signals, while the signals after artifact removal is applied are superimposed in orange.

As for noise filtering, the issue is not knowing *a priori* what exactly has to be considered as *noise* for the present application. As seen in the previous sections, signals acquired are in general very clean, and even in the instance of noisier standing signals, a solution cannot be as simple as band-pass filtering with some arbitrary band, because it might mean losing important information for the purpose of this study. The approach chosen is therefore that of generating distinct sub-features having a common fundamental basis, but involving different pre-processing and filtering steps. This will allow discerning what technique is best suited for this specific application, on the bases of its performance as a feature in capturing the effect of interest (i.e. the decrease in signal energy due to presence of fluid accumulation). A detailed description of each of the techniques used in generating such features is given in Section 6.5.

6.4 Heart Rate Extraction

Although extraction of the heart rate is not of central focus for the present study, it is nevertheless advantageous to obtain the instantaneous as well as average value of heart rate for each participant, in order to be able to identify or exclude any heart-rate dependency of the results obtained.
The method used for heart rate extraction is the following. Windows of 30 seconds, with 10 seconds overlap are shifted along the signal, and one value of heart rate is found for each window using the method hereby

described. A sixth-order Butterworth band-pass filter is applied to each signal window, with passband 0.8 to 2 Hz. The normal resting heart rate for adults is typically defined to be between 1 and 1.6 Hz (60 to 100 bpm). In order to preserve this frequency band without attenuation, the filter is designed for a slightly larger passband, as shown in Figure 21.

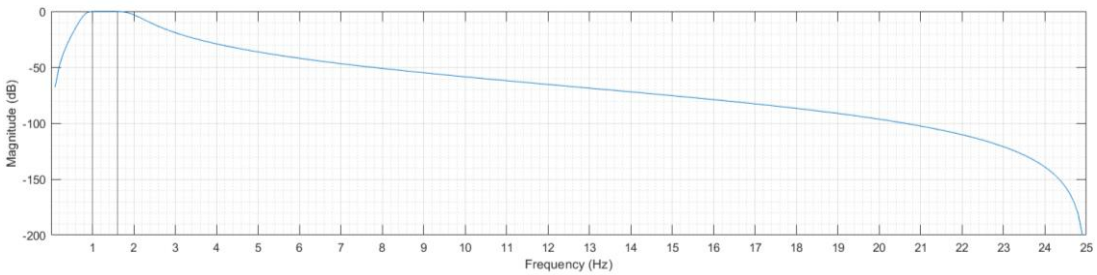

Figure 21: Magnitude to frequency response of the 6-th order Butterworth band pass filter designed for heart rate extraction. The two black vertical lines mark the normal resting heart rate band (1 to 1.6 Hz).

Butterworth filters are designed to provide the sharpest roll-off possible without introducing ripple in the pass-band, for this they are commonly known as *maximally flat filters* [31]. A Butterworth filter is therefore a good choice when wanting to preserve signal characteristics in the passband as faithfully as possible, such as for the present case. Once the filter coefficients have been obtained, a forward-backward filtering technique is used in order to ensure zero phase distortion. For an input signal *x(n)* and filter *h(n)*, implementation of this technique involves the following steps:

$$z_1(n) = h(n) * x(n), \tag{11}$$

$$z_2(n) = h(n) * z_1(-n), \tag{12}$$

$$s(n) = z_2(-n). \tag{13}$$

Where *s(n)* is the filtered output signal. The filter magnitude function is now the squared value of the original filter magnitude function, and the filter order is twice the original filter order [26].

After the signal has been filtered, the power spectrum is estimated with a similar procedure as described in Section 6.1. This time, however, the spectrum is obtained for each individual window (without averaging). The signal autocorrelation sequence is obtained, and after normalization by the mean, a Hanning window is applied to the signal before applying the Fourier transform. The use of a Hanning window reduces undesirable effects common in power spectrum estimation such as smearing and leakage [26].

After the power spectrum is obtained, the highest spectral peak is identified and the corresponding frequency is taken as the heart rate value for that particular window.

From spectral analysis it is clear that amongst the signals available, the most apt to heart rate extraction are signals from accelerometer 1 (located on the abdomen), from accelerometer 2 in Round 2 (located on the chest), as well as EMFIT signals. These present a stronger heart rate component. The use of signals obtained from the sum of all three accelerometer axes is advisable since, as shown in Section 6.1, it is not always the same axis to retain the strongest heart rate signature. Figure 22 shows an example of this procedure, applied to the signal obtained from the sum of the three axes of accelerometer 1. In the first plot is a 30-second window containing both the original and band-pass filtered signal (in blue and orange respectively). The second plot shows the heart rate values calculated over an entire 3-minute measurement, each point corresponding to one 30-seconds window (the third point corresponds to the window shown in

the first plot). The third plot shows the power spectrum of the window shown in the first plot, from which the heart rate value was obtained.

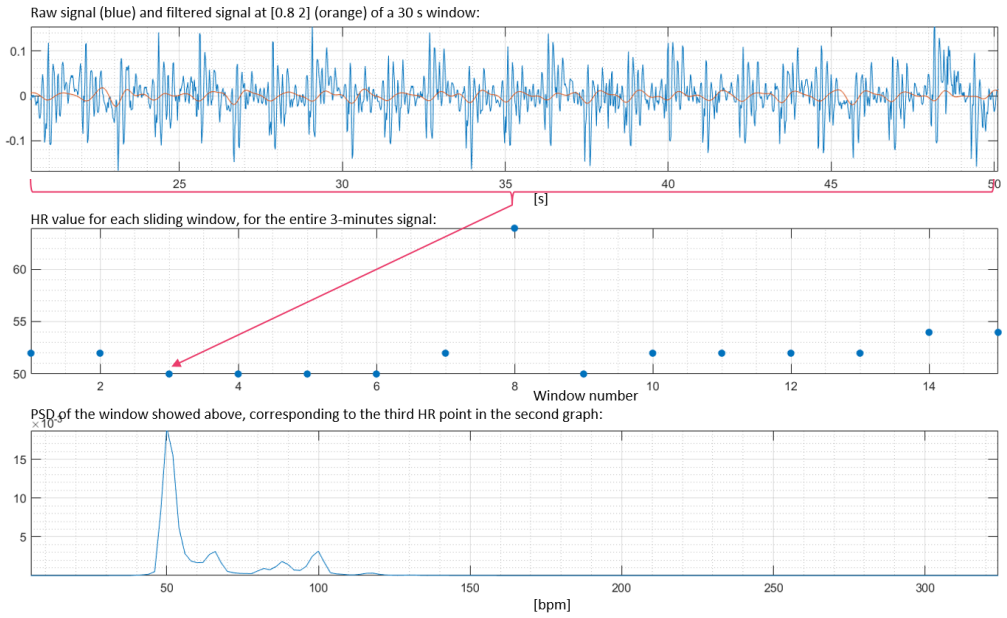

Figure 22: Example of heart rate extraction procedure

To calculate the participants' average heart rate during one Test Round, the median value was taken from each 3-minute measurement (so to be less affected by outlier windows), and finally the values from all measurements were averaged to obtain the average heart rate. Using the values obtained from accelerometer 1, it was possible to compare values obtained from Test Round 1 and Test Round 2 for each participant. The results were very consistent, with a median difference between the two rounds of less than 3 bpm.

6.5 Feature Exploration

It is now time to define signal features that will allow to capture the hypothesized drop in signal energy from BL condition to AI condition (respectively, 'baseline' and 'after-intake' as per definition given in Section 5.3). Firstly, it is necessary to define a quantity able to describe signal energy. The signals under analysis consist in oscillatory random processes alternating around a constant mean (i.e. zero). The most established way of defining energy for this type of signals is the *standard deviation* (σ). This describes the average power of signal deviation from the mean. The deviation of the *i-th* sample from the mean is defined as $|x_i - \mu|$. The power of deviation is defined as the square of its value. Therefore, the overall standard deviation of an *N*-samples signal is defined as:

$$\sigma = \sqrt{\frac{1}{N-1}\sum_{i=1}^{N}|x_i - \mu|^2} \quad (14)$$

One limitation of standard deviation is its sensitivity to outliers. One way to reduce this effect is computing the standard deviation of short windows instead of the entire measurement. This will allow having a higher number of data points, of which only one will be affected by a hypothetical outlier, instead of the entire measurement. Another quantity which can be used, this time to characterize the signal amplitude, is the *median absolute deviation* (MAD). It computes the absolute deviation of each sample from the median, and then takes the median value from the sequence, as follows:

$$MAD = median(|x_i - median(X)|) \quad (15)$$

Where X is the complete signal, and x_i the *i-th* sample of X. Because this estimate uses the median instead of the mean, this measure is more robust against the influence of outliers.

It is therefore decided to use these two quantities as base features for the analysis. As previously mentioned, a set of sub-features has been developed on the basis of these two primary features, each involving different pre-processing and filtering steps, in order to explore which signal components contain the most relevant information for the present purposes, and best isolate the damping effect of interest. All features have been initially computed on sliding windows of 10 seconds with no overlap, leaving as a later step the task of optimizing window length and percentage of overlap. The complete list of features is hereby described.

- *Feature 1 – Basic σ feature*. Standard deviation is obtained of the complete signal, without pre-processing.
- *Feature 2 – σ of the signal excluding respiration band*. Before computing standard deviation, the signal is filtered with a 6th-order high-pass Butterworth filter, with cutoff at 0.6 Hz. This filters out the respiratory component of the BCG signal. Respiration-induced amplitude variation is most probably a confounding factor for calculation of the BCG signal energy. Moreover, because it has been observed that respiration affects different signals in different measure, filtering it will make signals more comparable to one another.
- *Feature 3 – σ of the signal excluding respiration and heart-rate band*. This feature is even more selective, focusing on the higher frequencies of the BCG signal. A 6th-order high-pass Butterworth with cutoff at 2 Hz is used to filter the signal before standard deviation is computed.
- *Feature 4 – σ of the 'resonance band'*. Based on the observations made in Section 6.2, it appears that there is a particular frequency band containing considerable power spectral density. This band is thought contain those frequencies of the BCG signal which closely match the body's natural frequencies, thus entering a condition of resonance which enhances the response vibration. Because the effect of damping is known to be especially significant close to resonance, it might be beneficial to focus on said frequency band. Based on observation of the signals' spectra, and on the results reported from an experimental study [30] on human resonant frequency, the pass-band for this feature has been defined to have cutoffs at 2.5 and 7.5 Hz. The filter used is again a 6-th order Butterworth.
- *Feature 5 – σ of the signal denoised with Empirical Mode Decomposition (EMD).* As discussed in the previous sections, it is not intuitive to discern from the spectra of these signals a specific rage of noise-corrupted frequencies. Therefore, simple low-pass filtering is not advisable and a different approach must be adopted and tested for efficacy. This feature utilizes an EMD-based denoising technique. EMD is a time-frequency analysis tool designed to deal with non-stationarity and non-linearity of signals such as biological ones. It is a self-adaptive and data-driven algorithm that

decomposes a signal into its oscillatory modes, called intrinsic mode functions (IMF). These are essentially fast to slow sub-band oscillations contained in the signal. IMF are defined as functions satisfying two criteria: have same number of extrema and zero crossing, or differing by at most one; and have mean value of the upper and lower envelope (defined by local maxima and minima respectively) equal to zero at any point. The decomposition into IMF is obtained with the following procedure, known as *sifting*. The signal's local extrema are identified, and local maxima and minima are connected by a cubic spline line to form the upper and lower envelope, respectively. The mean m_1 between the upper and lower envelope is calculated and the first component h_1 is obtained as follows: $X(t) - m_1 = h_1$. If h_1 satisfies the IMF criteria, it is stored as IMF, otherwise the process is repeated by taking h_1 as data, until the IMF criteria are met. To proceed finding the next IMF, the residual signal is obtained by subtracting the IMF from the data. The residual is then used as new data, and the above procedure is repeated. The whole process is iterated until some stopping criterion is met. Sometimes this consists in limiting the standard deviation of the difference between two consecutive results of the sifting procedure to some set threshold. Otherwise, the process can be stopped once the residual becomes a monotonic function from which no IMF can be extracted. Eventually, the decomposed signal is such that:

$$X(t) = \sum_{i=1}^{N} c_i + r_n \tag{16}$$

where c_i are the N intrinsic mode functions and r_n is the last residue [32]. Observation of the IMF can give insight into which set of modes contains useful information, and which other can be discarded as noise, and excluded from signal reconstruction. An example of EMD decomposition of one signal from the data set under analysis is shown in Figure 23.

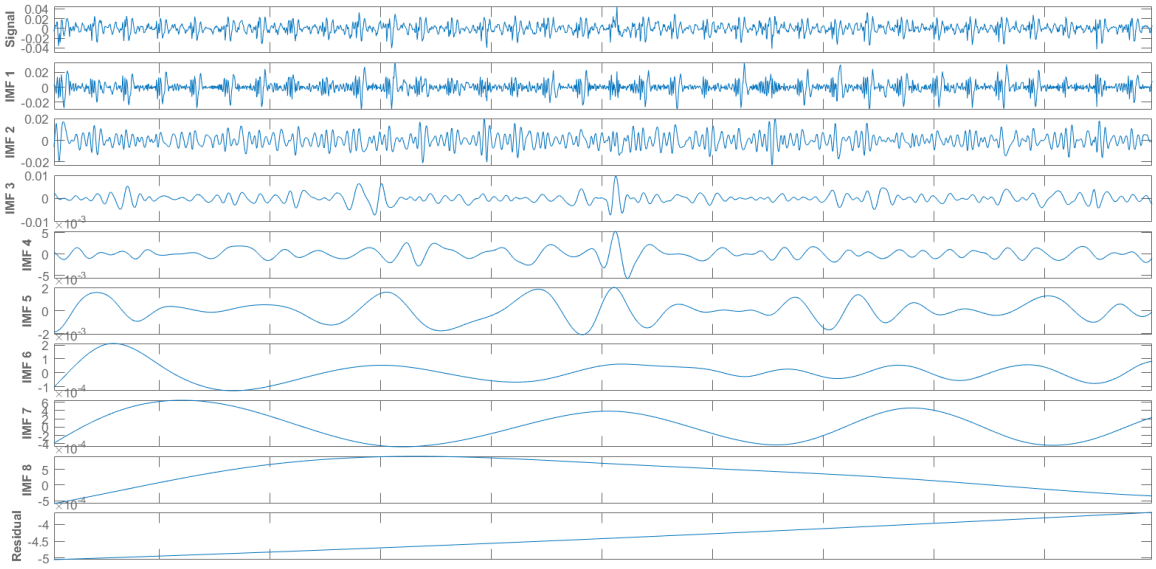

Figure 23: Empirical mode decomposition of a BCG signal

The present feature is calculated by decomposing the input signal with EMD and then reconstructing the signal, to be used for calculation of the standard deviation, from the IMF set after discarding the first and the last three IMF. The first IMF contains the heart rate signature together with very high frequency tiny oscillations that in the original signal are superimposed to

the BCG waveform. The latter are likely of random nature and can be considered as noise. At the same time, discarding the first IMF also allows exclusion of the heart rate while retaining the higher frequency components of the BCG waveform, as already done for Feature 3. The last three IMF contain very low-frequency oscillations identifiable as baseline drift, and are for this reason discarded as well. Figure 24 shows an example of a noisy signal segment (from standing data) with the corresponding signal reconstructed using the described technique.

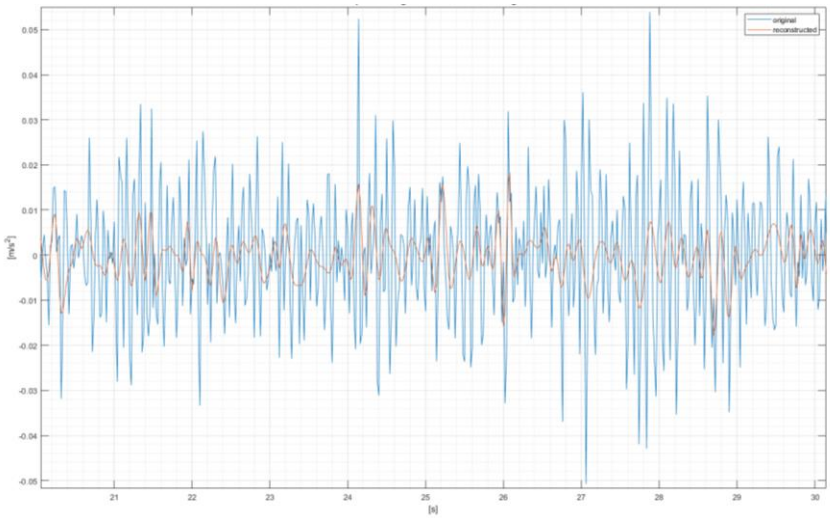

Figure 24: Segment of signal denoised using EMD (in orange) with the corresponding original signal (in blue)

One disadvantage of this approach is that the algorithm is completely unsupervised, which implies having no control over the feature and no opportunity for optimization.

- *Feature 6 to 9 – σ of, respectively, IMF 2, 3, 4 and 5.* These features are based on EMD, and selectively compute the standard deviation of one individual IMF from the set. Only the second to fifth IMF are considered, for the reasons explained above.
- *Feature 10 to 18 – MAD-based feature set.* These nine features involve the same pre-processing steps as features 1 to 9, but compute the energy using MAD instead of σ.

All features have been calculated from each of the 12 signals available (the 8 accelerometer channels, EMFIT and the additional 3 signals obtained by the sum the axes for each accelerometer). The next steps in the analysis will consist in quantifying feature performance, in order to select the most promising feature among the complete feature set, to use as a starting point for further feature optimization. Contextually, the performance of each acquisition channel will be compared in order to indentify the most appropriate signal axis, monitoring location and sensor type.

6.6 Preliminary Feature Selection

In order to proceed with the selection of a preferred feature from the above-described feature set, it is necessary to define the criteria that will be used for quantifying a feature's performance. Ultimately, the desired feature should be able to highlight the hypothesized decrease in signal energy from BL to AI

condition in a consistent way, ideally for all participants. The quantity to look at, for quantifying feature performance, is, therefore, the amplitude of the difference in feature values between the BL and AI condition. However, because the features are calculated on short-time shifting windows, we actually have a time series of feature values for each measurement. We must therefore quantify this difference in statistical terms, in order to describe both the mean difference between data points of the two sets (BL and AI), as well as the variance of the two sets. One way of doing this is looking at the value of the Student's t-test statistics (t_{stat}). This is calculated as follows:

$$t_{stat} = \frac{m_{BL} - m_{AI}}{\sqrt{\frac{v_{BL}}{n_{BL}} + \frac{v_{AI}}{n_{AI}}}} \quad (17)$$

Where m_{BL} and m_{AI} are, respectively, the means of the BL and AI data sets, v_{BL} and v_{AI} the respective variances, and n_{BL} and n_{AI} the number of data points in the two sets. This value will be larger the larger the difference in means between the two sets (i.e. the larger the decrease in energy observed by the feature), and the smaller the larger the variances in the two sets. The so obtained t_{stat} value is typically used in the context of an independent two-sample Student's t-test. This is a parametric statistical tool to test the null hypothesis that the mean difference between two samples is statistically zero, for some chosen confidence interval. If the test fails to reject the null hypothesis, there is statistically no difference in the means of the two samples. This test can therefore be employed in the feature analysis to determine, for each participant, whether a feature shows a significant decrease from BL to AI condition. This will allow quantifying the number of participants for which each feature performs in the desired fashion, as an additional selection criterion, together with the average of the t_{stat} values obtained for each participant, which in turns will quantify the amplitude of the decrease observed. An independent two-sample Student's t-test makes use of the following assumptions:

- Mean of the two samples being compared are assumed to follow a normal distribution. The test is, nevertheless, highly robust to small deviations from this assumption. For large samples especially, the test is typically considered valid for any type of sample distribution [33].
- The two samples are assumed to have equal variances. With equal sample sizes in the two groups, the test is highly robust to unequal sample variances. However, there also exists a variant of the Student's t-test (sometimes called Welch' s t-test) which is insensitive to equality of the variances. In the present case, it is chosen to opt for this latter variant to strengthen the test robustness, even though the variances are likely to be very similar in the two datasets.
- The data used is assumed to be sampled independently from the two populations compared. In the present case, the two 'populations' consist in the BL and AI data sets. Because we compare the individual data sets from one participant at a time, this assumption is verified.

It is common, for this kind of tests, to use a 95% confidence interval (or α=0.05) to reject the null hypothesis. In this case, because we are interested in specifically testing the alternative hypothesis that the mean of the BL sample be higher than that of the AI sample, a right-tailed t-test can be used. In this case, however, the α value must be lowered to 0.025 (half as much as the corresponding α in the two-tailed test) in order to maintain the same level of confidence. Because the analysis includes considering the value of t_{stat}, which becomes negative in the case of an opposite behavior to the one expected (i.e. an increase in energy from BL to AI), we don't run the risk of overlooking this possibility by using a right-tailed test.

Finally, it was chosen to additionally test the same hypothesis using the Wilcoxon Rank Sum test. This is a non-parametric test, which does not assume normal distribution of the samples. Instead of comparing the

mean of the samples, it compares medians [34]. We expect that, in the case that assumptions made for use of the Student t-test are appropriate for the present dataset, outcomes of the two tests should be very similar.

Based on the knowledge that water retention duration in the GI tract might be relatively short, it was decided that only the AI measurements recorded within the first 15 minutes from water-intake be considered in the AI sample for the calculation of t_{stat}, as well as for hypothesis testing with Student t-test and Wilcoxon Rank Sum. Based on gastric emptying and intestinal absorption rates found in literature [25], [35], [36], [37], [38], it was estimated that the amount of water present in the GI tract might already be half the quantity ingested after less than half an hour. Moreover, these rates are known to have an inter-personal variability of 22% to 30% [39], meaning the absorption might be even faster for some participants. By considering only those AI measurements recorded within 15 minutes after intake, we are relatively confident that the amount of liquid present in the GI tract is comparable to the total intake amount.

Summarizing: in order to select most promising features from the feature set, the t_{stat} value and the binary decision results from Student t-test and Wilcoxon Rank Sum are considered. These performance measures are obtained, for each of the 15 participants, of each of the 18 features applied to each of the 12 signal channels.
Subsequently, the number of participants showing a significant decrease in feature value from BL to AI, according to both tests, is averaged across all signal channels in order to observe the overall performance for each feature. The same is done for mean t_{stat} per participant.

Figure 25, Figure 26 and Figure 27 show the results for the data set from Test Round 1, lying position. As clear from the graphs, results from Student t-test and Wilcoxon Rank Sum are almost identical, and indicate the same trend of performance among different features. Moreover, it stands out how performance of the σ-based feature set (Features 1 through 9) and of the MAD-based feature set (Feature 10 through 18) is almost identical. This suggests that the presence, or effect, of outliers on feature calculation be minimal.
By observing the graph in Figure 27, we can gain insight on the average magnitude of effect observed by each feature. The t_{stat} value trend among features reflects results of the two statistical tests. In the figure, two magenta dashed lines indicate the positive and negative values of t_{stat} for which the result is deemed statistically significant for the chosen α level and sample size. Therefore, even though we see some negative values, these are not, on average, significant. From these three plots, it appears that the most promising features are Feature 4, and the respective MAD-based Feature 13. These show the highest *sensitivity*, which we define as the ratio of study volunteers for which the presence of water accumulation is 'detected' by the feature on the total number of participants. The effect magnitude (quantified by t_{stat}) is overall larger for the σ-based features, and Feature 3 in this case attains highest performance. These considerations point out to Feature 4, consisting in σ of the 'resonance band', and Feature 3, the one obtained from exclusion of respiratory and heart rate components, as the most promising candidates to proceed with feature optimization, in the case of lying position, and for the signal acquisition locations of Test Round 1. The selection of the most appropriate signal channel for acquisition is left as a later step.

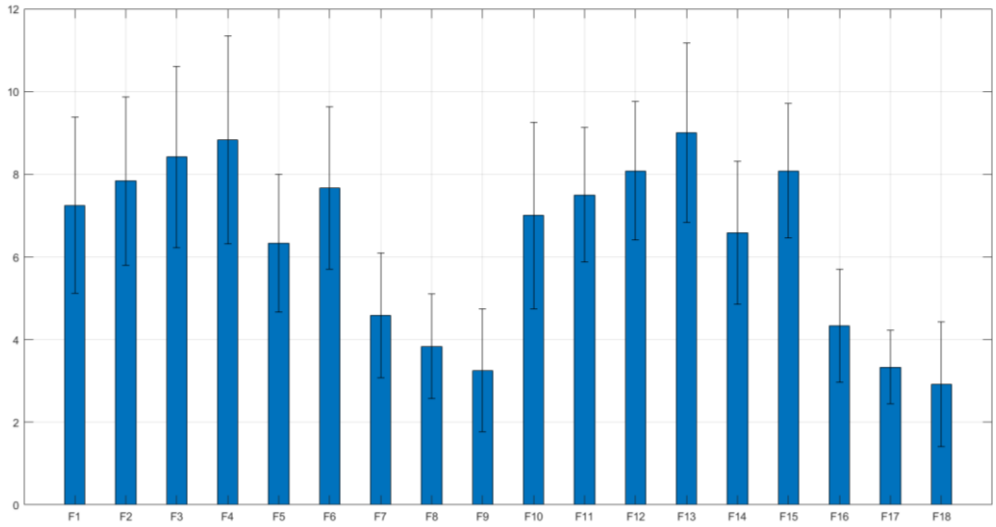

Figure 25: For each feature, number of participants, averaged amongst the 12 signals, showing a significant decrease in feature value from BL to AI according to Student t-test calculated on Test Round 1, lying data. The black vertical lines indicate standard deviation from the average.

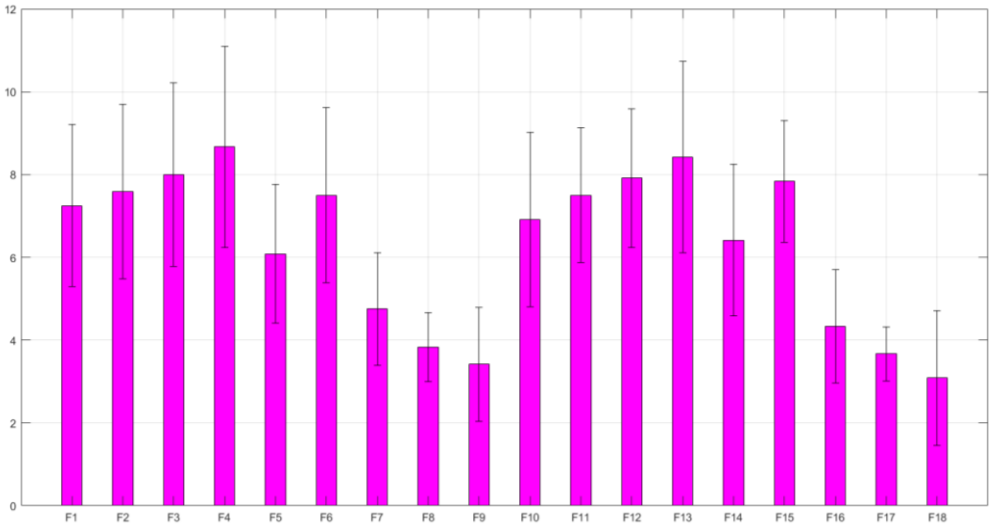

Figure 26: For each feature, number of participants, averaged amongst the 12 signals, showing a significant decrease in feature value from BL to AI according to Wilcoxon Rank Sum test calculated on Test Round 1, lying data. The black vertical lines indicate standard deviation from the average.

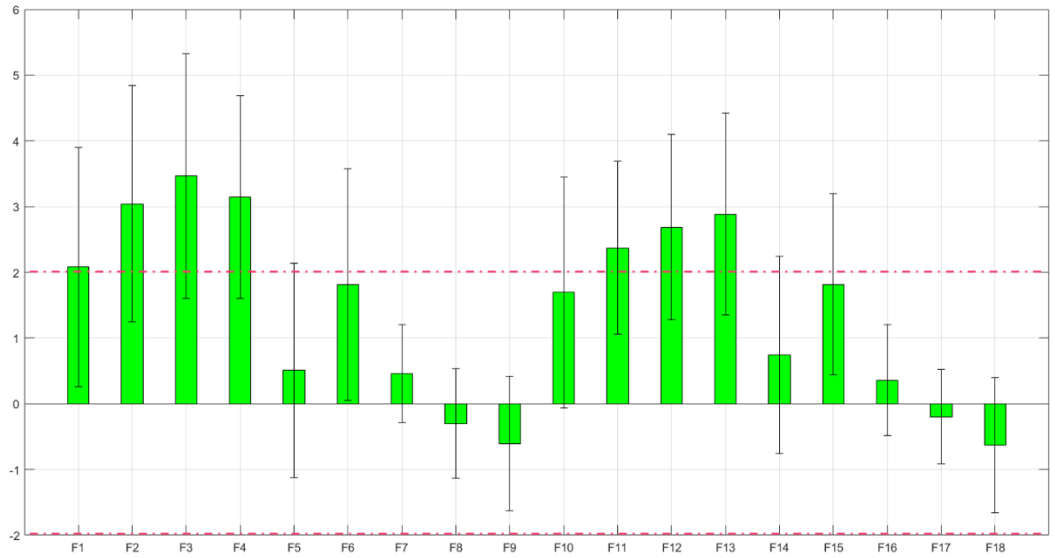

Figure 27: For each feature, mean t_{stat} value per participant, averaged amongst the 12 signals, calculated on Test Round 1, lying data. The black vertical lines indicate standard deviation from the average. The dashed lines indicates the t_{stat} value for which a result is deemed statistically significant at the chosen α value (in both directions) for the sample size considered.

We now proceed with the same analysis for the other two data sets, the standing data set of Test Round 1, and the lying data set of Test Round 2. Figure 28 and Figure 29 show results for the standing data (Wilcoxon Rank Sum results are not reported here because highly analogous to the Student t-test). In this case, the most promising feature appears to be Feature 3 (and the corresponding MAD-based version, Feature 12).

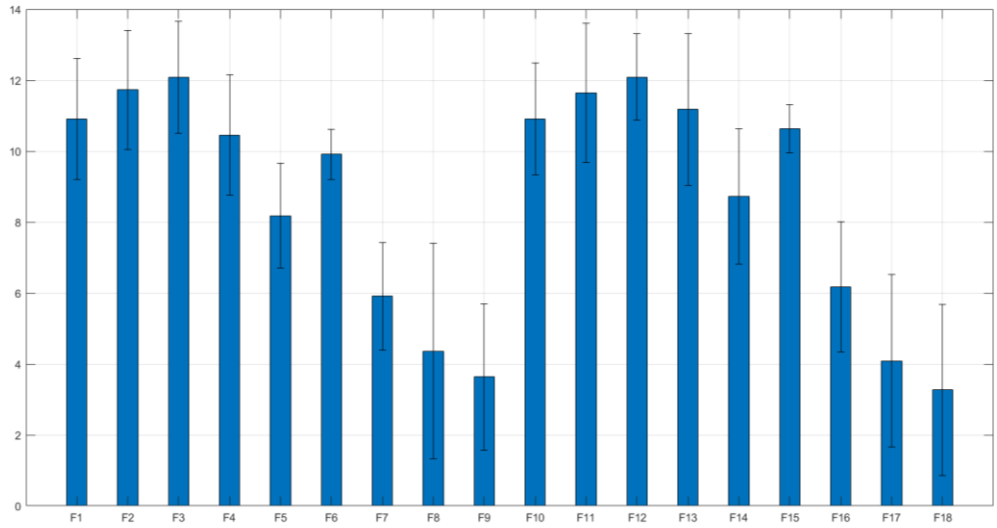

Figure 28: For each feature, number of participants, averaged amongst the 12 signals, showing a significant decrease in feature value from BL to AI according to Student t-test calculated on Test Round 1, standing data. The black vertical lines indicate standard deviation from the average.

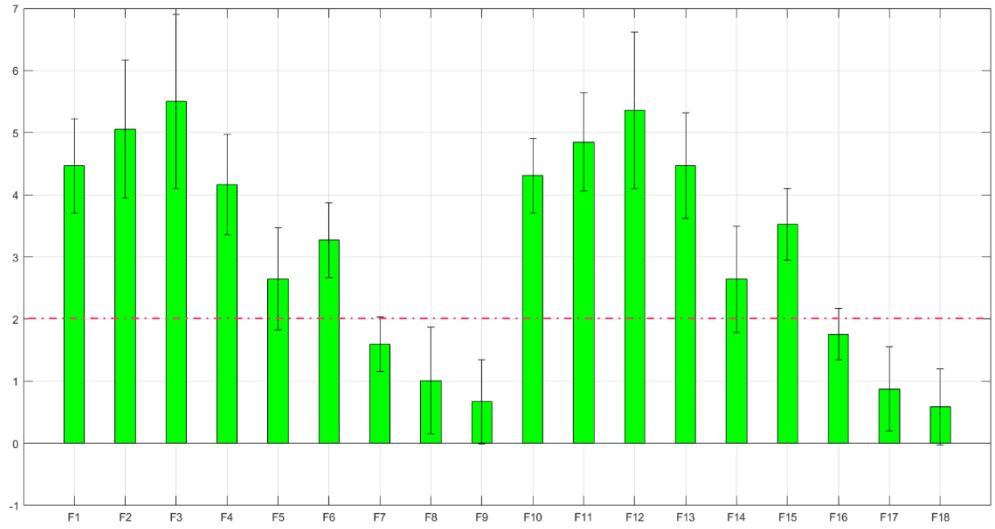

Figure 29: For each feature, mean t_{stat} value per participant, averaged amongst the 12 signals, calculated on Test Round 1, standing data. The black vertical lines indicate standard deviation from the average. The dashed line indicates the t_{stat} value for which a result is deemed statistically significant at the chosen α value for the sample size considered.

Finally, Figure 30 and Figure 31 show the results for the data set of Test Round 2, lying position. This time, σ-based features appear to perform overall slightly better than the corresponding MAD-based ones. Among the σ-based set, Feature 3 has a slightly better performance.

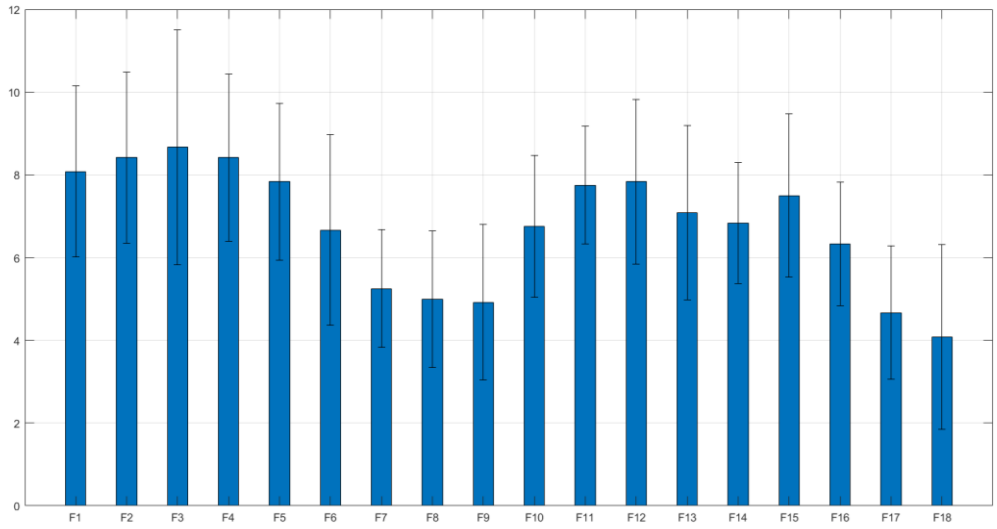

Figure 30: For each feature, number of participants, averaged amongst the 12 signals, showing a significant decrease in feature value from BL to AI according to Student t-test calculated on Test Round 2, lying data. The black vertical lines indicate standard deviation from the average.

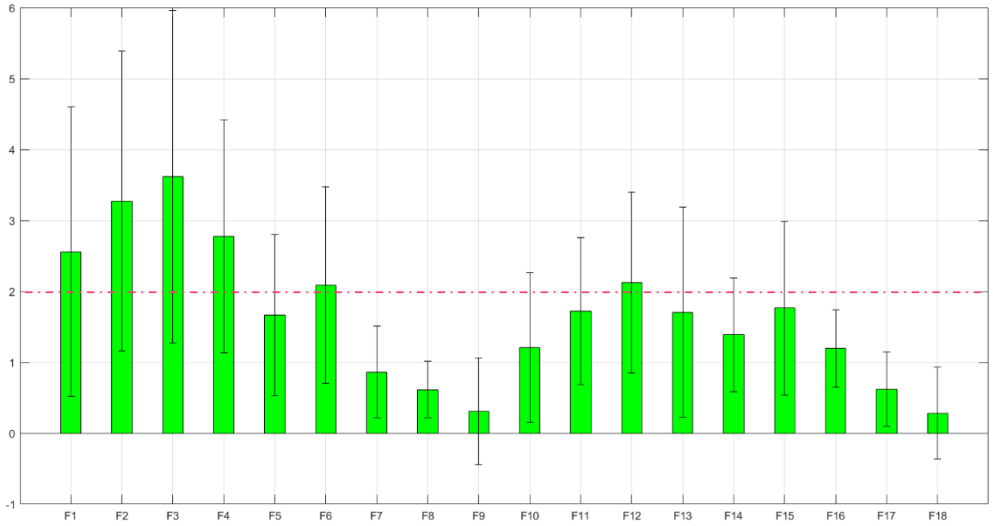

Figure 31: For each feature, mean t_{stat} value per participant, averaged amongst the 12 signals, calculated on Test Round 2, lying data. The black vertical lines indicate standard deviation from the average. The dashed line indicates the t_{stat} value for which a result is deemed statistically significant at the chosen α value for the sample size considered.

In conclusion, there are two features that overall stand out from the complete set of explored features. These are Feature 3 (especially in the standing data set and for the lying data set in Test Round 2) and Feature 4 (for the lying data set in Test Round 1). Both these features are based on the standard deviation-based measure of signal energy, and exclude the lower frequencies of the signal (using cutoffs at 2 Hz and 2.5 Hz respectively). There is thus quite a large overlap in the two features. However, the first considers all remaining frequencies up until 25 Hz, while the second limits the considered band to 7.5 Hz. The present study was conducted in particularly controlled and noise-free conditions; however, because in most real life scenarios this will not be the case, it is maybe advisable to obtain a finalized feature that uses a defined frequency band. The fact that Feature 3 in some cases performs better than Feature 4, suggests that the optimal upper cutoff frequency might be higher than that defined for Feature 4. Since the bands of these features were somewhat arbitrarily chosen, the next step will consist in a systematic analysis to define the optimal frequency band to use. Contextually, the optimal signal channel to use in combination with the finalized feature will be determined. Finally, a similar systematic analysis will determine the optimal window length and overlap percentage to adopt in calculating the features.

One last thing to check before going into feature optimization is whether there is any dependency of the chosen feature values with the instantaneous heart rate. As seen from Equation 8 in Chapter 4, the amplitude of response oscillation does not only depend on the damping coefficient, but also on the frequency of the forcing oscillation. Moreover, the forces and dynamics involved in pumping of blood during the cardiac cycle, which highly affect the BCG signal, could vary with varying heart rate. We thus need to make sure that the observed decrease in the recorded BCG signal energy is not due to a systematic change in heart rate between the two conditions. In order to exclude this possibility, the instantaneous feature values for each BL and AI measurement were plotted in relation to the corresponding instantaneous heart rate calculated over the same window. By visual inspection of these plots, it was possible to conclude that the effect observed is indeed not due to systematic heart rate variation. For instance, Figure 32 shows

the behavior of Feature 4 in one participant who had a very stable heart rate throughout the test (which was in fact the case for the majority of participants): we can clearly see a significant drop in feature value from the BL to the AI measurements, while the heart rate remains constant. Because the heart rate of participants during the experimental study conducted was in general very stable, we cannot completely exclude that stronger heart rate variations would affect the observed feature value. Nevertheless, we can at least be confident that the effect observed during the present experiments is indeed caused by fluid accumulation and not by a systematic shift in heart rate.

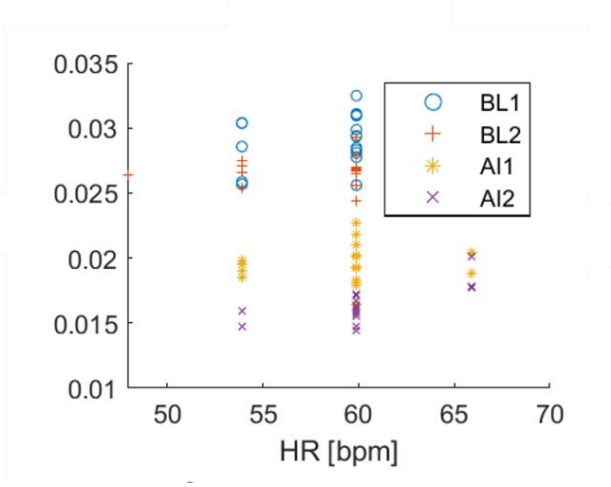

Figure 32: Scatter plot of instantaneous feature values, calculated from two BL and two AI measurements, against the corresponding instantaneous heart rate values

6.7 Feature Optimization

In order to optimize the working frequency band, a set of bands to test is generated as follows: lower cutoff frequencies are considered from 0.5 to 5 Hz in increments of 0.5; starting from each of these, 10 different bands are defined considering bandwidths of 1 to 10 Hz. Each of these bands is used to filter the input signals with a 6^{th}-order Butterworth band-pass filter, before calculation of the standard deviation using 10 seconds windows with no overlap. The obtained features are then analyzed based on the previously defined performance parameters: sensitivity, defined as the ratio of study volunteers for which the presence of water accumulation is 'detected' by the feature on the total number of participants, and effect magnitude, quantified by t_{stat}.

In Figure 33 and Figure 34, the sensitivity of each signal channel per frequency band is plotted for the lying data in Test Rounds 1 and 2 respectively. On the x-axis we have all the frequency bands used to filter the signal prior to calculation of the σ-based feature. The y-axis indicates the number of participants for which the corresponding feature shows a significant decrease in presence of water accumulation. Each of the 12 signals is plotted with a different marker, according to the legend to the right of the figure. For reference, the signals analyzed are schematized in Figure 35.

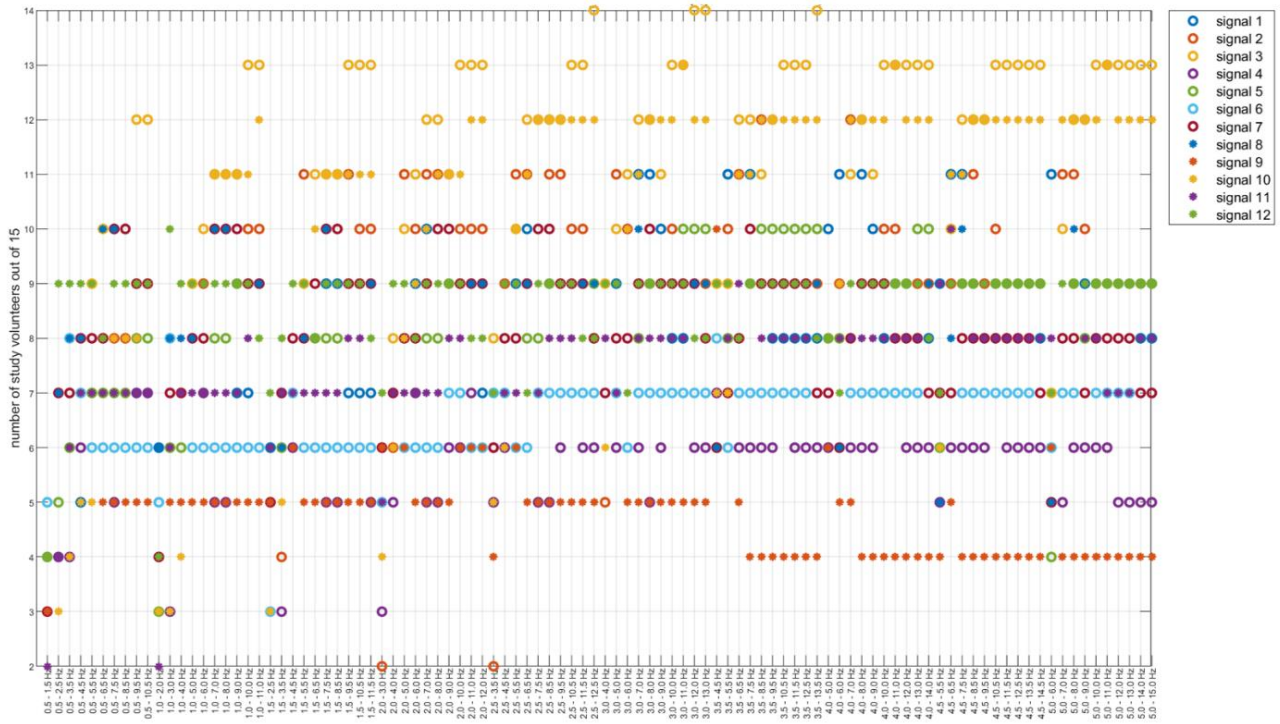

Figure 33: Sensitivity of σ-based features calculated on incremental set of frequency bands for each signal considered, for data set of Test Round 1, lying position.

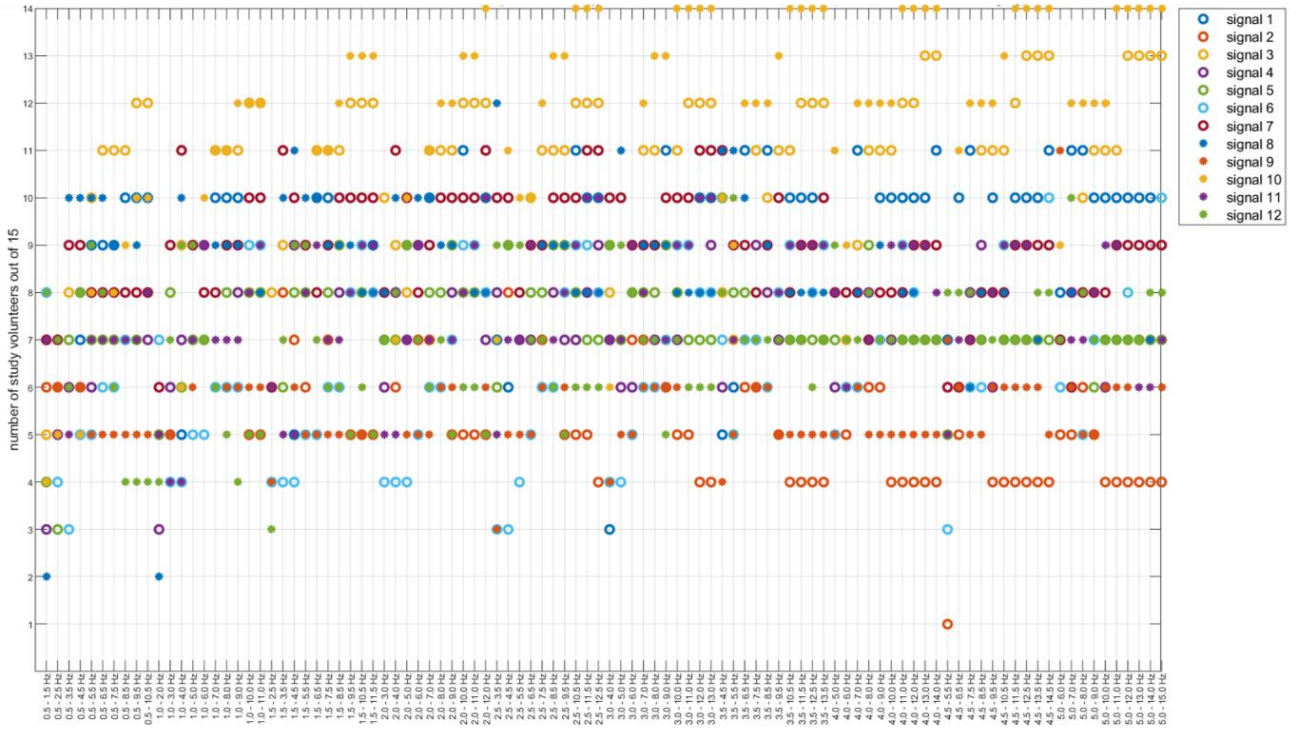

Figure 34: Sensitivity of σ-based features calculated on incremental set of frequency bands for each signal considered, for data set of Test Round 2, lying position.

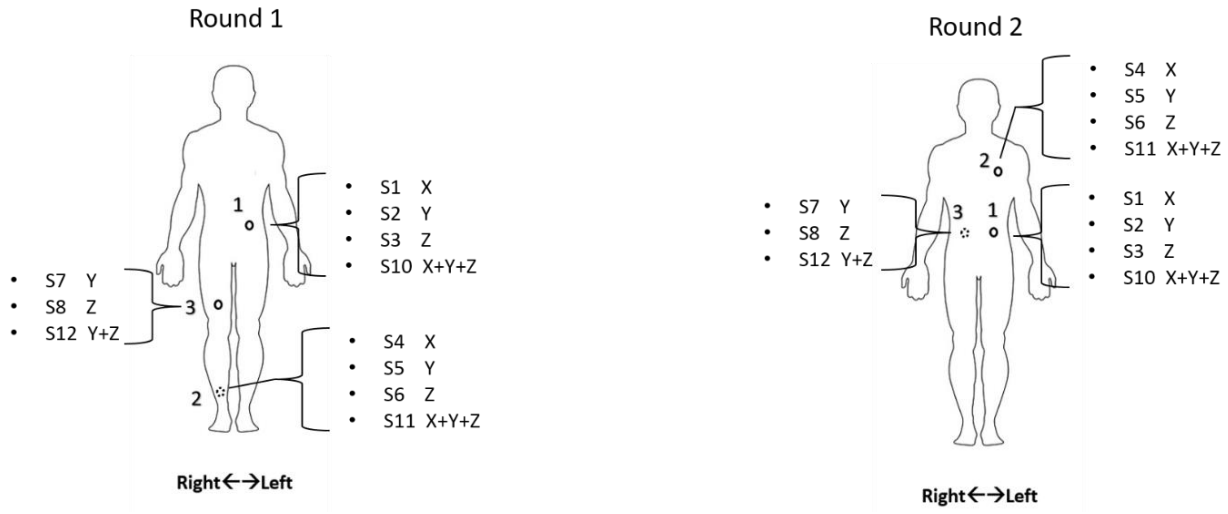

Figure 35: Schematization and nomenclature of the accelerometer signal channels analyzed

The first thing that stands out from these plots is that in both test rounds, the two signals that achieve highest sensitivity are Signal 3 and Signal 10. These correspond, respectively, to the Z axis and to the sum of all axes of the accelerometer located on the lower abdomen. We can therefore focus on these two signals for further analysis. This is somewhat fortunate, because it means we can compare the performance of each frequency band across two successive Test Rounds, and get an idea of the repeatability of the obtained results. In order to select the optimal frequency band and signal, the sensitivity and average mean t_{stat} achieved by each frequency band for both signals are obtained and compared. Eventually, it is found that the best performing signal overall is Signal 10, as it achieves higher overall sensitivity if results from Test Round 1 and 2 are averaged. Three candidate features achieved the highest (identical) performance when used on Signal 10. These are: 3 to 11 Hz, 4 to 11 Hz and 5 to 11 Hz. They show a sensitivity of 13 out of 15, and a mean t_{stat} of 6.7 in Test Round 1, and sensitivity of 14 out of 15 and mean t_{stat} of 7.5 in Test Round 2. The performance, averaged between the two Test Rounds, of these bands is summarized in Table 3.

Table 3: Overall performance (averaged between Test Rounds 1 and 2) of the optimal σ-based feature bands for lying condition, calculated on Signal 10.

Band [Hz]	Sensitivity (%)	mean t_{stat}
3-11	90	7.1
4-11	90	7.1
5-11	90	7.1

The same procedure is applied to the standing data set. This time, the best performing signal is Signal 1, as can be seen from Figure 36. Several signal bands reach a sensitivity value as high as 100%. By also comparing the mean t_{stat} value, again three bands with almost identical performance are identified as optimal. These are summarized in Table 4. It appears from these values that, overall, monitoring in the standing position achieves higher performance compared to lying. This might be attributed to two different factors: on one hand, the larger movement freedom in x and z directions compared to lying position, due to absence of full-body contact with the bed; on the other hand, the different spatial distribution of the liquid mass in the two different positions, likely having a stronger damping effect with the subject in a vertical position.

Table 4: Overall performance of the optimal σ-based feature bands for standing condition, calculated on Signal 1

Band [Hz]	Sensitivity (%)	mean t_{stat}
5-11	100	7.6
5-12	100	7.7
5-13	100	7.7

Because the feature obtained from using the band 5-11 Hz performs optimally for both standing and lying position, it is eventually chosen as working feature, so to obtain position independence.

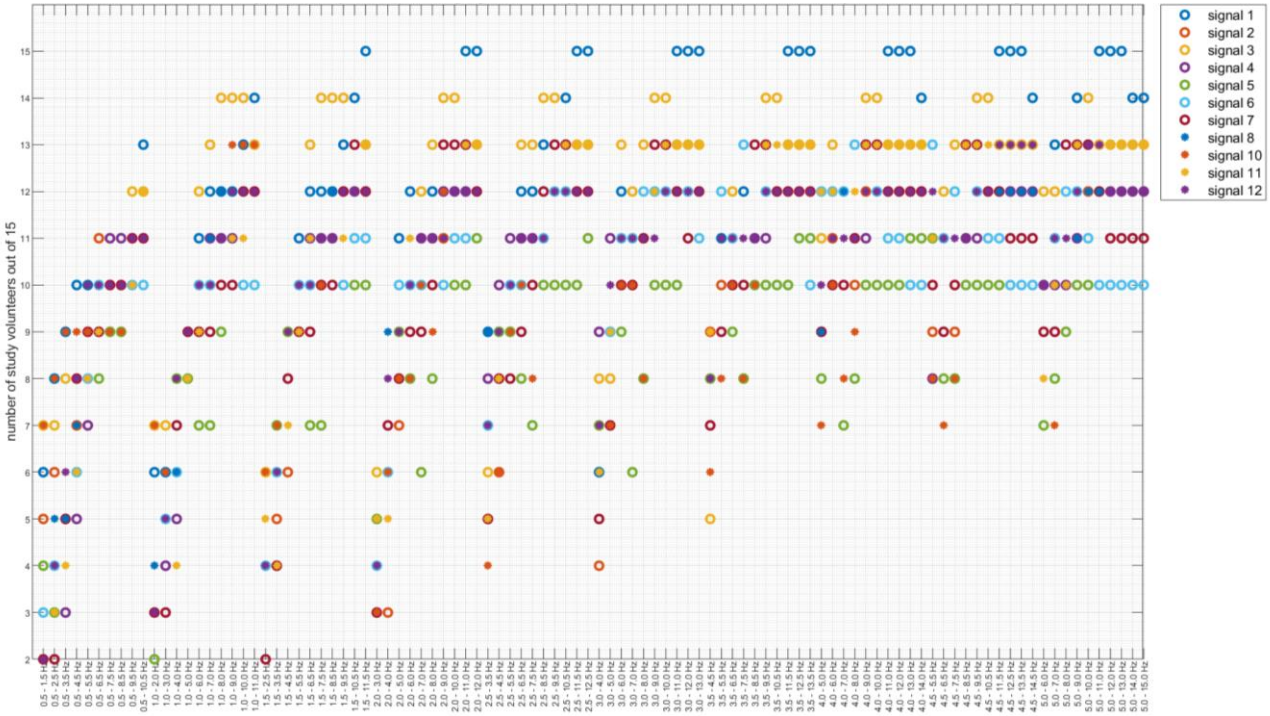

Figure 36: Sensitivity of σ-based features calculated on incremental set of frequency bands for each signal considered, for data set of Test Round 1, standing position.

The last optimization step consists in finding an optimal window length and overlap percentage for feature calculation. A similar procedure is adopted. Window lengths from 5 to 30 seconds are tested, each with 0%, 25%, 50% and 75% overlap. The performance is evaluated according to the same parameters. The highest performance is achieved by taking 5 seconds windows with 75% overlap. This is the combination which allows taking the largest number of data points per measurement, while also decreasing sample variance. This ultimately means obtaining a more accurate feature value per each condition, which is why the mean difference between BL and AI becomes more easily observable, as it is less 'polluted' by sample variance. It is therefore the right design choice albeit a slightly higher computational cost.

The performance of each of the defined combinations of window length and overlap level can be visualized in Figure 37. The x-axis reports each of the window length-shift length combinations used for calculation of the previously selected σ-based feature. On the y-axis, the corresponding performance values are reported: the red circular markers indicate the sensitivity (as previously defined), and the blue asterisk markers indicate the mean t_{stat} value per participant achieved by the corresponding feature. The plot in

Figure 37 was obtained from Signal 10 of the lying measurements during Test Round 2; however, the trend observed and related conclusions are completely analogous for all other cases as well.

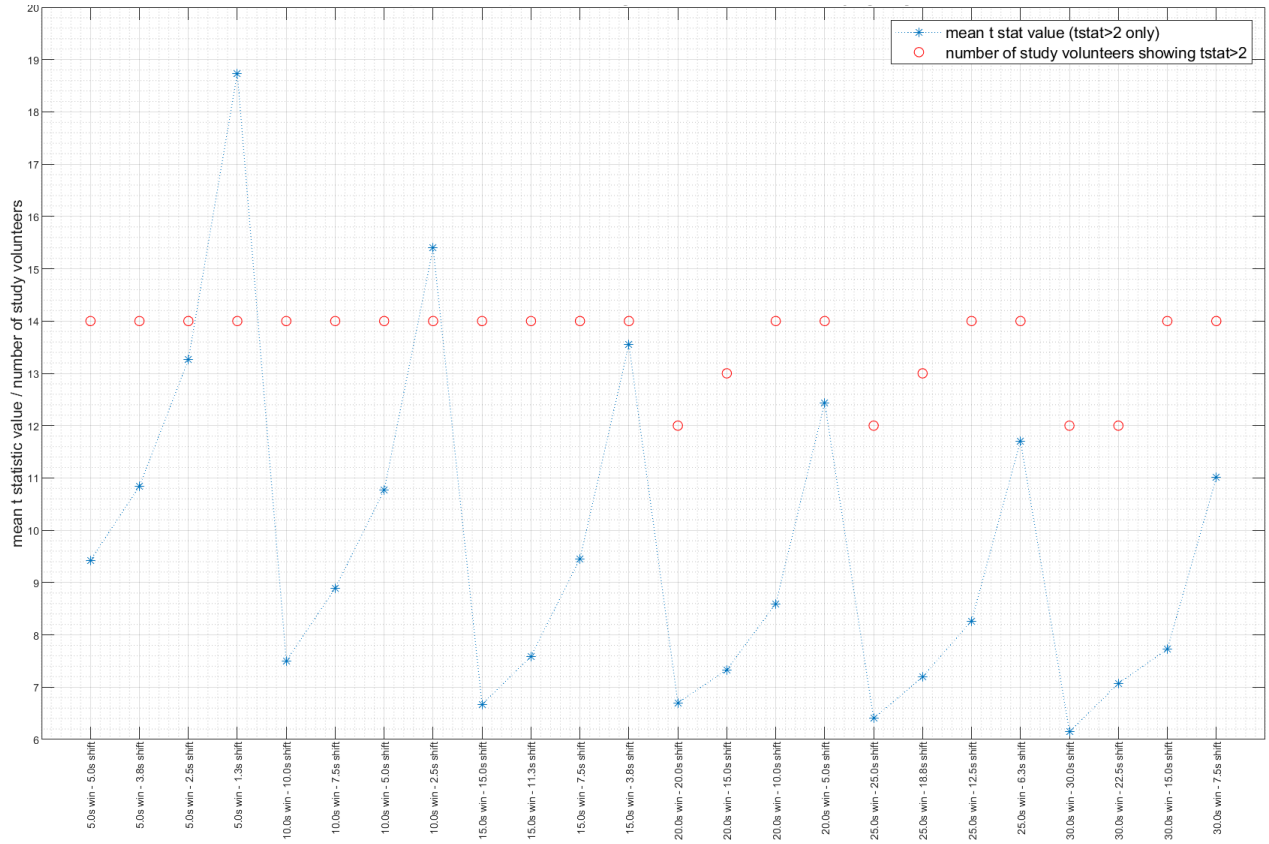

Figure 37: Feature performance using different window length and overlap percentage combinations, in terms of sensitivity and mean t_{stat} per participant (taking into account only the significant values).

7. Results

Two of the research objectives of the present study consisted in (1) developing a feature able to accurately capture the decrease in BCG signal energy caused by the presence of fluid accumulation in the body, and (2) determining the optimal sensing modality and sensing location on the body, among the ones tested, for monitoring of intra-abdominal fluid accumulation.

Based on the feature exploration, selection and optimization performed, an optimal energy-describing feature has been developed. This consists in the standard deviation of the input signal, computed in shifting windows of 5 seconds and 75% overlap, after pre-processing by movement artifact rejection (as described in Section 6.3) and band-pass filtering of the input signal with a 6-th order Butterworth filter with lower cutoff at 5 Hz and higher cutoff at 11 Hz.

Accelerometers appear to be the optimal sensor type, amongst the ones tested, for the purposes of this study. In particular, signals acquired from the accelerometer placed the left side of the lower abdomen (about 3 cm below the navel level), appear to capture the decrease in BCG signal energy due to intra-abdominal liquid accumulation with the highest sensitivity and effect magnitude, consistently for both lying and standing monitoring posture, and in both Test Rounds. The lower abdomen is, therefore, indicated as the optimal monitoring body location, among the set of locations tested in the present study, in the case of fluid accumulation in the abdominal cavities. However, while for monitoring in the lying position it was found that the highest performing signal is the one obtained from the sum of the three axes sensed by the accelerometer, for monitoring in the standing position a significant increase in performance was achieved by using the X component only as input signal for feature calculation.

Figure 38 schematized the steps involved in the optimized process of feature extraction.

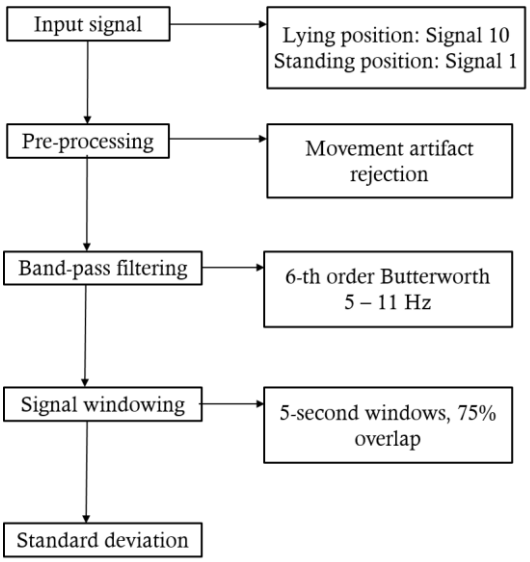

Figure 38: Schematization of optimized signal processing steps involved in energy feature extraction (for reference on signal nomenclature, see Figure 35).

Performance of the finalized feature, extracted from the respective chosen signals for lying and standing, is summarized in Table 5 and Table 6 in terms of sensitivity – as previously defined – and mean t_{stat} value.

Table 5: Performance of optimized energy feature (applied to Signal 10) in lying tests

	Sensitivity (%) based on Student t-test	Sensitivity (%) based on Wilcoxon Rank Sum test	mean t_{stat}	mean t_{stat} (only t_{stat}≥2 included)
Test Round 1	87	87	14.06	17.09
Test Round 2	93	93	16.38	18.72
Average	90	90	15.22	17.91

Table 6: Performance of optimized energy feature (applied to Signal 1) in standing test

	Sensitivity (%) based on Student t-test	Sensitivity (%) based on Wilcoxon Rank Sum test	mean t_{stat}	mean t_{stat} (only t_{stat}≥2 included)
Test Round 1	100	100	19.06	19.06

Because in any clinical scenario, a patient being monitored for pathological fluid accumulation, would be lying on a hospital bed, performances achieved during the lying tests give a more reliable indication for feasibility considerations of the proposed monitoring solution.
One could decide, for reasons of practicality, to trade the high performance of Signal 1 in the standing position, for a unified solution with good performance in both standing and lying positions. Signal 10 would be the best candidate for such a unified solution, as the sensitivity reported in the standing test is consistent with the value obtained in the lying position during the same test round. Its performance metrics in the standing test are reported in Table 7.

Table 7: Performance of optimized energy feature, this time applied to Signal 10, in standing test

	Sensitivity (%) based on Student t-test	Sensitivity (%) based on Wilcoxon Rank Sum test	mean t_{stat}	mean t_{stat} (only t_{stat}≥2 included)
Test Round 1	87	87	18.03	21.62

However, because of the higher performance achieved by Signal 1 in standing, in the present report it is chosen to indicate the latter as optimal choice for specific monitoring in the standing position.

The performance parameters used so far serve to give a statistical indication of whether there is an observable difference between the mean of the energy feature values obtained in BL and AI conditions. However, to have a more practical idea of the effect under analysis, it is useful to observe the feature values in the two conditions graphically represented as boxplots for each participant. Boxplots represent the distribution of groups of numerical data in terms of their median (represented as a red line), interquartile range (as a blue rectangle), distribution outside the quartiles (as a black vertical line delimited by horizontal dashes for the maximum and minimum) and outlier values (as red crosses). Figure 39 represents the energy

feature values (calculated on Signal 1) obtained from standing measurements during Test Round 1. Data points from BL and AI measurements are grouped in two separate boxplots, for comparison. Each plot corresponds to data from one of the 15 participants.

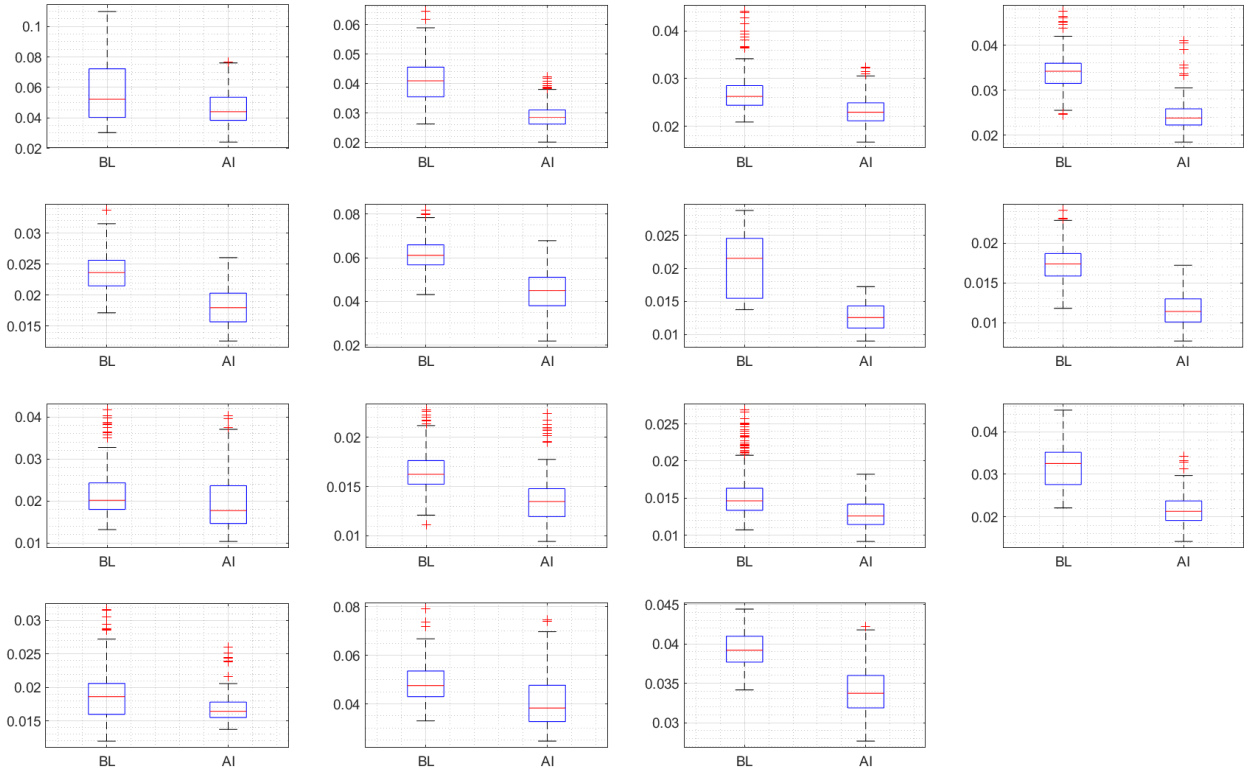

Figure 39: Boxplot representation of the energy feature values obtained from standing measurements of Test Round 1. BL and AI stand for baseline and after-intake condition, respectively.

As one can observe from the figure, a decrease in energy from BL to AI condition (drop in median level from first to second boxplot) is visible for all 15 participants, which is consistent with the results from Student's t-test and Wilcoxon Rank Sum test. However, the magnitude of median difference and level of overlap between the interquartile ranges varies among participants. Possible parameters affecting the magnitude of the effect observed per participant are explored in the Discussion chapter. Similar plots for the lying measurements of Test Round 1 and 2 are displayed in Figure 40 and Figure 41. It is interesting to observe that the participants for which there is no visible drop in energy are not the same in both Test Rounds (plots in second row, first column and third row, third column in Figure 40, and plot in first row, third column in Figure 41). Moreover, the same participants that do now show energy decrease in Test Round 1 lying, do appear to experience a visible drop in the standing data from the same test round. This suggests that these anomalies be contextual to some type of data contamination rather than to specific participant characteristics.

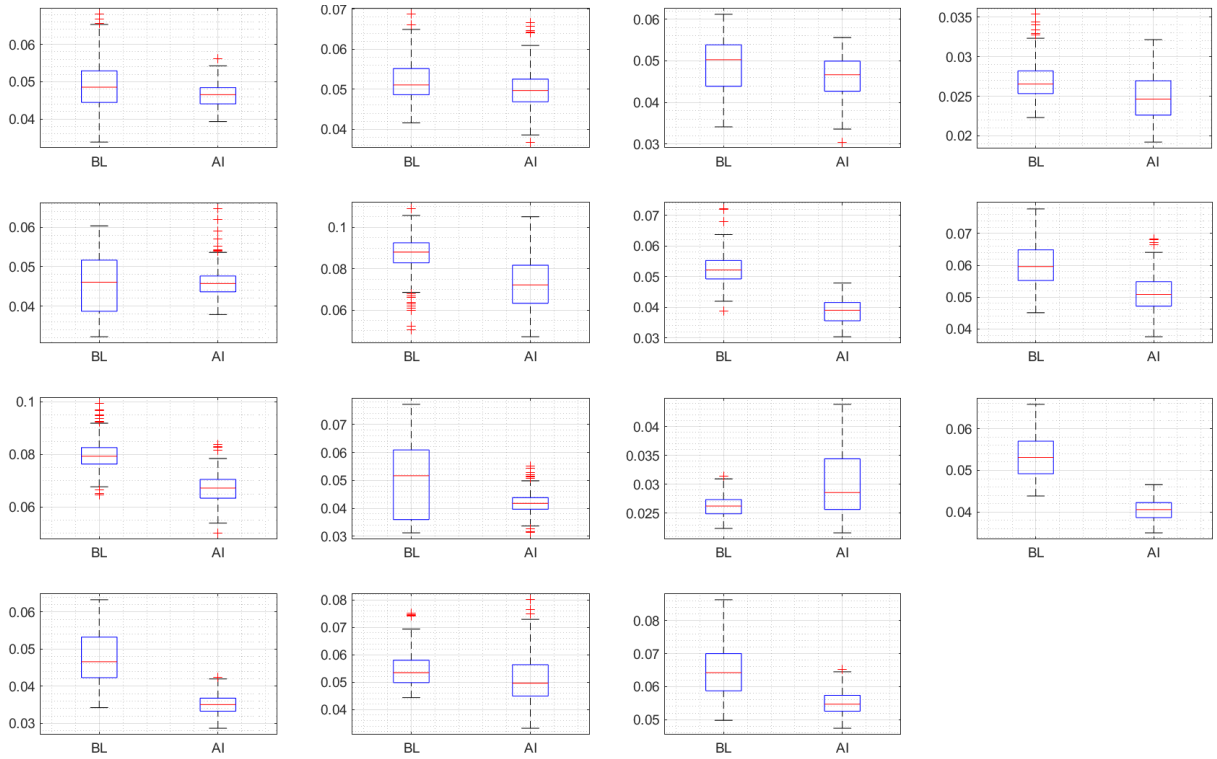

Figure 40: Boxplot representation of the energy feature values obtained from lying measurements of Test Round 1. BL and AI stand for baseline and after-intake condition, respectively.

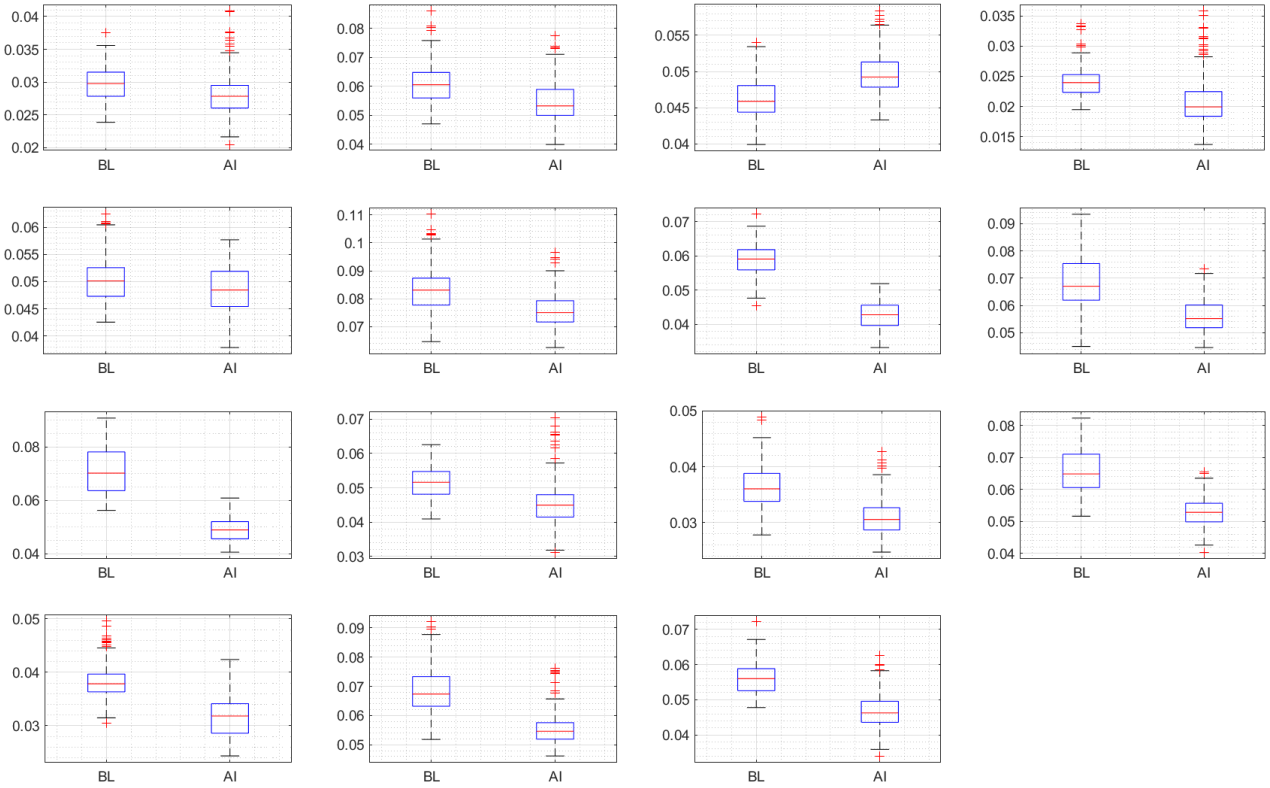

Figure 41: Boxplot representation of the energy feature values obtained from lying measurements of Test Round 2. BL and AI stand for baseline and after-intake condition, respectively.

The results reported in terms of performance metrics and graphical representation of the data consistently indicate the occurrence of the hypothesized decrease in BCG signal energy in presence of fluid accumulation in the body. However, when analyzing results from small scale experimental studies such as the one conducted for this research, it is common practice to verify the significance of the obtained results by means of a paired-sample Student's t-test. This is essentially the same test that had previously been used to assess the significance of the decrease in energy value observed between BL and AI samples from a same participant. However, this time we use it to verify whether the decrease in energy observed is significant over the set of all participants, given the sample size. This consists in testing the alternative hypothesis that the mean of the set of average BL values of all 15 participants is statistically different from, and higher than (since we use a right-tailed test), the mean of the corresponding set of average AI values. Because each value in the BL set has a corresponding value in the AI set to which it is mutually correlated (since they belong to the same participant), we must use the paired-sample version of the Student's t-test. Results of the t-test for the standing data (using Signal 1) and the two lying datasets (using Signal 10), are reported in Table 8.

Table 8: Results of paired-sample Student's t-test for the three experimental datasets

	Standing – Test Round 1	Lying – Test Round 1	Lying – Test Round 2
t-test *p*-value	0.000007	0.000257	0.000225

By looking at the test *p*-value, we can see that, for all three cases tested, the null hypothesis is rejected at a confidence level higher than 99.9% (p-value<0.001). This result strongly validates the hypothesis at the basis of the present research study.

8. Discussion

Results of the experimental study and analysis conducted confirm the presence of an observable and consistent decrease in BCG signal energy due to presence of internal fluid accumulation in the body, which can be effectively quantified by use of the indicated signals and feature extraction method. The positivity of results obtained suggest that this technique has indeed the potential to be further developed towards use as an unobtrusive monitoring tool for internal fluid accumulation. However, several challenges are envisioned on the basis of the results observed, and these will be addressed as discussion points in the present chapter.

8.1 Variability of the Effect Magnitude

The first discussion point regards the variability in effect magnitude observed in different participants. Whereas a decrease in the mean energy value is consistently observed from BL to AI, the amplitude of this decrease and the amount of sample overlap differs widely. This can be observed by representing the sample distribution in histograms, as done in Figure 42 for data from the lying Test Round 2.

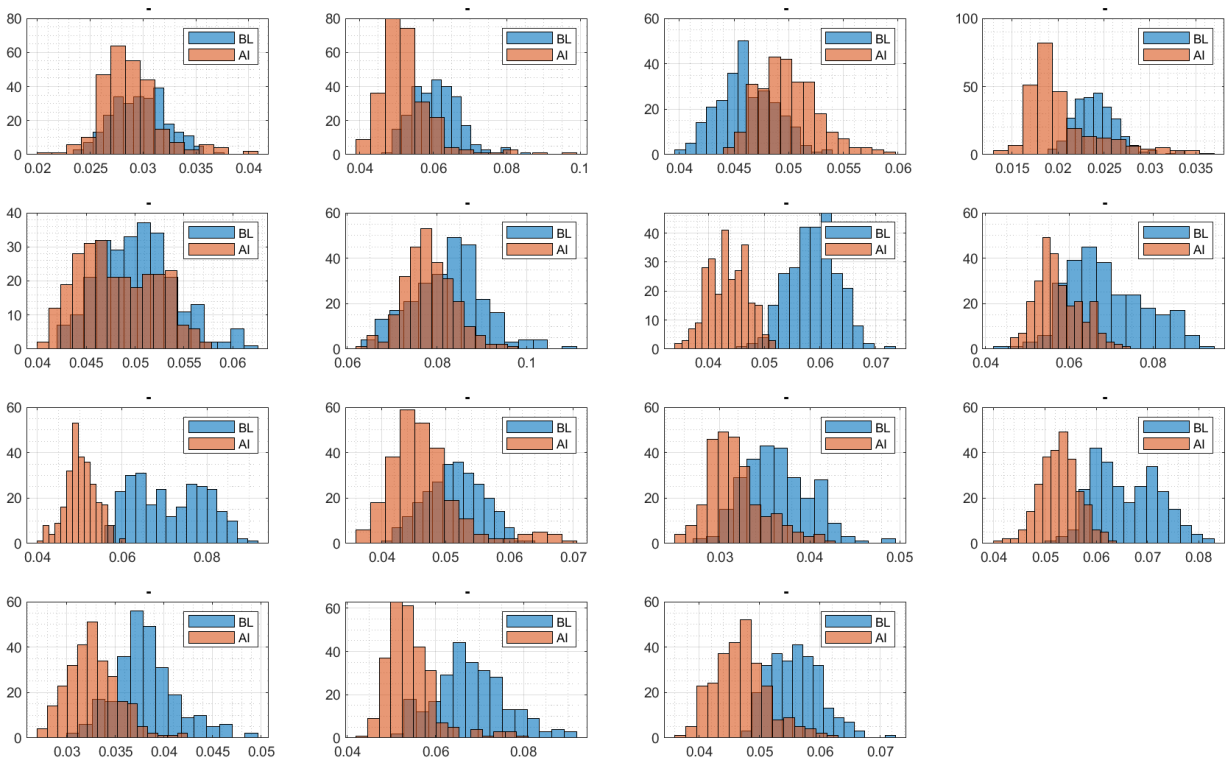

Figure 42: Sample distribution histograms of BL and AI values obtained for each of the 15 participants during the lying Test Round 2

These are several factors which might play a role in this interpersonal variability. A first consideration is that the amount of liquid ingested by participants during the experiment is fixed to 500 mL, whereas their

body weight varies considerably. It seems plausible to hypothesize that different ratios of ingested liquid mass to total body mass will be linked to different effect magnitudes. In particular, we expect that the higher this ratio, the higher the experienced dissipation of signal energy and vice versa. Similarly, this variability could be linked to anatomical differences and body mass composition parameters that affect the vibrating response of the body to the cardiac harmonic excitation and to presence of the damping element. Finally, characteristics of the BCG signal itself are extremely person-dependent [19] and vary according to several parameters such as ventricular ejection force, cardiac contractility, arterial blood pressure and cardiovascular health [15], [40]. We can imagine that for instance, a more irregular BCG pattern could contribute to masking results. Finally, as previously mentioned, a large inter-personal variability exists in water absorption rates [39]. This is likely a contributing factor to variability of the effect magnitude observed.

As per approved experimental protocol, the following personal data of the study participants were made available for analysis: weight, BMI, gender and age. Moreover, the average heart rate of each volunteer was extracted from the BCG signals acquired. It was therefore possible to derive simple linear regressions of the magnitude of the effect observed (measured as the t_{stat} value) to each of these variables. Figure 43 and Figure 44 show the linear regressions obtained for the results of lying Test Round 1 and 2 to these parameters. For the linear regression, data points showing a negative t_{stat} smaller or equal to -10 were excluded from the dataset. There was one such data point in each Test Round, belonging to two different participants. These values deviate highly from the range of the remaining dataset, and there is no correlation in the available personal parameters between the two subjects experiencing this result. Moreover, the anomalous behavior for both of these subjects is isolated to one Test Round and is not repeated in the standing test either. For these reasons, they are considered as outliers.

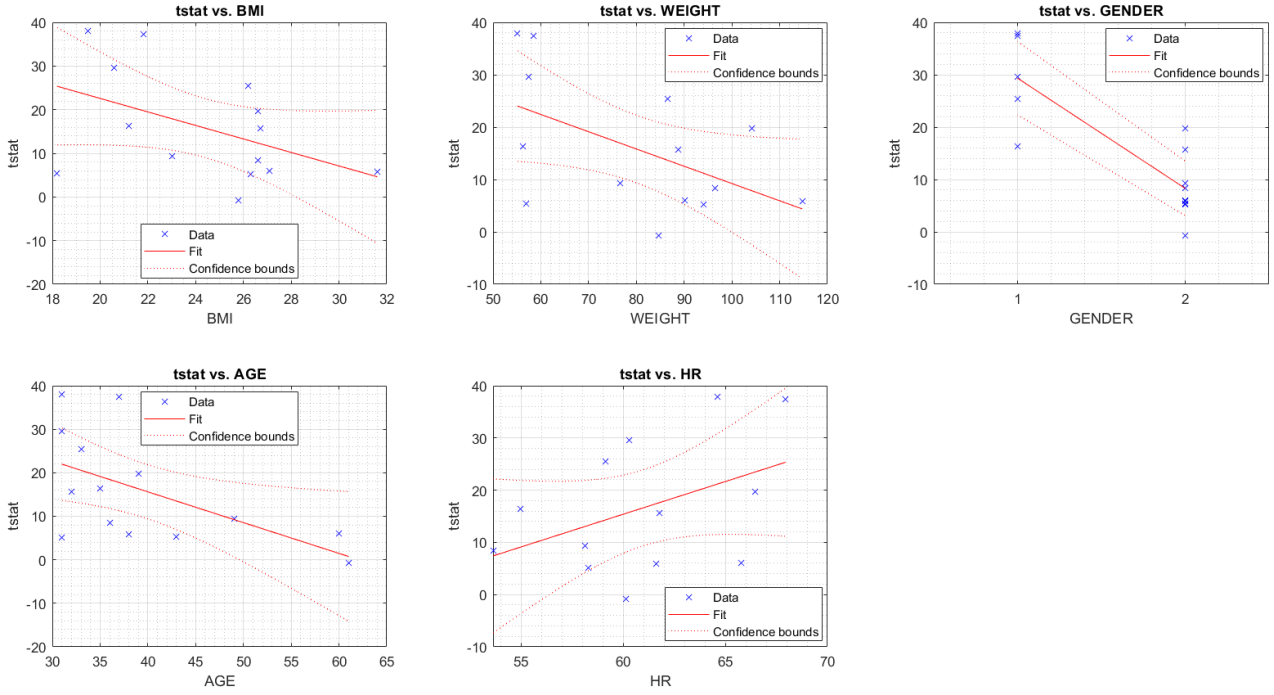

Figure 43: Linear regression of individual t_{stat} value from lying measurements of Test Round 1 to participant BMI, weight, gender, age and average heart rate.

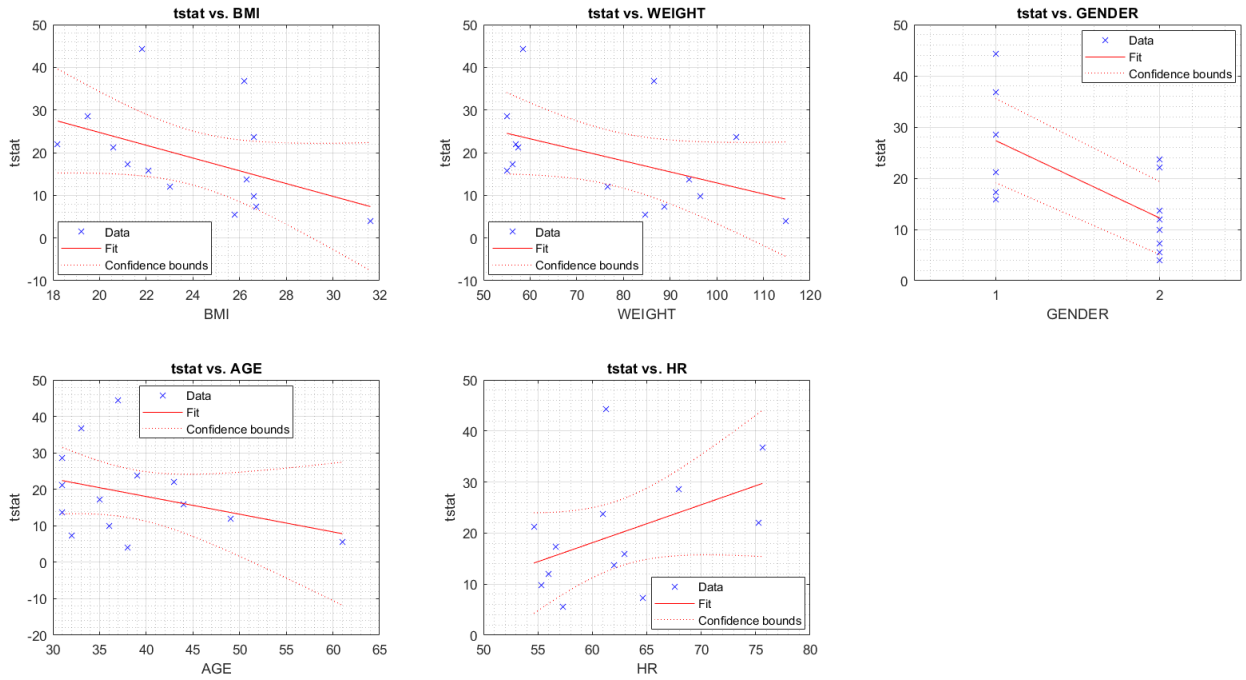

Figure 44: Linear regression of individual t_{stat} value from lying measurements of Test Round 2 to participant BMI, weight, gender, age and average heart rate.

Table 9: Regression coefficients and *p*-values for each independent variable for lying data of both Test Rounds

	BMI	Weight	Gender	Age	Heart Rate
c – Round 1	-1.5478	-0.32964	-21.033	-0.70706	1.2529
c – Round 2	-1.496	-0.25838	-15.095	-0.48504	0.74324
p-value – Round 1	0.0995	0.053	0.0002	0.032	0.143
p-value – Round 2	0.0937	0.101	0.0106	0.223	0.117

Table 9 reports the regression coefficients for each of the considered variables in the two Test Rounds, and the corresponding *p*-values. The *p*-values of each independent variable express the level of confidence at which the regression model rejects the null hypothesis that the variable has no correlation with the dependent variable. A high *p*-value indicates that there is insufficient evidence to conclude that the relationship expressed by the model exists at the population level. The regression coefficients express the direction and amount of change in the dependent variable in response to a unit increase of the independent variable. According to the *p*-values obtained, the only variable whose descriptive value is statistically significant at a 95% confidence level in both test rounds is gender. In the plot labels on the x axis of the gender graph, 1 stands for female and 2 for male, meaning that the effect magnitude observed is consistently higher in female participants compared to male ones. Men and women have very different anatomy, and this difference is known to extend even to the heart itself. More so, gender differences exist in cardiovascular physiology too [41]. It seems plausible, therefore, that such differences influence the BCG signal and, consequently, its response in presence of fluid accumulation. However, further research is required to understand the exact nature of these influencing factors. As for the other variables, even though the statistical significance is lower, we can observe some trend by looking at sign and value of the regression coefficient. For instance, the regression coefficient for BMI is negative, indicating that a higher BMI tends

to be linked with a decrease in effect magnitude, as previously hypothesized. The BMI measures the body mass divided by the squared body height. It thus gives a better indication of the amount of body mass concentrated on the abdominal area rather than weight itself, which might explain why BMI appears more strongly correlated to t_{stat} compared to weight. Overall, for the limited sample size available and, on the other side, large variance of the dependent variable, it is indeed difficult to draw definitive conclusions. However, further research, involving a larger number of participants, will likely give better insight on the dependency of the effect observed to any physiological parameter. In fact, because the individual t_{stat} tends to be relatively consistent within the two test rounds (remember that the two test rounds are repeated at approximately one week distance), we understand that some personal parameter must indeed play a role in the effect magnitude observed. This is clear from Figure 45, which reports the t_{stat} values obtained by each participant in the two test rounds. The two outlier values have been excluded from the plot for the reasons explained above. It is also interesting to notice that the majority of participants (9 out of 13) score a higher t_{stat} value in Test Round 2 (magenta dots). This might be related to the fact that Test Round 2 has been conducted in a more stable and noiseless fashion, since participants were lying on the bed continuously after water intake, without interleafing standing and lying measurements. This is a promising result, since the latter situation is clearly more similar to a clinical monitoring scenario.

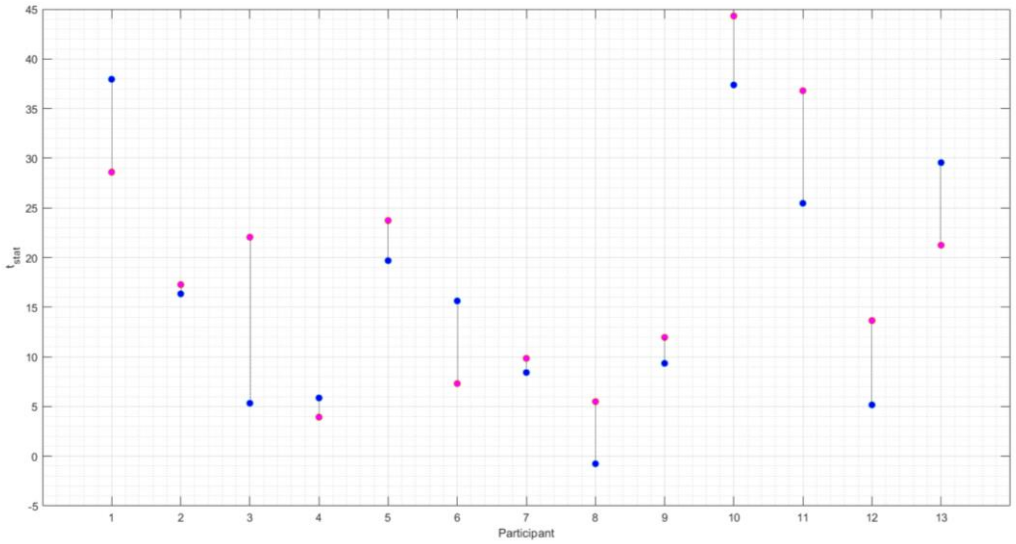

Figure 45: Difference in t_{stat} value of each participants between the two lying test rounds. Blue dots represent results of Test Round 1 and magenta dots of Test Round 2.

8.2 Inter-personal and Intra-personal Variability of the Baseline

Another challenge envisioned, in view of a future effort in developing a detection algorithm based on the suggested feature, lies in the baseline variability, and variability of the feature itself. What we have proven so far is that a decrease in feature value is, consistently, observed when monitoring a volunteer starting from a baseline condition and then inducing a fluid accumulation. This means that, in a hypothetical clinical scenario, this monitoring method would allow individuation of a transient increasing fluid

accumulation from some baseline condition (be it absence of fluid, or presence of an initial amount of fluid). The crucial point here is the necessity of a baseline measurement to be able to assess fluid accumulation. If, say, a patient would be subject to monitoring starting from an advanced stage of fluid accumulation, this method, at its present stage, wouldn't be able to assess this initial condition. Instead, it could only be able to detect whether there would be a further development from this initial condition. However, there are two points of investigation in this regards, which are possible thanks to the availability of the repeated lying test in the two test rounds. The first one is evaluating whether there is consistency over time in the individual BL and AI values obtained for a volunteer, so to get insight on the level of intra-personal variability of the feature. Figure 46 contains a plot for each volunteer, where the first boxplot represents the BL feature values of the first and second test round grouped together, and the second boxplot, analogously, the AI feature values of the first and second test round grouped together. The results observed are actually promising, because for most of the volunteers (12 out of 15), we can still observe a drop in the median line from the BL to the AI boxplot. This means that, in general, feature variability over a relative amount of time (one week circa) is not as large as to completely hinder separation of BL from AI condition. Additionally, Figure 47 shows how the individual mean BL values per participant are very consistent within the two test rounds. This observation is further confirmed by performing a paired-sample Student t-test on the two sets of mean BL values of Test Round 1 and 2: the test fails to reject the null hypothesis that there is no statistical difference between these two sets (p-value of 0.757). This implies that use of this feature would hypothetically allow, for instance, long-term monitoring of a patient once a 'healthy condition' baseline value has been stored for calibration. Of course, at this stage, it is not possible to make any claim on the usability of this method in a clinical situation, as many more variables might play a role when dealing with pathological scenarios. However, these results further testify the feasibility of this method, and prove that investment in further research is indeed worthwhile.

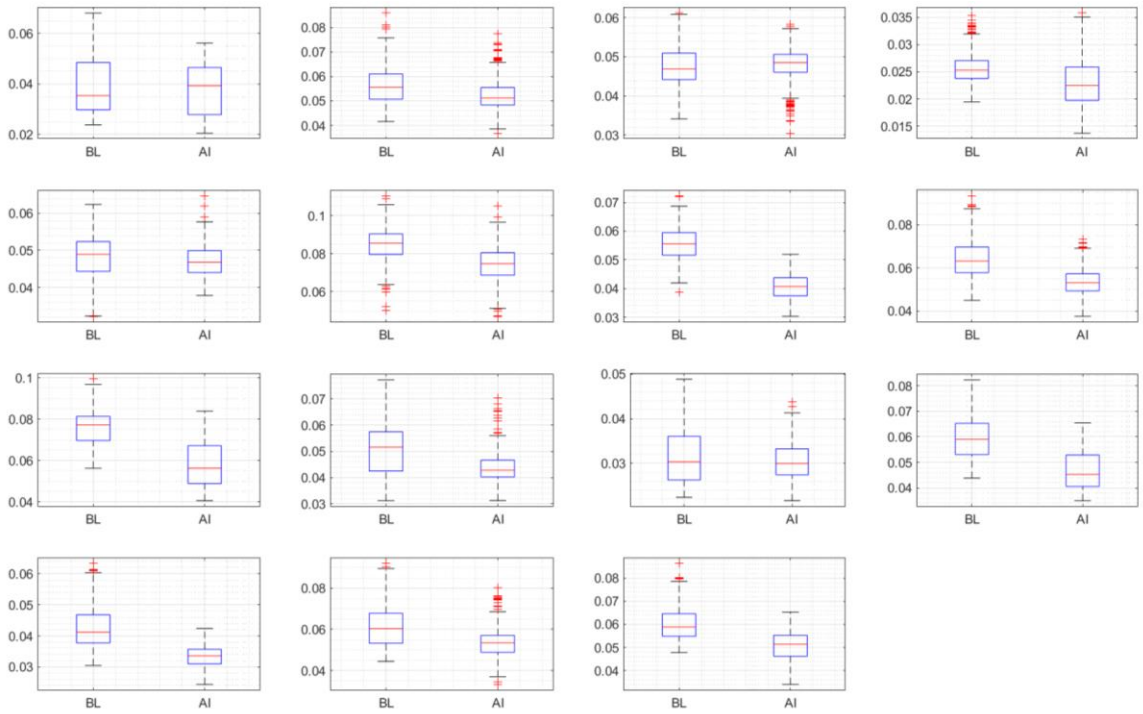

Figure 46: Boxplots obtained by grouping the BL and AI feature values of the two test rounds for the lying data.

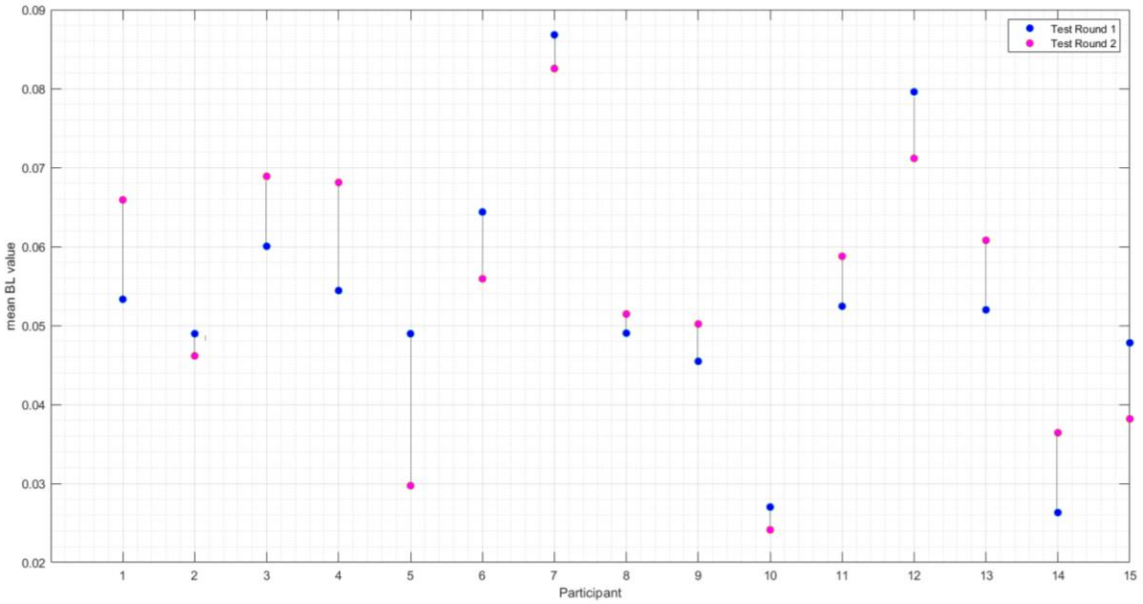

Figure 47: Mean BL values from the two lying test rounds for each participant.

The second point of investigation deals with the inter-personal variability of the feature. This entails checking whether it is still possible to discern BL condition from AI condition when grouping the feature value of all participants together. To verify this, we again plot the two conditions in separate boxplots, this time taking all data points from all participants together for each. The resulting plot is shown in Figure 48. As one can deduce from the figure, although there is indeed an overall visible decrease, on average, of the feature values from BL to AI condition, this decrease is too small in relation to the amount of overlap of the interquartile ranges. In practice, it would not be possible to measure the feature value of a person, without knowing a priori their baseline value, and assign the measured value to one of the two conditions, at least for the amount of liquid considered in the present study. This is, indeed, a limitation factor that, at the present stage, relegates this method to a personalized monitoring tool rather than a diagnostic tool.

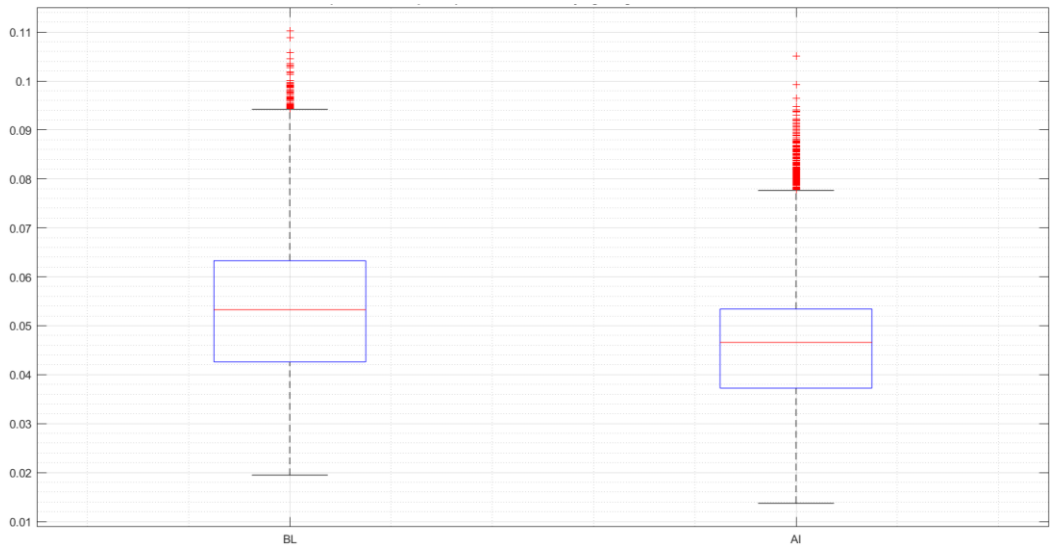

Figure 48: Boxplots of BL vs. AI feature values of all participants from both Test Rounds

One envisioned solution could exist if we would be able to predict, on the basis of personal physiological parameters, the expected BL value. We tried, therefore, to relate the mean BL value of each participant to the available personal data by means of a linear regression similarly to what was described in the previous section for the effect magnitude. However, none of the variables available appeared to have a significant predictive value for BL over the two test rounds. Nevertheless, from observation that the baseline value is consistent within participant, it is highly likely that its value be dependent on personal physiological parameters, and we must rely on further research to investigate what these are.

8.3 Feature Overfitting

The third discussion point deals with the risk of overfitting of the developed feature to the limited dataset available. In the feature optimization phase, an optimal spectral band has been selected for feature extraction based on two selection criteria: highest average sensitivity, and highest effect magnitude in the two lying test rounds as well as in the standing test. However, we must be aware that the high performance of this feature might be highly specific to the set of volunteers based on which the optimization has been performed. In other words, the fact that this feature works really well for the vast majority of participants included in this study does not necessarily mean that the same performance will translate to any set of subjects. This risk must be accounted for and is a common limitation to small-scale studies.

In order to be confident that the effect observed is not a result of chance, we can test whether, extending the bandwidth on which the feature is calculated to a wider band, the feature still achieves a similar performance and overall significance of results. In order to do this, a new feature was calculated, as previously using Signal 10 for the lying data and Signal 1 for the standing, however this time by band-pass filtering with cutoffs at 3 and 15 Hz. This band includes virtually any BCG frequency component, excluding respiratory and heart rate bands, and assuming that any signal power at frequencies above 15 Hz be mainly due to noise. If the high performance of the feature depends, as hypothesized, on the interaction of BCG signal frequencies with the body's natural frequencies, based on the values suggested in literature [30] we can be confident that this band should include any value of human body's resonant frequency. Most importantly, this band is chosen arbitrarily (based on field knowledge) and is not data-driven.

Table 10 summarizes the results obtained by using this generalized feature, in terms of sensitivity as previously defined, and on the results of the paired-sample Student's t-test used on the entire volunteers set. These results are almost identical to those obtained with the optimized feature and show significance at a confidence level above 99.9%. This gives us confidence that the effect observed is indeed real and that the feature is robust in terms of band used.

Table 10: Performance of generalized feature in terms of statistic values from a paired-sample Student's t-test and of sensitivity

	Standing – Test Round 1	Lying – Test Round 1	Lying – Test Round 2
t-test *p*-value	0.000016	0.000590	0.000144
Sensitivity (%)	100	87	93

9. Key Contributions and Future Developments

The presented research study has as primary goal the validation of a novel technique for unobtrusive monitoring of fluid accumulation in the body. This technique involves monitoring of the Ballistocardiogram, a signal resulting from the periodic oscillations generated on the body due to ballistic forces produced by the heart with the ejection of blood into the large vessels during each cardiac cycle. The hypothesis at the basis of this work is that, upon onset of an internal fluid accumulation within the human body, the energy of these oscillations will decrease as a result of added viscous damping caused by the fluid mass. The motivation behind pursuing such a monitoring technique is that, at present, screening methods for internal fluid accumulation are mainly imaging-based, thus limited to spot-checks and demanding operation by trained staff, and are only performed once the presence of a particular condition is already suspected from clinical evaluation of the patient. For instance, in the case of internal bleeding, screening is triggered by observation of hemorrhagic shock indicators such as abnormal heart rate and blood pressure. These, however, are often only apparent after loss of a considerable amount of blood (approximately 1 liter) has already occurred. The method proposed in this thesis would allow unobtrusive, continuous monitoring of internal fluid accumulation, and could be usefully incorporated within the clinical workflow as an early alert system.

The most significant contributions of this thesis work towards validation and development of this novel technique are the following:

- Generation of an *ad-hoc* dataset by means of an experimental study conducted on 15 human volunteers, comprising of BCG signals acquired before and after inducing intra-abdominal fluid accumulation via ingestion of 500 mL of water by the participants. The dataset is comprehensive of signals acquired with three different sensing modalities (tri-axial accelerometers, EMFi, load cells), in two different monitoring positions (lying and standing), and from several different sensing locations on the body.
- Determination of suitable preprocessing steps for preparation of the BCG signals for specific use in energy-quantifying feature extraction.
- Development of an optimal energy-describing feature able to quantify the energy decrease due to fluid accumulation consistently and with high sensitivity. This feature is based on the standard deviation of the signal, calculated on sliding windows of 5 seconds and 75% overlap, over a passband which contains the higher BCG frequencies (5 to 11 Hz). These are thought to experience an enhanced damping effect due to interaction with the body's natural frequencies. The feature so defined yielded promising results in terms of sensitivity (ranging from 87 to 100% in the different test rounds performed). Because the amount of fluid detected by the feature is at most 500 mL, ability of this technique to attain low detection limit is foreseen (the amount of fluid investigated is, for instance, 50-70% lower than the detection limit of standard practice for internal hemorrhage assessment based on hemorrhagic shock indicators).
- Selection of the optimal sensor type and monitoring location to use in the present context, among the ones tested. This was found to be tri-axial accelerometers. In particular, for monitoring in the lying position, the best signal to use, among those available, was found to be the sum of the three

axes components of an accelerometer placed on the left lower abdomen, approximately 3 cm below the navel height. For monitoring in the standing position, the same signal proved to perform similarly to the lying case, however an even higher performance was achieved by using the x signal only of the same accelerometer (still located on the lower abdomen), i.e. the axis perpendicular to the body's sagittal plane.

- Validation of the hypothesized effect via statistical significance analysis, with results supporting feasibility of the proposed technique. In particular, a paired-sample Student t-test shows a consistent decrease in signal energy (quantified by the above described feature), from baseline to after-intake conditions, at a confidence level of above 99.9% (p-value<0.001), for all test rounds performed.

Overall, the feasibility of such a monitoring technique is supported by results of the present study, and further research towards the improvement and development of this technique is considered worthwhile and highly encouraged. There are, of course, several aspects demanding further investigation. One deals with gaining deeper insight into the factors affecting the personal baseline value. The BCG signal characteristics are known to have high inter-personal variation, being affected by a variety of physiological and anatomical parameters. The same is true for the body's BCG-induced oscillations. In the present study, an attempt to correlate baseline values with participants' BMI, weight, age, gender and average heart rate yielded inconclusive results. However, it is likely that a larger-scale study, also involving additional parameters, might indeed succeed in this intent. It has, in fact, been observed that the baseline value for individual participants was highly consistent across the two test rounds, which were conducted at a week's distance, implying there must be a correlation to personal physiological parameters.

Another point which demands further investigation is the inter-personal variability in effect magnitude observed. Analysis of the results showed that the magnitude of effect was consistent in individual participants across the two test rounds, suggesting this too might depend on personal physiological parameters. Linear regression to the personal data available showed a high correlation to gender (effect was consistently stronger in female volunteers), and a weaker correlation to BMI (probably to be linked to the fact that the same amount of water was ingested by participants having different body weights and compositions, leading to different effect scaling). However, gaining more insight into what parameters can explain this variability would be extremely valuable, allowing to predict for instance whether for particular subjects the detection limit be higher than for others. In this perspective, experimenting in a more controlled environment, allowing precise knowledge of the amount of liquid present at any point of time during monitoring, would allow investigating which type of relationships exists between feature value and linearly increasing fluid volume, as well as investigating tighter detection limits. One envisioned experimental scenario for this kind of study would be on peritoneal dialysis patients. Peritoneal dialysis is a medical procedure consisting in the infusion of a solution in the peritoneal cavity through a tube. Patients must typically undergo this procedure several times a day. By introducing a wearable accelerometer in the patient's routine, it would be possible to monitor such patients without additional discomfort, and test the technique in a situation where fluid accumulated is static and the amount of fluid present is know precisely at any time (unlike for the present experiment). Moreover, the fluid is introduced and removed several consecutive times, which would allow testing the technique in a long-term monitoring situation.

Another aspect to explore is how the effect changes in presence of different fluids. Viscosity of the fluid influences the amount of damping it causes. Therefore, it is likely that the response to blood accumulation or other bodily fluids be to some extent different from the one observed in presence of water. It would thus be interesting to repeat the experiment by substituting water with different types of edible fluids having different viscosities.

Furthermore, it could be investigated whether, and to what extent, a dependency exists between the energy feature value observed and instantaneous heart rate. For the present study, it was shown that the effect observed was not linked to changes in instantaneous heart rate. However, because the volunteers' heart rate was relatively stable throughout the experiment, it wasn't possible, at this stage, to exclude the possibility that a larger heart rate variation have some effect on the signal energy measured. This is a crucial point if envisioning the application of this technique to clinical scenarios where the heart rate might not be as stable as in the present study. In this view, an experiment could be designed where heart rate is intentionally modified in volunteers (e.g. by means of controlled physical exercise or paced breathing), and feature response is observed. Because the heart rate can be conveniently extracted from the same signal employed in feature calculation, should such dependency be known, normalization per the instantaneous heart rate would be possible without use of additional devices.

Finally, after all these aspects have been clarified, the next step would be defining in which way this feature can be used to develop a detection algorithm. This could be based on some defined thresholds in order to determine whether a measured feature value represents onset or increase of fluid accumulation from a baseline. With a more vast dataset, machine learning-based classification approaches could also be explored. This could involve, for instance, defining several classes (e.g. baseline, mild fluid accumulation, severe fluid accumulation... etc.), and including additional signal features and explanatory variables which could train the algorithm to personalize the classification based on individual parameter values.

In conclusion, insight gained from the present study opens up numerous possibilities for further exploration and development, with the promise of working towards a solution which could contribute to saving lives. Much about this fascinating topic is still left to experiment, understand and discover. Furthermore, along the path of progressing this technique towards a reliable monitoring tool, inevitably researchers will be faced with the challenge and pleasure of discovering new hidden rules and mechanisms governing the perfect machine that is the human body.

Bibliography

[1] The American College of Surgeons, "Advanced trauma life support (ATLS): the ninth edition.," *J. Trauma Acute Care Surg.*, vol. 9, pp. 1–392, 2013.

[2] I. Sadek, "Ballistocardiogram Signal Processing : A Literature Review," pp. 1–20.

[3] Steven K. Herrine, "Ascites - Hepatic and Biliary Disorders - Merck Manuals Professional Edition," *MERK MANUAL Professional Version*, 2018. [Online]. Available: https://www.merckmanuals.com/en-ca/professional/hepatic-and-biliary-disorders/approach-to-the-patient-with-liver-disease/ascites. [Accessed: 17-Aug-2019].

[4] K. Moore *et al.*, "The management of ascites in cirrhosis: Report on the consensus conference of the International Ascites Club," *Hepatology*, vol. 38, no. 1, pp. 258–266, Jul. 2003.

[5] V. Kumar, A. K. Abbas, and J. C. Fausto, *Pathologic Basis of Disease (7th ed.)*. Elsevier Saunders, 1999.

[6] "Hydrocephalus Fact Sheet," *National Institute of Neurological Disorders and Stroke*, 2016. [Online]. Available: https://web.archive.org/web/20160727231854/http://www.ninds.nih.gov/disorders/hydrocephalus/detail_hydrocephalus.htm. [Accessed: 17-Aug-2019].

[7] K. A. Galagan, *Color atlas of body fluids : an illustrated field guide based on proficiency testing*. College of American Pathologists, 2006.

[8] J. L. Pascual and J. W. Cannon, *Hemorrhagic Shock. Recognition, Pathophysiology and Management*. Nova Science Publishers, Inc. New York, 2017.

[9] N. S. Duncan and C. Moran, "(i) Initial resuscitation of the trauma victim," *Orthop. Trauma*, vol. 24, no. 1, pp. 1–8, Feb. 2010.

[10] J. R. Richards and J. P. Mcgahan, "Focused Assessment with Sonography in Trauma (FAST) in 2017 : What Radiologists Can Learn 1," *RSNA Radiol.*, vol. 283, no. 1, 2017.

[11] S. W. Branney, R. E. Wolfe, E. E. Moore, and E. Al., "Quantitative Sensitivity of Ultrasound in Detecting Free Intraperitoneal Fluid," *J. Trauma Inj. Infect. Crit. Care*, 1995.

[12] V. H. Gracias *et al.*, "Defining the learning curve for the Focused Abdominal Sonogram for Trauma (FAST) examination: implications for credentialing.," *Am. Surg.*, vol. 67, no. 4, pp. 364–8, Apr. 2001.

[13] B. J. Abrams, P. Sukumvanich, R. Seibel, R. Moscati, and D. Jehle, "Ultrasound for the detection of intraperitoneal fluid: the role of Trendelenburg positioning.," *Am. J. Emerg. Med.*, vol. 17, no. 2, pp. 117–20, Mar. 1999.

[14] M. C. Daignault, T. Saul, and R. E. Lewiss, "Bedside ultrasound diagnosis of atraumatic bladder rupture in an alcohol-intoxicated patient: a case report," *Crit. Ultrasound J.*, vol. 4, no. 1, p. 9, May 2012.

[15] E. Pinheiro, O. Pedro Girão, and U. S. Tiwary, "Theory and Developments in an Unobtrusive Cardiovascular System Representation: Ballistocardiography," *Open Biomed. Eng. J.*, vol. 4, no. 1, pp. 201–216, 2010.

[16] W. Dock and F. Taubman, "Some technics for recording the ballistocardiogram directly from the body," *Am. J. Med.*, vol. 7, no. 6, pp. 751–755, 1949.

[17] P. Paul and L. B. Symes, "Ballistocardiography in the Physics Classroom," *Phys. Teach.*, vol. 46, no. 5, pp. 300–302, 2008.

[18] K. S. Park and H. Yoon, "Ballistocardiography," pp. 127–155, 2018.

[19] O. T. Inan *et al.*, "Ballistocardiography and Seismocardiography: A Review of Recent Advances," *IEEE J. Biomed. Heal. Informatics*, vol. 19, no. 4, pp. 1414–1427, 2015.

[20] O. T. Inan, M. Etemadi, R. M. Wiard, L. Giovangrandi, and G. T. A. Kovacs, "Robust ballistocardiogram acquisition for home monitoring," *Physiol. Meas.*, vol. 30, no. 2, pp. 169–185, 2009.

[21] S. Rajala and J. Lekkala, "PVDF and EMFi sensor materials - A comparative study," *Procedia Eng.*, vol. 5, pp. 862–865, 2010.

[22] S. Kärki and J. Lekkala, "Film-type transducer materials PVDF and EMFi in the measurement of heart and respiration rates.," *30th Annu. Int. Conf. IEEE Eng. Med. Biol. Soc.*, pp. 530–533, 2008.

[23] O. Postolache, P. S. Girão, E. Pinheiro, and G. Postolache, "Unobtrusive and Non-invasive Sensing Solutions for On-Line Physiological Parameters Monitoring," *Wearable Auton. Syst. LNEE 75*, pp. 277–314, 2010.

[24] S. S. Rao, *Mechanical Vibrations 2nd Edition, Addison-Wesley Publishing Company, Inc., Reading, MA.*, no. 4303. 1990.
[25] E. Marieb and K. Hoehn, *Human Anatomy & Physiology*, Tenth. Pearson, 2016.
[26] L. Sörnmo, *Bioelectrical Signal Processing in Cardiac and Neurological Applications*. 2005.
[27] M. H. Hayes, "Statistical Digital Signal Processing and Modeling," 1996.
[28] J. Alametsä, A. Värri, J. Viik, J. Hyttinen, and A. Palomäki, "Ballistocardiogaphic studies with acceleration and electromechanical film sensors," *Med. Eng. Phys.*, vol. 31, no. 9, pp. 1154–1165, 2009.
[29] Y. Y. Lin Wang, M. Y. Jan, C. S. Shyu, C. A. Chiang, and W. K. Wang, "The Natural Frequencies of the Arterial System and Their Relation to the Heart Rate," *IEEE Trans. Biomed. Eng.*, vol. 51, no. 1, pp. 193–195, 2004.
[30] J. M. W. Brownjohn and X. Zheng, "Discussion of human resonant frequency," in *Proceedings of the SPIE, Volume 4317, p. 469-474 (2001).*, 2001, vol. 4317, pp. 469–474.
[31] S. W. Smith, "03 ADC and DAC," *Sci. Eng. Guid. to Digit. Signal Process.*, pp. 35–66, 1997.
[32] N. E. Huang *et al.*, "The empirical mode decomposition and the Hilbert spectrum for nonlinear and non-stationary time series analysis," *Proc. R. Soc. A Math. Phys. Eng. Sci.*, vol. 454, no. 1971, pp. 903–995, 1998.
[33] T. Lumley, P. Diehr, S. Emerson, and C. Lu, "The Importance of the Normality Assumption in Large Public Health Data Sets," *Annu. Rev. Public Heal.*, 2002.
[34] D. A. W. Hollander, M., "Nonparametric statistical methods," *Biom. Z.*, vol. 17, no. 8, pp. 526–526, Jan. 1975.
[35] G. P. P. Lambert, R. T. T. Chang, T. Xia, R. W. W. Summers, and C. V Gisolfi, "Absorption from different intestinal segments during exercise.," *J. Appl. Physiol.*, vol. 83, no. 1, pp. 204–12, 1997.
[36] R. Murray, D. Eddy, W. Bartoli, and G. Paul, "Gastric emptying of water and isocaloric carbohydrate solutions consumed at rest," *Med. Sci. Sport. Exerc.*, vol. 26, no. 6, pp. 725–732, 1994.
[37] F. Péronnet *et al.*, "Pharmacokinetic analysis of absorption, distribution and disappearance of ingested water labeled with D2O in humans," *Eur. J. Appl. Physiol.*, vol. 112, no. 6, pp. 2213–2222, 2012.
[38] M. S. Fadali, J. W. Steadman, and R. G. Jacquot, "A model of water absorption in human intestine," *Biomed. Sci. Instrum.*, vol. 16, pp. 1–14, 1980.
[39] J. B. Leiper, "Fate of ingested fluids: factors affecting gastric emptying and intestinal absorption of beverages in humans," *Nutr. Rev.*, vol. 73, pp. 57–72, 2015.
[40] R. S. Gubner, M. Rodsteing, and H. E. Ungerleider, "Ballistocardiography: An Appraisal of Technic, Physiologic Principles, and Clinical Value," vol. VII, no. February, pp. 268–286, 1953.
[41] Rita Baron-Faust, "A woman's heart: a mystery of science," *Medscape*, 2000. [Online]. Available: https://www.medscape.com/viewarticle/782902#vp_3. [Accessed: 14-Aug-2019].